

DESIGN OF A SUPER-COMPRESSIBLE METAMATERIAL

AN EXPERIMENTAL INVESTIGATION GUIDED BY MACHINE
LEARNING

DESIGN OF A SUPER-COMPRESSIBLE METAMATERIAL

AN EXPERIMENTAL INVESTIGATION GUIDED BY MACHINE
LEARNING

by

Michael HOULDER

Master Thesis

submitted in partial fulfilment of the requirements for the degree of

Master of Science

Technical University Delft, Delft, Netherlands,
Department of Cognitive Robotics, Master track Vehicle Engineering.
To be publicly defended on Wednesday 29 May 2019 at 13:00

Thesis Supervisor,

Dr. M.A. Bessa

Technische Universiteit Delft

Committee members:

Prof. dr. ir. J. Sietsma,

Technische Universiteit Delft

Prof. dr. I.M. Richardson,

Technische Universiteit Delft

Dr. ir. O.K. Bergsma,

Technische Universiteit Delft

Copyright © 2019 by Michael Houlder

Student number: 4146778

An electronic version of this dissertation is available at
<http://repository.tudelft.nl/>.

SUMMARY

Mechanical metamaterials are a new emerging class of materials which achieve properties outside the bounds of conventional materials. A metamaterial consists of a unit cell which is periodically repeated in space. In this study, a new metamaterial unit cell is proposed, derived from a class of space structures known as deployable masts. What makes these masts particularly interesting is their ability to contract to a fraction of their original length. In order to use such a structure as a unit cell, requires a deep understanding of the design parameters impact on material response.

To guide this project, a novel data driven approach to design will be implemented. Here, computational simulations are used to create a database of mechanical responses, which in turn is used to model the relationship between input and output responses. This approach essentially flips the conventional approach of mechanical design on its head by using computational simulations to define the design space before manufacturing and testing. This replaces designer intuition with predictive charts, becoming increasingly useful for non-intuitive problems.

This study validates the data driven approach through mechanical testing of a metamaterial unit cell. This testing is done at the macroscopic scale, utilizing a hobbyist 3D-printer (Ultimaker 2) to manufacture the structure. This study demonstrates that the material model is capable of accurately predicting the unit cell response. The limitation and possibilities for fused deposition modelling printed parts to be used as functional components is also investigated. Based on the insights gained from the data driven design process and experimental validation, design parameters are proposed for which a metamaterial unit cell exhibits both extreme compressibility and a high compressive strength.

CONTENTS

Summary	v
1 Introduction	1
2 Literature review	5
2.1 Metamaterials.	5
2.1.1 Micro-/nanolattices	7
2.1.2 Chiral metamaterials.	9
2.1.3 Origami metamaterials	10
2.1.4 Pattern transformation.	10
2.1.5 Pentamode metamaterials & negative compressibility	11
2.1.6 Auxetic metamaterials	12
2.2 A selection of highly compressible materials	12
2.3 Coilable space structures: the deployable mast	16
2.4 Additive manufacturing.	19
2.4.1 Fused deposition modeling	20
2.4.2 Stereolithography	21
2.4.3 CLIP: continuous liquid interface production	21
2.4.4 Powder bed fusion	21
2.4.5 Inkjet	22
2.4.6 Direct energy deposition.	22
2.4.7 Laminated object manufacturing	22
2.4.8 Microscopic additive manufacturing.	24
2.5 Data-driven computational design	24
2.6 Knowledge gap, aims and objectives	25
3 Data driven framework applied to a buckling mast	43
3.1 Proposed metamaterial concept	43
3.2 Data Driven Approach	44
3.2.1 Design of Experiments	44
3.2.2 Finite element analysis.	45
3.2.3 Geometric imperfections	46
3.2.4 Response data	46
3.2.5 Machine learning	46
3.3 Design Charts.	47
3.4 Analytical model	47
4 Characterizing the Material	59
4.1 Mesosstructure characterization.	60
4.1.1 Ideal packing.	60

4.1.2	Longeron mesostructure analysis	60
4.2	Characterization of 3D printed material properties	62
4.2.1	Uniaxial tensile tests	63
4.3	Uniaxial compression tests	68
4.4	Shear testing	71
4.5	Yield Surface Longeron	72
4.6	Summary	75
5	Experimental validation of data-driven design	79
5.1	First 3D printed prototypes	79
5.2	First half-mast design	80
5.3	Second mast iteration	82
5.4	Third mast iteration	83
5.5	ML classification validation	84
5.6	Comparison with state of the art	90
5.7	Additional preliminary investigations	94
5.7.1	Mirrored stacked unit cells	94
5.7.2	Scaling the problem	94
6	Discussion	105
6.1	Importance of friction effect	105
6.2	End rotation imperfection (first buckling mode)	106
6.3	Repeated loading	106
6.4	Longeron Cross section	107
6.5	Applications	107
7	Conclusion and Recommendations	111
7.1	Conclusion	111
7.2	Recommendations	112
	References	115
A	List of Tests	125
B	Ultimaker 2 printers and used material	127
B.1	Ultimaker 2 print process	127
B.2	Printing Settings	128
B.3	Polylactic Acid	129
B.3.1	Superior material choice	129
C	Longerons	131
C.1	Failed prints	131
C.2	Pin-hole relationship	131
C.3	Longeron cross section	131
D	Novel design to print mast on Ultimaker 2	135
E	Supplementary information material testing	139
E.1	Densification strain	139
E.2	ASTM D638-14	139

E.3	Dog-bone specimens	141
E.4	ASTM 695-15 compression specimen	143
E.5	Torsion testing	145
E.5.1	Torsion specimen cross section	146
E.5.2	torsion testing apparatus.	148
E.6	Yield surface plot	148
F	7 parameter model	151

1

INTRODUCTION

LOW density materials are commonplace in the world today in the forms of honeycombs and foams. These materials prove effective for lightweight structures and applications which, amongst others, require vibration absorption, thermal insulation, and filtering [1]. A comparison of their density with other common materials is given in Figure 1.1, where the low Young's modulus of low density materials can be noted. Their high ultimate compressive strains (densification strain) are invariably linked to their low compressive strength, as shown in Figure 1.2. This work strives to improve these apparently antagonistic properties, with the goal of increasing compressive yield strength by creating a new lightweight, strong, and recoverable metamaterial.

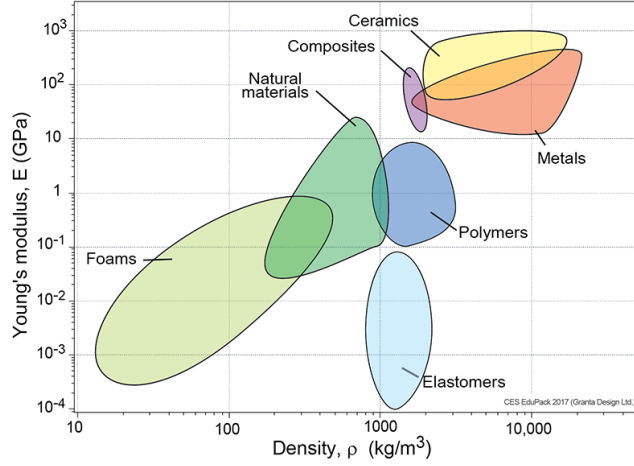


Figure 1.1: Ashby plot showing density and Young's modulus of different material classes [2]

Materials (foams, honeycombs) are highly deformable due to having a large number of air pockets. It logically follows that a way of increasing compressibility of a material is simply to cut slots or holes into it, as demonstrated by Mullen et al. [3]. However, the Young's modulus (E) of the material scales with density (ρ) as $E \sim \rho^2$ or $E \sim \rho^3$ for materials with stochastic architecture. [4]. In order to make this relationship linear ($E \sim \rho$), an underlying structure needs to be created [5]. A material constructed with a repeated underlying man-made architecture is known as a metamaterial, and when targeting mechanical properties it is labelled as mechanical metamaterial.

The more practical minded reader may notice that there is no direct application in mind for such a structure. This research is exploratory in nature, i.e. an attempt to demonstrate the feasibility of a new concept by combining additive manufacturing and machine learning to create it. This thesis focuses on the manufacturing and experimental testing of the metamaterial, including computational and analytical modelling as well as machine learning generated design charts. Therefore, Chapter 2 provides a literature review to establish a baseline for this research. The chapter starts with an overview on mechanical metamaterials, focusing on highly compressible and/or energy absorbent solutions presented by different authors. Then, section 2.3 introduces the aerospace structure that served as a starting point for the data-driven design of a new metamaterial: the deployable mast. Relevant additive manufacturing techniques are discussed in section 2.4, and a brief overview of the data-driven design framework created by Bessa et al. [6, 7] is provided at the end of the chapter. The data driven framework was used to create design charts to guide the experimental exploration conducted in this work.

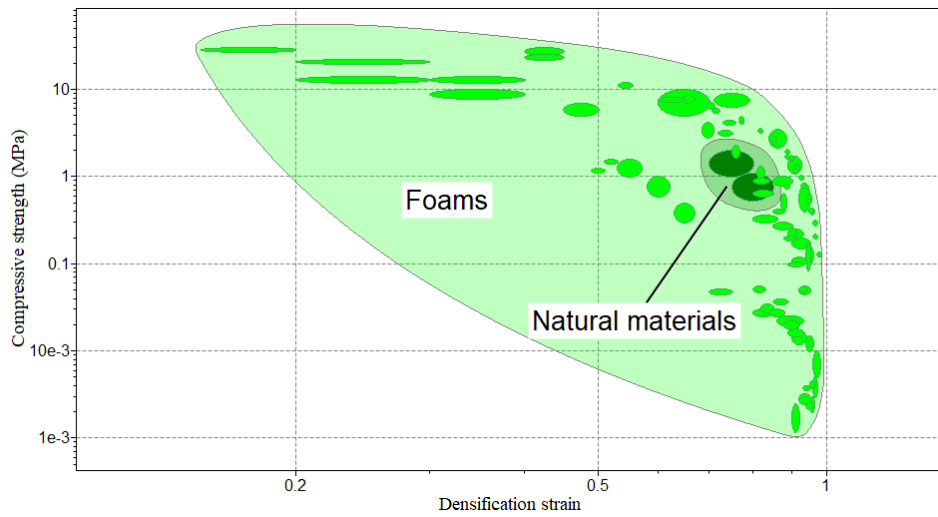


Figure 1.2: Ashby plot: Densification strain and compressive strength made with CES Edupack. For details about what densification strain represents see Figure E.1

2

LITERATURE REVIEW

2.1. METAMATERIALS

METAMATERIALS, also known as designer materials and architected materials, are a product of human ingenuity. The term was first used in the field of optics [8] where the focus was primarily on light refraction and cloaking. Soon after, metamaterials were introduced in the field of acoustics [9], as both situations focus on controlling waves. Metamaterials are changing the way we think about material properties and design. Their underlying structures as such are not found in nature and usually consist of repeating unit cells (see Figure 2.2). This structure is typically constructed on the micro- or nanoscales and is designed to achieve desirable characteristics at the macroscale. Importantly, the material derives its properties primarily from the underlying architecture rather than the chemical composition and microstructure of the base material [10].

The focus here is providing an overview of mechanical metamaterials, which is facilitated by classifying them into classes. Different classification systems have been proposed. Bertoldi et al. [11] divide them into four subcategories: linear mechanical metamaterials, mechanism based metamaterials, instability based metamaterials and topological metamaterials. Yu et al. [12] propose a classification based on their elastic constants.

Typically metamaterial properties are associated with the four elastic constants, the Young's modulus (E), shear modulus (G), bulk modulus (K), and Poisson's ratio ν . These metamaterials are classified as strong-lightweight (E/ρ), pattern transforming, Pentamode ($G \ll K$), auxetic ($G \gg K$), and materials with negative compressibility ($-4G/3 < K < 0$). Furthermore, using topology optimization materials can be created with properties as ultra-low density, ultralight stiffness, vanishing shear modulus and negative Poisson's ratio [12]. Many designs are presented in literature for both two- and three-dimensional metamaterial structures. The reader is referred to relevant examples of materials with

negative Poisson's ratio [13], negative compressibility [14], and negative incremental stiffness [11]. These and other solutions have a wide range of applications, such as shape matching [15], self-folding [16], and energy absorption [4, 5]. Considering the interests outlined for this thesis, the following sections are dedicated to low-density, highly deformable materials that typically explore buckling and postbuckling behavior in the elastic or plastic regimes.

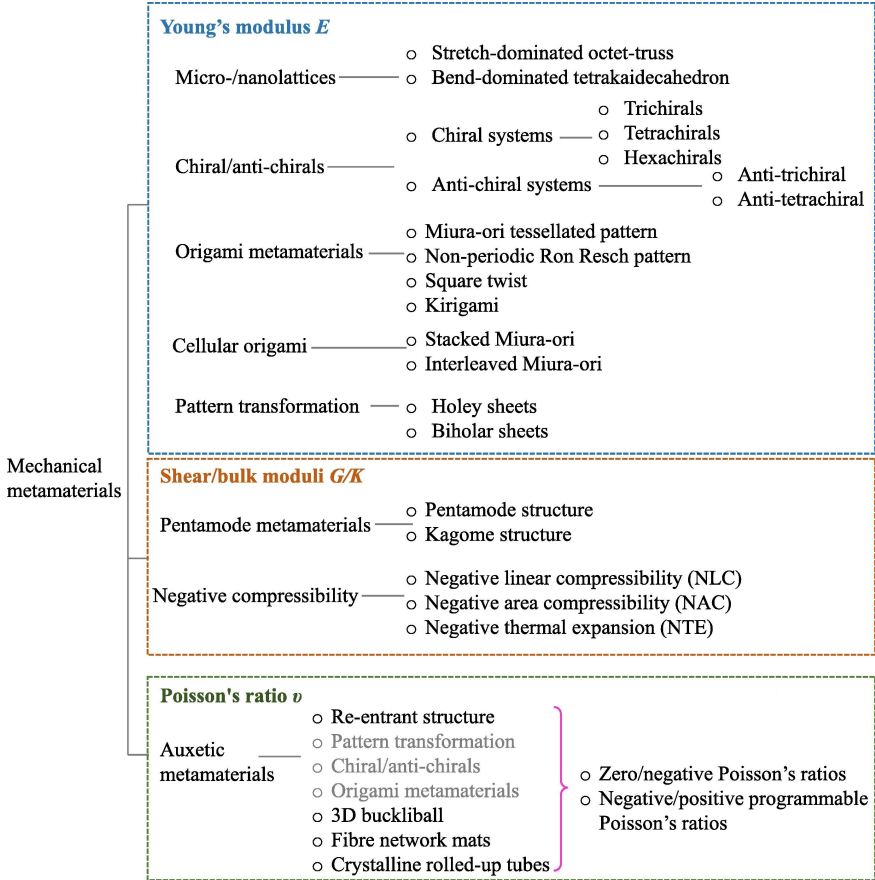


Figure 2.1: Classification of mechanical metamaterials [12]

Figure 2.1 shows the three main subcategories following Yu et al. [12] namely: Young's modulus E , Shear/bulk moduli G/K , and Poisson's ratio ν . These elastic constants along with the functional characteristics of the material are determined by the cell morphologies, porosity, and the properties of its chemical composition [17]. This classification relates each metamaterial concept to the elastic property it most influences. For a detailed explanation of derivations of the fundamental elastic properties the reader is referred to the paper from Yu et al. [12]. The key to metamaterial design is adjusting the cell morphology to obtain desired results at the macroscopic level. These underlying build-

ing blocks can deform, rotate, buckle, fold, and snap in response to mechanical forces and are designed in such a manner that together they yield a desired behaviour. The following sections briefly explain each subcategory with examples, after which a deeper literature review on highly compressible materials is provided.

2.1.1. MICRO-/NANOLATTICES

Micro and nanolattices represent two of the most common forms of mechanical metamaterials. Their primary goal is to achieve low density ($< 10 \text{ kg/m}^3$) whilst maintaining high stiffness [12]. Figure 2.2 shows two examples of such a structure, Figure 2.2 A shows an octet truss structure, and Figure 2.2 D a tetrakaidecahedron shape [5, 18].

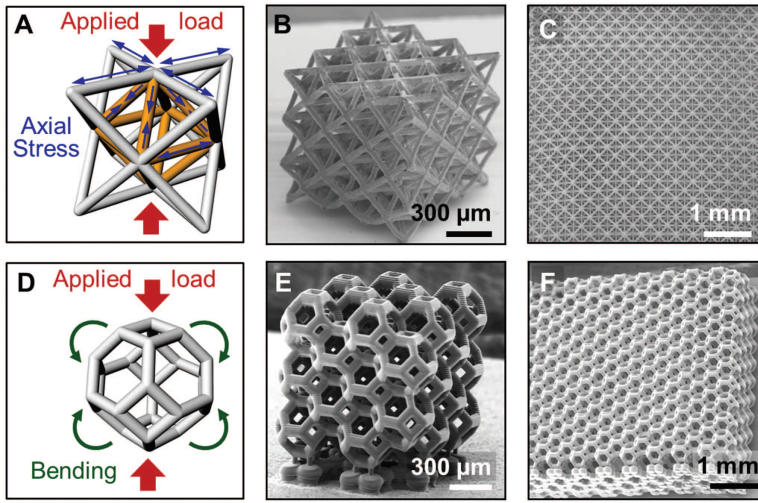


Figure 2.2: Metamaterial example showing a octet-truss unit cell and tetrakaidecahedron unitcell made using projection microstereolithography and coated with either hollow-tube nickelposphorus (Ni-P) or (amorphous Al_2O_3 , alumina) [5]

Man made micro-/nanolattice metamaterials are inspired by cellular solids, for example, honeycomb and foam-like structures. The geometry of the unit cell and its tessellation are significant for their design. A unit cell consists of periodic bars or tubes connected at nodes, so this type of structure can only be constructed via additive manufacturing (see Chapter 2.4.8) when considering micro- and nanoscales. For cases with structural hierarchy, the stiffness is determined by the relative density and the spatial configuration of voids in the solids [19, 20]. As the structures of these materials are not random as with foams, this leads to predictable material behaviour. Designing the material in this manner also leads to the Young's modulus scaling with density as $E \sim \rho^2$, as opposed to $E \sim \rho^3$ for a single material, as observed in aerogels and carbon nanotube foams [4].

Figure 2.2 shows a metamaterial created by Zheng et al. [5]. The corresponding stress-strain curves under compressive load are shown in Figure 2.3, as they represent a key figure of merit to this work. Note that Figure 2.3 clearly indicates when the material

yields.

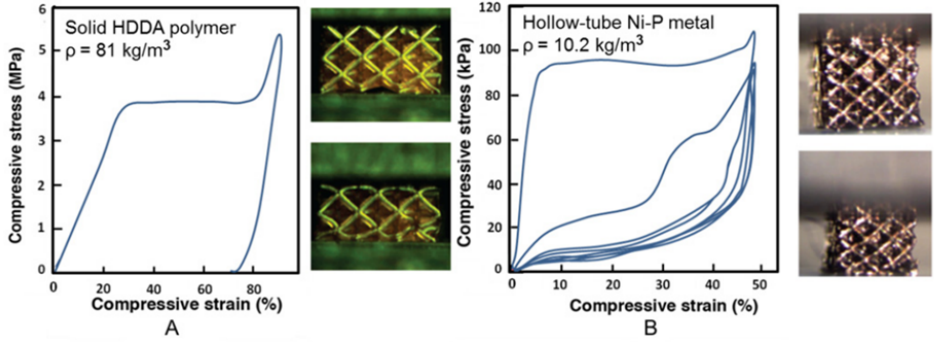


Figure 2.3: Stress-strain curve under compressive load [5]

Zheng et al. [5] tested several material designs, both for polymers and metals, and compared their elastic moduli as shown in Figure 2.4. The stress-strain plots seen in Figure 2.3 pertain to the polymer test on the left and the nickel-phosphorous material on the right. The polymer lattice undergoes plasticity, as highlighted from the unloading path, but the metal lattice is able to return to the origin, albeit with significant yielding of the material.

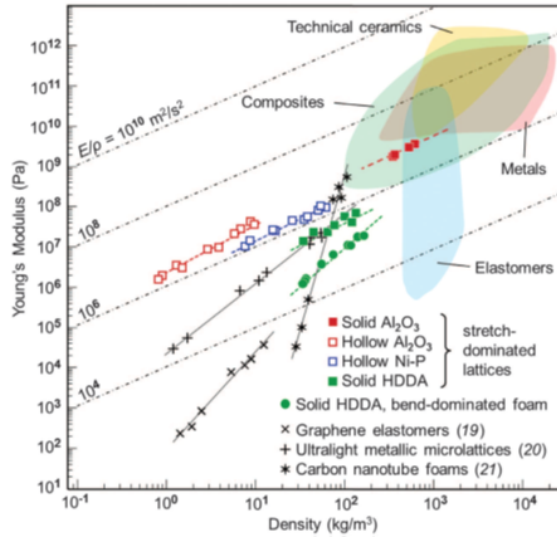


Figure 2.4: Ashby plot of Zheng et al. lattice structures for several metamaterials showing different ($E \sim \rho^n$) relationships which can be obtained using metamaterials [5]

Methods for minimizing plasticity and damage of the lattice structures through altering the structure geometry is addressed in several other articles [21–23], but in general

strength, compressibility and energy absorption capabilities quickly degrade with multiple loading cycles. Schaedler [4], for example, reports a nearly constant energy loss coefficient of 0.4 after three repeated cycles. This shows that the amount of energy (area under stress strain curve) required to compress the mast is dissipating due to the onset of plasticity.

Remark 1 *Achieving high compressibility, high strength and full recoverability remains a significant challenge, as evidenced by the literature.*

2.1.2. CHIRAL METAMATERIALS

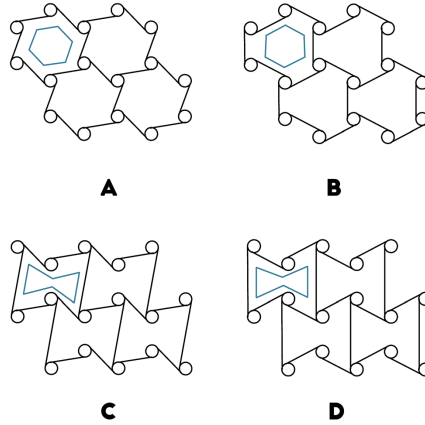


Figure 2.5: (A) Trichiral honeycomb. (B) Re-entrant trichiral honeycomb. (C) Anti-trichiral honeycomb. (D) Re-entrant anti-trichiral honeycombs. [24]

A chiral structure has a geometry which cannot be superimposed on itself; therefore it is not symmetrical and can be constructed in either a left handed or right handed manner creating chiral or anti-chiral structures [25]. Anti-chiral structures exhibit reflective symmetry as the nodes are on the same side of the connecting ligaments – see Figure 2.5 C and D. [24]. Chiral metamaterials were first proposed by Wojciechowski [26]. Later examples include an hexagonal chiral honeycomb structure by Prall and Lakes [27]. The figure illustrates chiral (Figure 2.5 A and B) and anti-chiral (Figure 2.5 C and D) materials with an array of cylindrical nodes connected by ribs. Using anti-chiral structures is one possible way to create auxetic behaviour ($G \gg K$) in materials. Chiral and anti-chiral materials can exhibit unique material properties especially with respect to the Poisson's ratio and thermal expansion coefficient [12].

A recent metamaterial creation by Frenzel et al. [28] demonstrates the unique material behaviour achieved through intelligent metamaterial design. Figure 2.6 shows that a twisting motion can be achieved under compressive load through a three dimensional chiral structure.

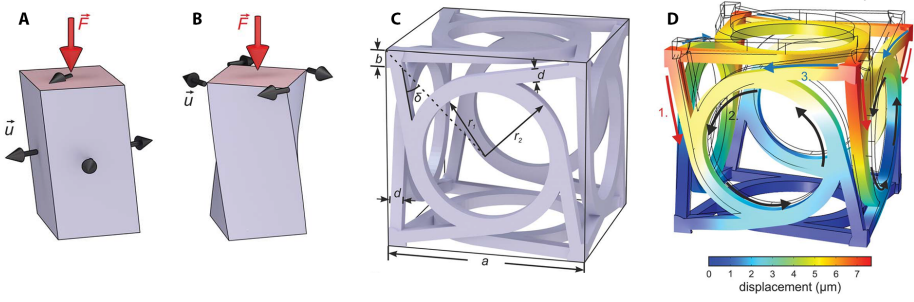


Figure 2.6: Twisting metamaterial concept presented by Frenzel et. al. [28] where $(75 < a < 350) \mu\text{m}$

2.1.3. ORIGAMI METAMATERIALS

The term "origami" is Japanese for folded paper. It has long been known that when thin sheets are bent, buckled, or assembled into smaller interlocking structures, the stiffness can be significantly increased [16]. In recent years this age-old tradition is being applied to create new materials which exhibit unique properties [12, 16, 22, 29–31]. Simply folding a piece of flat material, a whole range of material properties can be achieved including but not limited to auxetic behaviour, programmable stiffness and bi-stable snapping, as seen in the next subsection. The Miura-ori fold is one of the common ways in which to fold a sheet of paper results in auxetic behavior under compression. Other common folding patterns include Ron Resch pattern, and Square twist pattern [12].

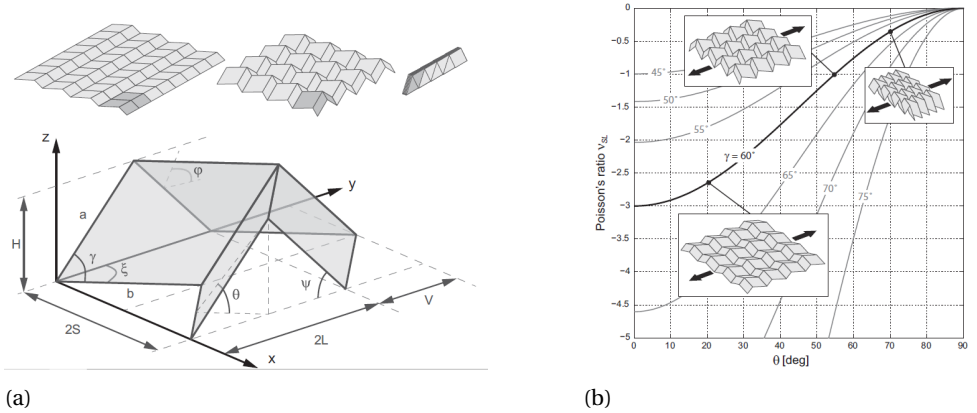


Figure 2.7: Miura-ori folded structure and their achievable Poisson's ratios with different geometries [32]

Origami introduces fundamental issues when compressive strength in more than one direction is sought, because the material typically has near zero-energy deformation

modes. An example of a Miura-ori pattern using steel is provided by Xiang et al. [33].

2.1.4. PATTERN TRANSFORMATION

Pattern transformation metamaterials have adjustable effective stiffness (E) as a function of the topology. For example, tuning a pattern of holes within the material [12] can cause the force-displacement curve to change by altering the hole size, as shown in Figure 2.8.

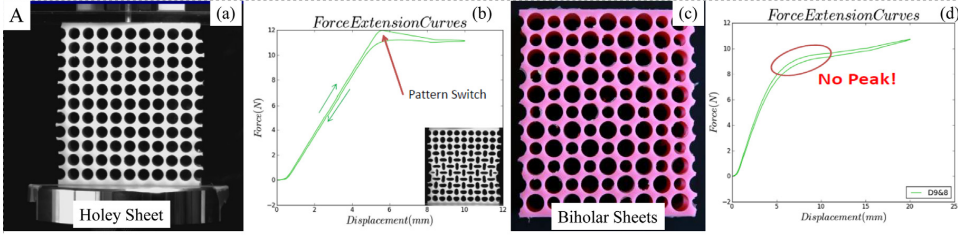


Figure 2.8: Pattern based metamaterials [12]

Hole shapes also have significant impact on how a material deforms under compressive or tensile loads. The shapes can range from circles and ovals to stars and to more complex geometries. Designing holes in such a way can also lead to materials which exhibit snapping behaviour and bi-stable states.

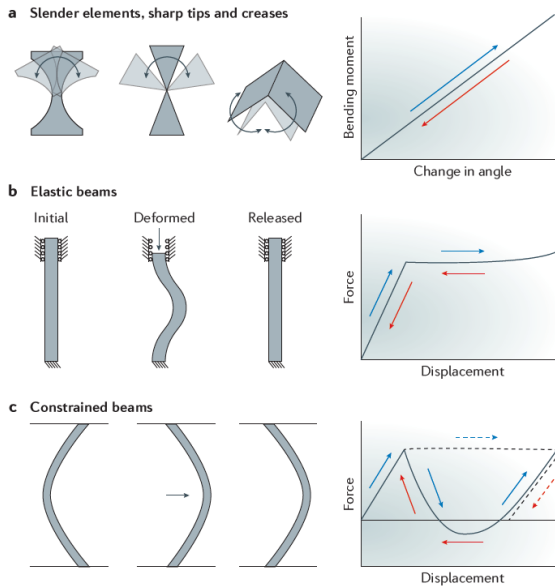


Figure 2.9: Bending and buckling characteristics of a slender beam element [11]

The pattern transformations that lead to bi-stable states and snapping are also known as instability based metamaterials. These materials employ buckling and snapping type behaviours that result in strongly non-linear relations between macroscopic stresses and strains [11]. Symmetric elements can undergo buckling instabilities that result in strong reversible non-linearities under loading conditions. Having multiple stable states also allows a snap-through behaviour in which energy can be absorbed.

Buckling (a property used in several metamaterial designs) is a phenomenon that has been known for centuries but was often seen as undesirable and avoided. Recent interest has led to new research in which buckling is used rather than avoided. Two beneficial features of a structure which is designed to buckle (Figure 2.9 B and C) are the high rate of motion and sudden release of energy after buckling [34], making it an ideal mechanism for adaptive and smart applications. In addition, buckling can be used in bi-stable states (see Figure 2.9 C).

Figure 2.10 shows how changing the hole shape for a holey sheet can lead to snapping behaviour and bistable states. In this case two different materials are used, but a similar result can be achieved with a single material. Such a structure can be altered to work in three dimensions, as shown by Haghpahan et al. [35]. In this way a material can achieve multiple stable configurations.

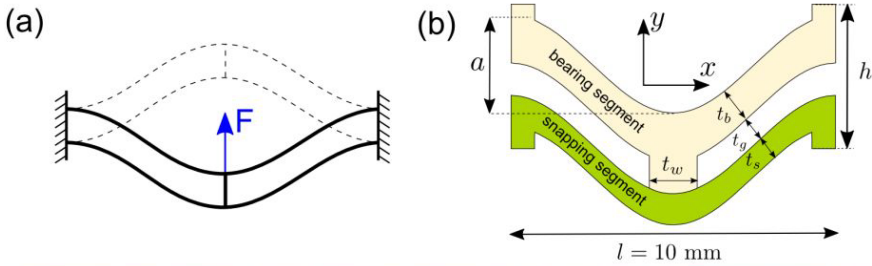


Figure 2.10: Snapping mechanism using bistable states where snapping segment is deformed as showing in (a) resulting in two different stable heights (b). [10]

The area under the stress-strain curve is the required energy to deform a structure. If this structure modes to a new stable position seen in Figure 2.9 c, the energy under the curve is absorbed by the structure. Therefore, by having bi-stable states one can store energy within a material. This is something that can be considered in future studies.

2.1.5. PENTAMODE METAMATERIALS & NEGATIVE COMPRESSIBILITY

A pentamode metamaterial is an artificially created structure which is solid, while having the mechanical characteristics of a liquid [22]. This means that it has a finite bulk modulus (K) and a vanishing shear modulus (G), i.e. it is difficult to compress but easy to shear [12].

Negative compressibility materials deform in an unexpected manner. When a force acts on a material, it is usually stretched in the same direction as the force, but with negative

compressibility the material will deform in the opposite direction [36]. As with Penta-mode materials, the material characteristics are not relevant to achieving high compressive strength or a high strain, thus they fall outside the scope of this thesis.

2.1.6. AUXETIC METAMATERIALS

As mentioned above auxetics are a class of materials which have a negative Poisson's ratio ($G \gg K$) – see Figure 2.11. The Poisson's ratio ν defines the ratio between transverse and axial strain in uniaxial loading [37]. This means auxetics counter-intuitively will contract in the transverse direction if a compressive load is applied [38]. Contrary to Buckmann [39] who proposes a bowtie lattice design which only demonstrates auxetic behaviour of small strains. Babaee et al. [38] investigated a design which they coin as Bucklicrystals. Rather than a lattice design these Bucklicrystals are spherical in which some holes are drilled. The spheres can be stacked in a similar manner to atoms in a BCC or FCC structure.

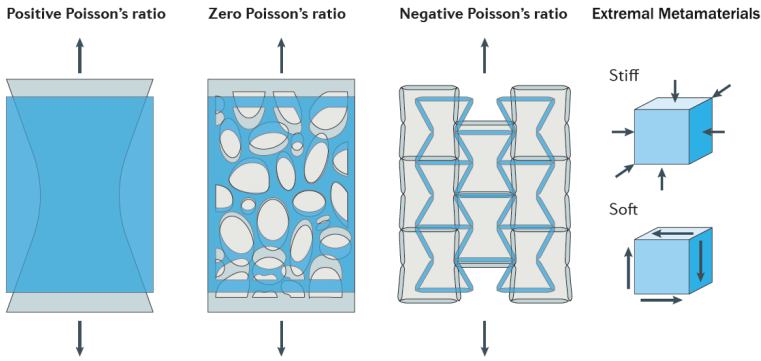


Figure 2.11: Negative Poisson's ratio and Extremal Metamaterials (adapted from Bertoldi et al. [11])

Remark 2 *Auxetic behavior is not the focus of this thesis, but the metamaterial building block investigated in this thesis will be implemented in a periodically repeating lattice that can be tuned to be auxetic.*

The flexible hinges used by Wang et al. [40] make use of shape memory to return to their original state after being deformed. Shape memory alloys can be triggered by stress or temperature change. Shape memory polymers are triggered with the above as well as electricity, light, moisture, and chemical stimulus. Moreover, shape memory alloys show shape recovery after 6-8% strain whereas some shape memory polymers can reach up to 400% in recoverable strain [34, 41].

2.2. A SELECTION OF HIGHLY COMPRESSIBLE MATERIALS

Within the literature of materials achieving high compressibility, four materials were considered particularly relevant to this thesis. An aerogel developed by Zu et al. [42], a low density graphene elastomer [43], three-dimensional periodic graphene aerogel mi-

colatlaces [17], and a super-compressible carbon nanotube film [44]. These materials achieve more than 50% repeatable compressive strain.

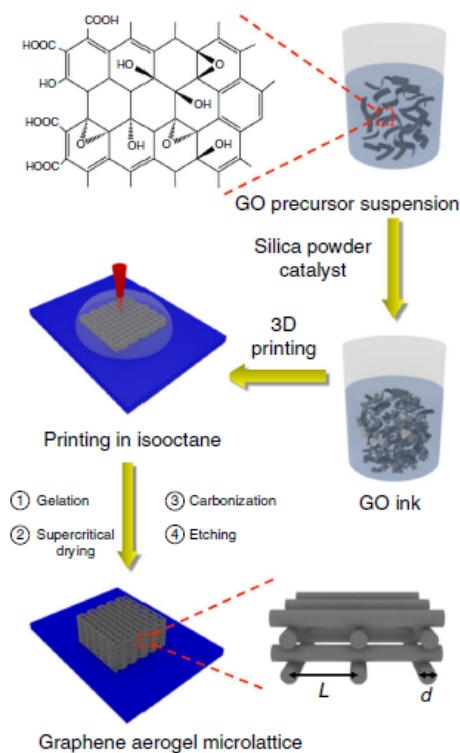


Figure 2.12: Construction of 3D printed graphene aerogel microlattices with a road diameter (d) of $200\ \mu\text{m}$ [17]

Zhu et al. [17] creates a 3D printed microlattice from graphene, a two dimensional material with low density and excellent mechanical properties. Using a solution (ink) containing graphene-oxide to 3D print a microlattice shown in Figure 2.12. This is a relatively basic 3D-printed structure, but with some refinements this technology may lead to printing more complex geometries with improved material properties.

The stress-strain curves in Figure 2.13 show that the material can achieve 50% strain, but with clear plastic deformation even at low strains as observed by the unloading paths. The area within the curves is the dissipated energy by plastic deformation. These plots demonstrate that the GO (graphene-oxide) inks containing R-F (resorcinol–formaldehyde) as seen in Figure 2.13 c and d, outperform both other inks. Secondly the plots for the 3D printed material (Figure 2.13 b and d) have better strain recovery than those using the bulk material. Figure 2.13 d is of particular interest as it shows nearly full recovery. Yet there are still clear signs of damage as the consecutive loading curves are different. This

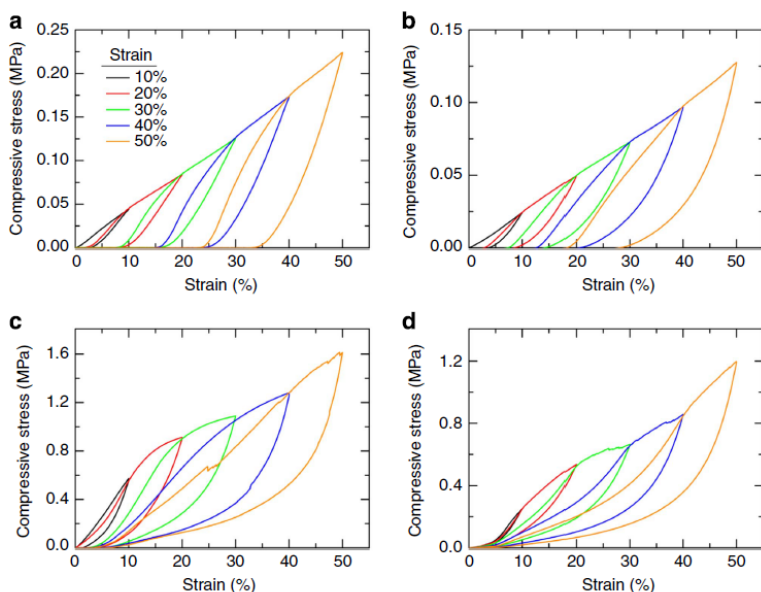


Figure 2.13: Stress-strain plots Zhu et al. 3D printed graphene aerogel microlattices: (a) bulk graphene aerogel (31 mg.cm^{-3}) and (b) 3D printed graphene aerogel microlattice (16 mg.cm^{-3}) using the GO ink without R-F, (c) bulk graphene aerogel (123 mg.cm^{-3}) and (d) 3D printed graphene aerogel microlattice (53 mg.cm^{-3}) using the GO ink with R-F [17]

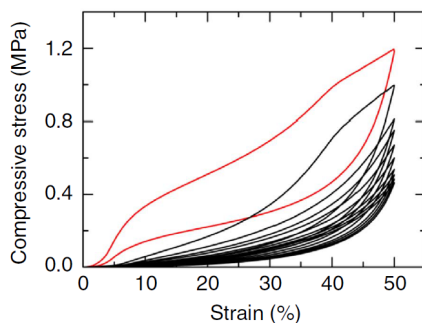


Figure 2.14: Stress strain response Zhu et al. 3D printed graphene aerogel microlattices for 10 consecutive loading cycles [17]

claim is further supported by the plastic deformation shown in Figure 2.14 that includes the material response over 10 consecutive cycles. This fast degradation of the properties is undesirable and will need to be addressed in a material which is intended to be loaded

several times.

Qiu et al. [43] take a different approach to creating a highly compressible material. Using the same base material as Zhu [17], they created a graphene elastomer foam and explore the relationship between mechanical resilience when decreasing the density. The authors [43] use a freeze casting technique to generate a graphene elastomer foam, after which several samples are thermally annealed at different temperatures ranging from 200 to 1000 degrees Celsius. The annealing temperature is the driving variable to see the impact on material strain recovery (return to original size and shape). Contrary to Zhu et al. [17], the molecular structure is random and thus relating it to the mechanical properties is challenging. A significant achievement is that the sample which was annealed at 1000 degrees Celsius was able to fully recover over 90% strain – see Figure 2.15b. This was the best performing material, as it achieved the largest amount of recoverable strain. However, it should be noted that the stress is low and it only achieves a high stress once the material is fully compressed. Therefore, the Young's modulus of the best performing material is very low, only 0.44 kPa, which means that this material is very compliant (not suitable for load bearing).

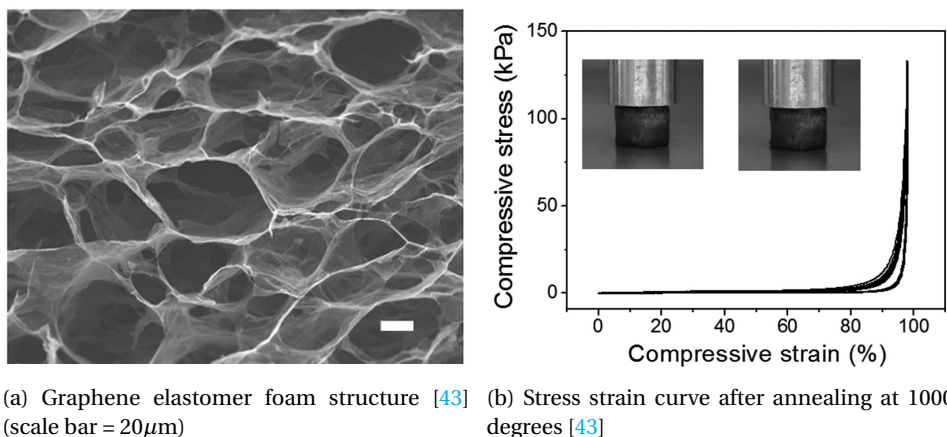


Figure 2.15: Graphene elastomer with a density of $1.64\text{mg}\cdot\text{cm}^{-3}$ by Qiu et al. [43].

Cao et al. [44] investigated a carbon-nanotube film structure which is orders of magnitude stronger than the previous examples – see Figure 2.16. The film is made of vertically aligned carbon nanotubes which deform in a zigzag manner under compression [44]. Interestingly, when compared to conventional foams the nanotube film shows significantly higher compressive stress, recovery rate, and sag factor (ratio of stresses at two deflections of 65% and 25%). The authors further demonstrate that this structure can be repeatedly compressed to 85% strain with nearly full recovery – Figure 2.16b. The sample survived over 10,000 cycles while losing less than 20 percent of its initial height.

Further examining Figure 2.16b, three distinct stages can be seen. With an initial Hookean region up to 22% strain with an elastic modulus of 50 MPa, a quasi plateau from roughly 22% to 79% strain with a modulus of 12 MPa, and a final densification, marked by a peak

stress of 25 MPa at 85% strain, which is orders beyond other metamaterial structures at this scale [44]. The superior degradation (20% loss over 10,000 compressive cycles) properties also make this a prime candidate for repeated loading. However the work presented by Cao et al. [44] is a two-dimensional structure and it would be challenging to implement in a three-dimensional lattice with similar properties. Secondly it can be noted that the compression is not fully linear as the unloading stress is lower than that of the loading stress. This means that some energy has been lost in the system.

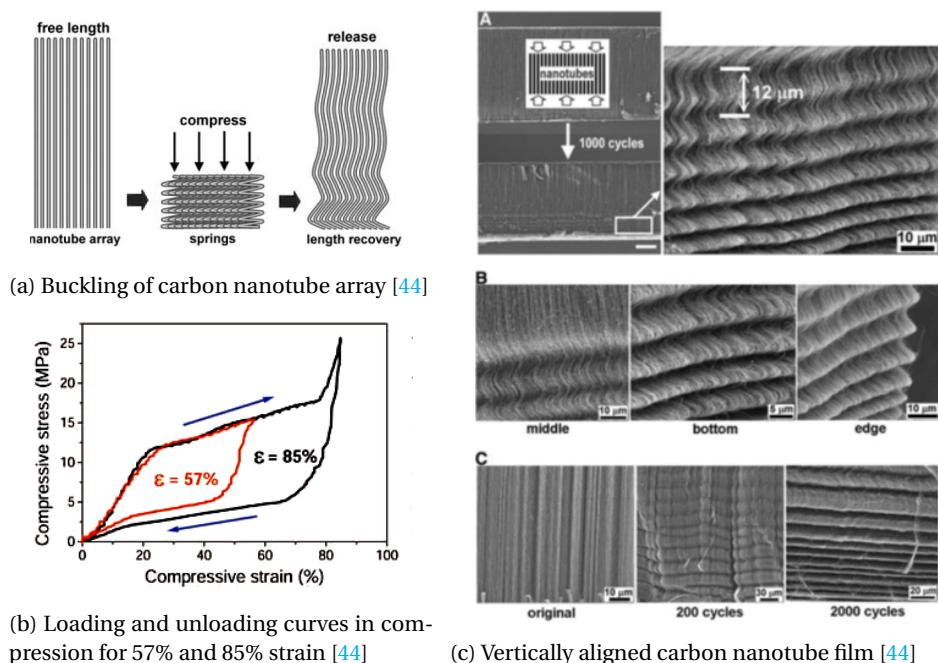


Figure 2.16: Carbon nanotube film by Cao et al. [44].

The final compressible material highlighted in this review was recently presented by Zu et al. [42]. Beyond high compressibility, the material achieves good thermal insulation, it is highly bendable, transparent, and machinable. The material is made by radical polymerization of a single alkenylalkoxysilane, leading to polyalkenylalkoxysilane and a subsequent hydrolytic polycondensation doubly cross-linked nanostructure consisting of polysiloxanes and hydrocarbon polymer units. The manufacturing and chemical composition fall outside the scope of this thesis but are detailed in their work [42]. Within the materials they analysed, the best performing in compression is the polyallylpoly-methylsiloxane (PAPMS) aerogel, seen in Figure 2.17d. It has a Young's modulus of 8.9 MPa which is lower than the carbon nanotube films by Cao et al. [44], but within the same order of magnitude. This material undergoes some energy loss and the peak stress is achieved at the end of compression, as observed in foam materials. The material is also able to recover fully after 80% strain. When considering all the properties of this material, we see the potential applicability it can have.

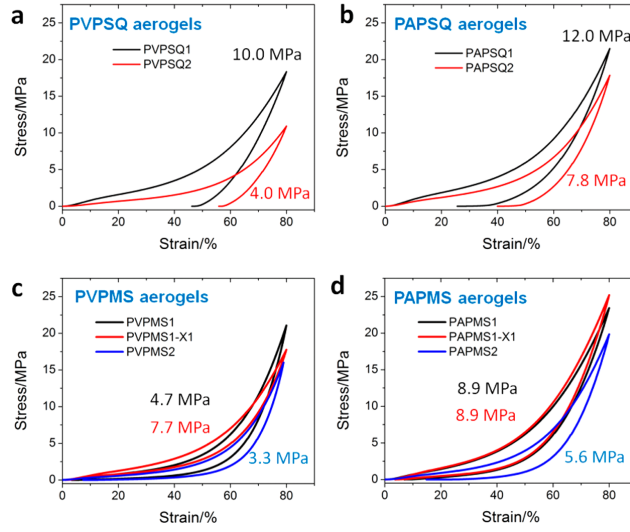


Figure 2.17: Stress-strain curves of uniaxial compression-decompression tests on typical (a) PVPSQ, (b) PAPSQ, (c) PVPMS, and (d) PAPMS aerogels. The values in the figure are the obtained Young's moduli. [42]

The few examples selected from the literature show that there is already an interest in creating highly deformable materials. The achievement Cao et al. [44] in this regard far surpasses all in terms of recoverable compressive stress, Figure 2.18. One thing that can be noted in Figure 2.18 is that the metamaterial proposed by Cao et al. already falls into the target zone. While highly remarkable, the compressive stress achieved by Cao only works in one dimension, and the design is not suited for implementation in three dimensions. For this reason, a target space (shown in red) is proposed for a new metamaterial which can be implemented in three dimensions. The PAPMS material created by Zu [42] also exhibits a high compressive strength without utilizing a metamaterial design, but by creating a highly porous material with extremely strong molecular bonds. One material surpassing all others in compressive strain is the Graphene-aerogel created by Qui [43].

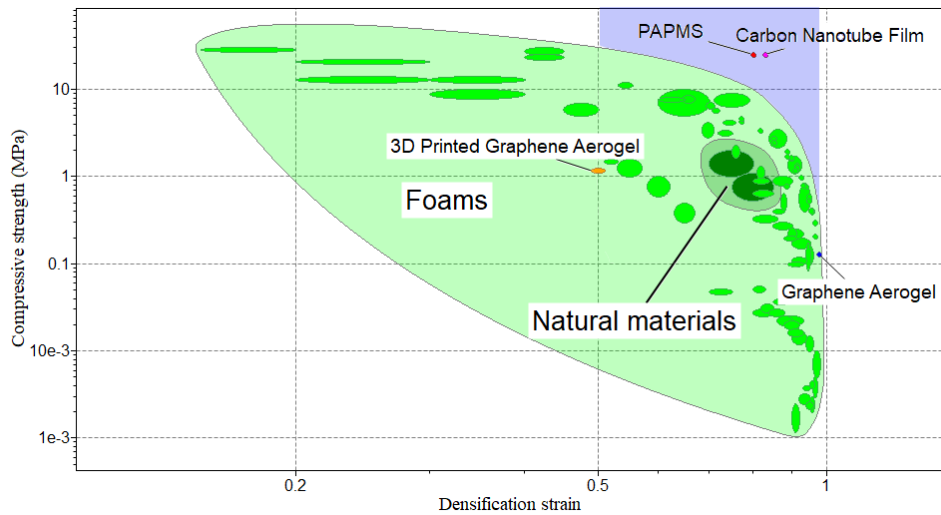


Figure 2.18: Compressive strength against Densification strain showing how metamaterial are able to surpass what traditional materials achieve for: carbon nanotube foam presented by Cao et al. [44], 3D printed graphene aerogel microlattice [17], PAPMS [42], and Grapehe aerogel [43]

2.3. COILABLE SPACE STRUCTURES: THE DEPLOYABLE MAST

When researching highly deformable structures one can consider deployable masts used in the space industry. Payloads of spacecraft have strict confinement limits when transporting objects into space. Therefore, the aerospace industry has been designing structures that are deployable while meeting demanding engineering requirements posed by the space environment. An interesting solution is the deployable mast used in satellite structures, as it consists of a highly deformable mechanism (99+ percent compressive strain) that when deployed is sufficiently rigid to maintain the shape of a satellite. An example of such a deployable mechanism is shown in Figure 2.19. Several mast designs have been made including the ISIS telescopic boom, the Collapse Tube Mast, the ADAM mast, and the CoilABLE boom [46–48].

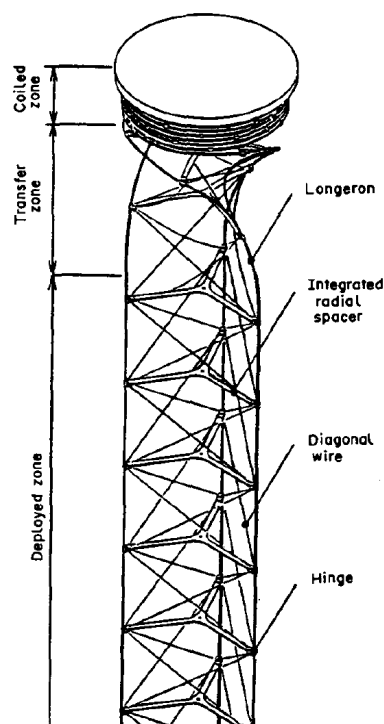


Figure 2.19: Deployable mast schematic [45].

The aforementioned masts use fundamentally different principles to achieve the large difference in length. They can be divided into several broader categories, namely: Inflatable booms, SMC booms, Truss Structures, Telescopic booms, Articulated booms, and Coilable booms. Puig et al. [46] compare these booms on a number of properties. Of key importance for this research project are the deployment length (maximum achievable length), the packaging ratio (ratio of compressed length to extended length), and the bending stiffness (resistance of lateral force). Figure 2.20 shows a comparison of different masts for these characteristics. Figure 2.20 A shows that the coilable mast has lower packaging ratio when compared to all other designs except the inflatable booms. Inflatable booms however do not seem to be implemented since 1996 for those lengths due to poor load capacity and stability. The coilable boom has the highest deployment length and bending stiffness which encompasses that of SMC booms. Articulated booms, and truss booms outperform the coilable boom in bending stiffness but have a larger boom diameter, higher mass, and worse packing ratio than that of the coilable mast.

The coilable mast is selected due to its design flexibility, high packing ratio, and wide range of mechanical properties lending itself to a data driven design approach.

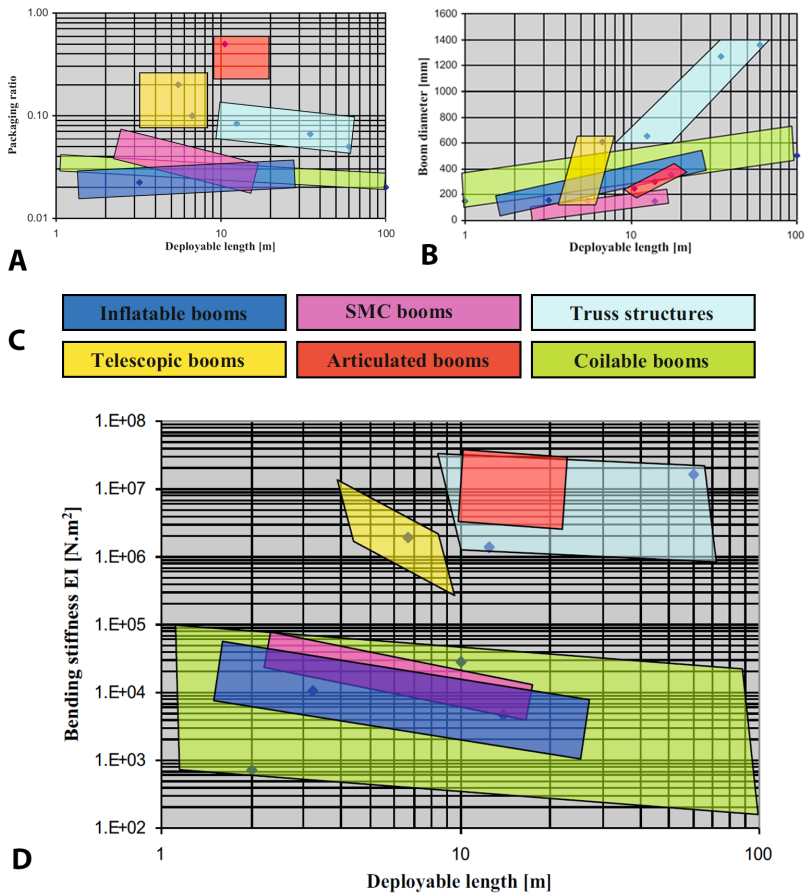


Figure 2.20: (A)Packing ratio - deployment length for various space masts (B) diameter - deployment length for various space masts (C) colour representation various masts (D) Bending stiffness - deployment length for space masts [46]

Figure 2.19 shows a coilable mast by Kitamura et al [45]. This mast design is derived from a deployable mast which was first developed by the Astro Research Cooperation. It is referred to as the coilable Astromast structure [49]. This design has a triangular cross section with three vertical rods (known as longerons) which are held in place by horizontal star shaped battens i.e. integrated radial spacers [45] and is held continually under compressive force by diagonal elements. This pre-compression is caused by tension of the diagonal cables as they are shorter than the nominal length, thus the whole structure is under pre-stress increasing overall stiffness [48].

The working principle of the mast is as follows: it is kept in a canister in its coiled state when it is launched in to space. Once at the correct location in space the mast is erected.

The deployment is controlled via a lanyard running down the centre whose force is in equilibrium with the force applied by the buckled longerons [50]. Figure 2.19 shows there are three deployment zones: (1) the coiled zone after which the mast goes through (2) the transfer zone into (3) the deployed zone. Although the deployed zone is resistant to lateral forces, the still partially coiled transfer zone is not. It is unable to resist lateral loads to the extent of the other zones and as such should be kept as small as possible. Looking at Figure 2.21 showing two possible deployment modes. In the helix mode, longerons twist along their entire length, while in the local mode they twist only locally forming a transition region between the coiled zone and the deployed zone [45, 48, 50]. The fundamental difference between these two coiling modes is that the helical mode resists lateral force significantly less than the local coiling mode.

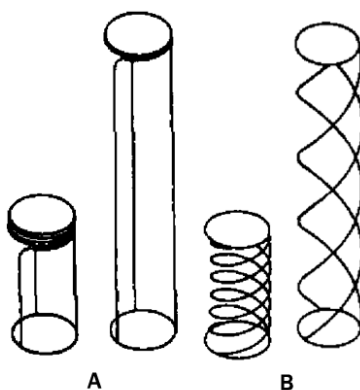


Figure 2.21: Coiling modes [45]

Key characteristics which determine the mast behaviour include the bottom helical angle, the number of bays, height between bays, longeron cross-section and longeron material [50]. The Young's modulus of the material which the longeron is made of, and the cross-section of the longerons determine the mast's bending stiffness. The bending strength of the mast is also determined by the aforementioned properties, as well as the distance between bays. The shear and torsional strength, however, are usually associated to the battens as well as the diagonal section properties [51].

Over the years, there have been many variations of the coilaible mast, but one notable one is the hingeless batten design seen in Figure 2.22 [45]. This design allows for increased alignment in the joints, and a simplification of the assembly process, thus saving time and costs. Despite subtle differences between versions of the masts the basic working principles are the same. Two idealized buckling modes are given in Figure 2.21, however the post buckling behaviour is based on many variables and few analytical models currently exist to predict post buckling behaviour. Xu et al. [48] for example, study the structural characteristics and natural frequencies of the mast during deployment, whereas Ma et al. [50] investigate the effects of the bottom helical angle on deformation, trying to optimize this for coiling in the local mode. It is clear, that an analytical model is needed to accurately predict the behaviour of such structures both before and after

buckling occurs. Bessa et al. [6] propose a new data-driven computational framework which can be used as a tool along side the usual iterative design process to find optimal solutions for particular design requirements. They apply this framework to an ultra-thin deployable carbon fibre shell boom and optimize the design for buckling load [7]. Applying such a tool to the Astromast may lead to new designs yet to be explored.

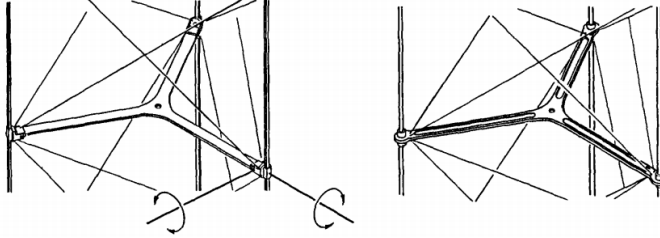


Figure 2.22: left: classic design with mechanical hinges at the joints, right: Hingleless design incorporating flexible battens [45]

Other deployable structures have also been reviewed but a detailed analysis will fall outside the scope of this literature review. Their working principles are either very similar to that of the Astromast, or not suitable for use in a highly deformable metamaterial. A comprehensive analysis of deployable booms can be found in a review paper by Puig et al. [46]. Note that other space structures can be and have been applied to design metamaterials, for example the deployable space structure by Arita et al. [52].

Analytical model

Kitamura et al. [45] propose an analytical model to predict the mast response to load during packing and unpacking of the mast. This equation represents the force exerted along the length (z direction) as a function of the percentage deployed. Two models are presented: a local coil response model and a helical response. Helical response:

$$F = \frac{4nx}{D_1^2 L} \left[2E_1 I_1 \left\{ 1 - \left(\frac{x}{L} \right)^2 \right\} + G_1 J_1 \left\{ 2 \left(\frac{x}{L} \right)^2 - 1 \right\} \right] - \frac{2n[GJ]s}{PD_1 \sqrt{1 - \left(\frac{x}{L} \right)^2}} \left(\sin^{-1} \frac{x}{L} - \frac{\pi}{2} \right) \quad (2.1)$$

Local coil response:

$$F = \frac{6E_1 I_1}{D_1^2} - \frac{3\pi^2 [GJ]s}{4PD_1} \quad (2.2)$$

Where:

F : force [N]

n : number of longerons [-]

D_1 : bottom ring diameter [mm]

x/L : deploying ratio to mast length

EI : bending stiffness [N mm²]

GJ : torsional stiffness [N mm²]

P : mast pitch (height between floors) [mm]

s : coordinate along a spacer [-]

Kitamura presents the mast response for the HL-1 mast as seen in Figure 2.23. This response data is compared to the idealised local coil mode with experimental data.

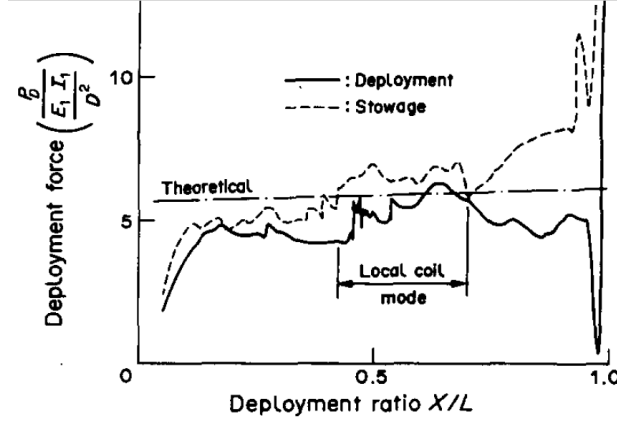


Figure 2.23: Kitamura analytical response formula shown with experimental data for HL-1 [45].

2.4. ADDITIVE MANUFACTURING

This thesis focuses on additive manufacturing (AM) for both micro- and macro-scale printing as the goal is to create a new metamaterial design with complex shapes that need to be scalable (from macro- to nano-scale). There are four other key manufacturing processes: (1) casting; (2) forging; (3) machining; and (4) joining. These are briefly discussed next to establish a baseline comparison with additive manufacturing.

Casting involves pouring a material in its liquid form into a mold and allowing it to solidify [53]. Forming encompasses changing the shape of some material while keeping the volume and mass the same. Examples of this are forging, rolling, extruding, pressing and bending [54]. Machining is a subtractive process by which material is removed [55]. Examples of machining processes are grinding, milling, cutting, turning, tapping. Joining is an additive process where through use of processes like welding, fastening, or chemical binding, several separate parts of material are combined into one [56].

The most commonly adopted method of manufacturing is using a combination of the four mentioned categories in separate steps to create the desired result. For mass production this can result in a short production time and low production cost per part, but

the high initial tooling costs make it unfavourable for small batches or unique parts [57]. Product scale also plays an important role, as many of the technologies that are mature for macro scale fabrication are not applicable or face specific challenges when considering smaller length scales. Traditional manufacturing often requires significant (time and financial) investments when creating highly complex geometries at small scales [58]. This is one of the cases where additive manufacturing provides significant advantages [59].

Additive manufacturing or 3D printing is the most recent branch of manufacturing. 3D printing creates a part by adding material layer by layer, so highly complex forms and geometries can be created. However, long manufacturing times [60], poor surface quality [61], anisotropic composition [62] and limited material choice, tend to make it more useful for prototyping after which production is carried out by the traditional methods mentioned above [60]. These challenges in 3D printing continue to be investigated by many research groups and there is a growing amount of literature in the subject. Hence, the importance of this fabrication process relative to others is expected to grow (expected 27% compound growth annually) [60, 63].

Additive manufacturing in its basic form consists of building up a component layer by layer. First developed by Charles Hull in 1986 the technology has recently received great interest by both media and research communities, which has led to significant progress [60]. Materials manufactured by additive manufacturing are characterized as having inferior mechanical properties and being highly anisotropic. Currently, this process has long manufacturing speed as compared with some large scale production methods (ex. injection molding), so it has not been adopted for mass production other than niche markets such as patient specific implants where each part is custom made to fit the patients needs [64]. To compete with traditional manufacturing the manufacture times will need to drop significantly. One company producing a printer which can print in minutes rather than hours is Carbon 3D (see Section 2.4.3) [65]. These lower manufacturing times make it attractive to use additive manufacturing for production in small quantities, as tooling costs are further reduced.

There are several different technologies currently used for 3D printing namely: SLA (stereolithography), powder bed fusion, FDM (fused deposition modeling), inkjet printing, and contour crafting (CC). These printing technologies can be used for a range of materials including ceramics, polymers (most common), and metals. Hybrid materials which can be printed have also been developed in recent years [66, 67]. This section briefly explains the working process and evaluates the benefits and disadvantages of each technology.

2.4.1. FUSED DEPOSITION MODELING

Fused deposition modelling (FDM), as illustrated in Figure 2.24 a), is now one of the most common methods of 3D printing and is used mainly for personal home use. The working method is as follows: a polymer filament is heated in a nozzle into a semi-liquid state and is extruded onto the previously printed layers. The mechanical properties of the printed parts are affected by: the thermoplasticity of the polymer filament, layer width, thickness, air-gap, and printing material [68]. Weaknesses of this technology in-

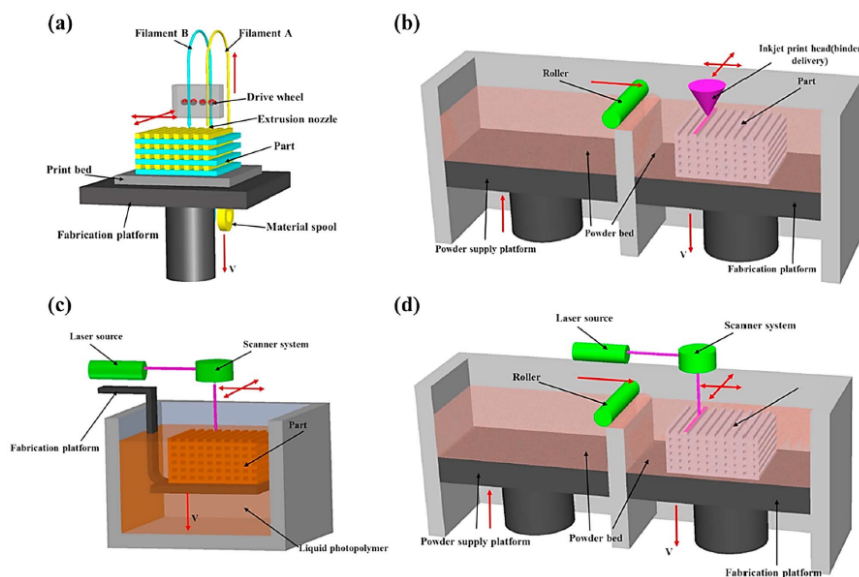


Figure 2.24: Schematic diagrams of four main methods of additive manufacturing: (a) fused deposition modelling; (b) inkjet printing; (c) stereolithography; (d) powder bed fusion [5]

clude interlayer distortion [69], high surface roughness [70], and a limited amount materials choice (thermoplastic polymers) [68]. The two most common materials which are printed with FDM are polylactic acid (PLA) and acrylonitrile butadiene styrene (ABS), however some printers, including the Ultimaker 3 [71], can also print other materials such as nylon or even multiple materials such as dissolvable supports. Research is also being done to strengthen the mechanical properties of FDM parts by incorporating composites [72], however anisotropic weakness caused by poor inter-layer adhesion and void formation make it challenging to use FDM in production; thus FDM is used for prototyping [73].

2.4.2. STEREOLITHOGRAPHY

Stereolithography – Figure 2.24 c – was one of the earliest methods of additive manufacturing [73]. It uses ultraviolet light (UV) or electron beams to convert a liquid monomer or resin locally to a solid. This happens due to the monomers or resins being UV active, and instantly convert to polymer chains after being activated. After printing, the unreacted resin can be removed and a post process, curing, can increase surface finish and mechanical performance [60]. The main factors contributing to the structure and therefore mechanical properties are the energy of the light source, exposure, and material choice [74]. Advantages of SLA is that they can be printed in very high resolution (as low as 10 micron) [75]. This means it can be effectively used for the production of nano-composites [63]. The disadvantages include that SLA is slow, expensive, and has a

very limited range of printable materials.

2.4.3. CLIP: CONTINUOUS LIQUID INTERFACE PRODUCTION

A recent breakthrough in printing technology is that the print speed has been dramatically increased by using oxygen to assist the curing of the resin. This technology, patented by Carbon3D inc. [76], uses continuous liquid interface production (CLIP) – Figure 2.25. CLIP works by projecting UV light through an oxygen permeable window underneath a liquid resin bath [65]. An oxygen-inhibited dead zone created above the window maintains a liquid interface below the advancing part. As the part is drawn out of the bath, it naturally creates suction forces underneath which will be filled with new resin. This is an evolution of stereolithography mentioned above. The continuous pulling process means parts can be produced in minutes (500 mm/hour) rather than hours [65].

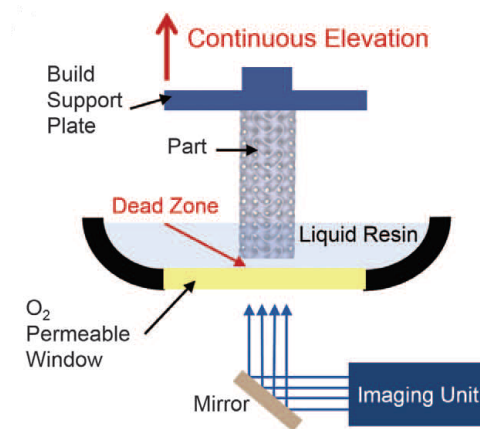


Figure 2.25: Overview CLIP printing [65]

2.4.4. POWDER BED FUSION

Powder bed fusion – Figure 2.24 d – combines aspects of both FDM and SLA. Rather than using a liquid polymer or filament it uses a laser or liquid binder to bind powdered material. For each layer, new powder is added on top of the previous layer after which the laser or liquid binder locally solidifies material where desired. It is not recommended for parts to be entirely closed (hollow), as after the printing process the excess powder needs to be removed. Selective laser sintering (SLS) is a subclass of this technology using a laser to either fully melt or sinter the powdered material. SLS is a common way in which to manufacture small scale (several cm) metal parts. Powder size and type, distribution and packing determine the end properties of the product [77]. In the case of liquid binder, the factors include size and shape of powder, deposition speed, the interaction between powder and binder, and post processing [75, 77]. Liquid binder should be considered if the powdered material has a too high melting/sintering temperature [60].

2.4.5. INKJET

Inkjet printing – Figure 2.24 (b) – is one of the main methods for printing with ceramics. This method works by creating a ceramic suspension (for example in water) [78], and is deposited in form of droplets onto the previously printed layer where they then solidify. This method is fast and efficient with a high resolution. The main printing factors for this technology include particle size, extrusion rate, viscosity of ink, nozzle size and speed of printing [79].

2.4.6. DIRECT ENERGY DEPOSITION

Direct energy deposition is a printing technology which locally melts powdered or filament material directly onto underlying layers. This is usually done with laser or electron beam depending on the material and precision required [80]. This technology along with contour crafting is primarily used for large products and thus will fall outside the scope of this thesis.

2.4.7. LAMINATED OBJECT MANUFACTURING

Laminated object manufacturing (LOM) is an AM technology which is unlikely to ever be used for metamaterials as it is more applicable to larger scale objects. However, it is one of the most commercially viable AM technologies and so is interesting to discuss. It works, as the name suggests, by repeatedly cutting (in a desired shape) and layering a new layer of material, joining it to the previous layer. LOM has been used in industries for smart structures, electronics, foundry and even paper manufacturing. It is the only method for creating metal structures at room temperature [81, 82]. It can be used for composites, ceramics, polymers, metals, and paper. The downsides to this technology are its low dimensional accuracy when compared to powder bed fusion, inferior surface quality, difficulty in removing excess material in a time efficient manner for complex shapes, and a need to recycle the excess material instead of reusing it as in SLA and powder bed fusion [60].

Methods	Materials	Applications	Benefits	Drawbacks	Resolution range (μm)
Fused deposition modelling	Continues filaments of thermoplastic polymers Continuous fibre-reinforced polymers	Rapid prototyping Toys advanced composite parts	Low cost High speed Simplicity	Weak mechanical properties Limited materials (only thermoplastics)	50-200 μm
Powder bed fusion (SL, SLM, 3DP)	Compacted fine powders Metals, alloys and limited polymers (SLS or SLM) ceramic and polymers (3DP)	Biomedical Electronics Aerospace Lightweight structures (lattices) Heat exchangers	Fine resolution High quality	Layer-by-layer finish Slow printing Expensive High porosity in the binder method (3DP)	80-250 μm
Inkjet printing and contour crafting	A concentrated dispersion of particles in a liquid (ink or paste) Ceramic, concrete and soil	Biomedical Large structures Buildings	Ability to print large structures Quick printing	Maintaining workability Coarse resolution Lack of adhesion between layers	Inkjet: 5-200 μm Contour crafting: 25-40 mm
Stereolithography	A resin with photo-active monomers Hybrid polymer-ceramics	Biomedical Prototyping	Fine resolution High quality	Layer-by-layer finish Very limited materials Slow printing Expensive	10 μm
Direct energy deposition	Metals and alloys in the form of powder or wire Ceramics and polymers	Aerospace Retrofitting Repair Cladding Biomedical	Reduced manufacturing time and cost Excellent mechanical properties Controlled microstructure Accurate composition control Excellent for repair and retrofitting	Low accuracy Low surface quality Need for a dense support structure Limitation in printing complex shapes with fine details	250 μm
Laminated object manufacturing	Polymer composites Ceramics Paper Metal-filled tapes Metal rolls	Paper manufacturing Foundry industries Electronics Smart structures	Reduced tooling and manufacturing time A vast range of materials Low cost Excellent for manufacturing of larger structures	Inferior surface quality and dimensional accuracy Limitation in manufacturing of complex shapes	Depends on the thickness of the laminates

Table 2.1: Overview of additive manufacturing technologies [60]

Another concern when designing parts for additive manufacturing is the material choice. Each AM technology can only print certain materials, and for each materials the finish and material properties will change. This is especially true when the parts have small length scale features. For example, of the near 5500 different metal alloys only a handful can be used in AM [83]. This is explained by inadequate micro structure formation such as columnar grains and micro cracks after melting and solidifying [84]. Due to this and a very similar situation when printing in polymers and composites, new research is being conducted to creating various materials and producing methods for manufacturing advanced polymer composites with a better overall performance [75, 85].

2.4.8. MICROSCOPIC ADDITIVE MANUFACTURING

The current trend of miniaturization drives the need for micro- and nano-scale manufacturing. Various technologies have been developed for manufacturing at these scales, including lithographic and non-lithographic methods, microengineering, and micro-manufacturing. However, contrary to conventional manufacturing methods, additive manufacturing becomes the more attractive technology at these scales [86]. This is in part due to the ability to process a relatively broad range of materials and fabricate functional and geometrically complicated 3D microstructures [59]. Vaezi et al. suggested that 3D micro additive manufacturing can be split into three categories: scalable additive manufacturing, 3D direct writing (DW), and hybrid processes [59]. Scalable additive manufacturing includes technologies such as stereolithography, selective laser sintering, and inkjet printing. 3D direct writing encompasses ink based DW, laser transfer DW, and Beam deposition DW. Lastly, hybrid processes such as electrochemical fabrication and shape deposition modelling can be used [59]. This review will focus solely on the

technology which the project will have access to which is direct laser writing used by the Nanoscribe.

The Nanoscribe uses direct laser writing to locally convert photosensitive materials. It uses non-linear two photon absorption, which means that the photo-sensitive polymer gets locally (3D pixel known as voxel) excited to a higher energy state with near-infrared light causing it to solidify [87]. The resolution and voxel size are determined by the size of the laser focus spot within the material. The power of the laser and the material properties also affect the voxel size. In order to achieve nano-meter accurate resolution a high numerical aperture is used [88]. There are two approaches to move the voxel to different locations in the material. Fixed beam moving sample where the print bed is moved in three dimensions via piezo actuators, moving beam fixed sample, where the laser is scanned by galvanometric mirrors. This second approach allows for much faster layer-by-layer fabrication speeds [88]. Using this technology the Nanoscribe can print structures with 100 nanometer accuracy, on a 200 micron by 200 micron build surface.

2.5. DATA-DRIVEN COMPUTATIONAL DESIGN

The work presented herein aims to create a new material which is both highly compressible whilst having a high compressive stress. What makes this work particularly relevant is the design of the structure is being developed in a novel way by using a data-driven computational framework. This framework creates a multi-dimensional design space in which several failure modes can be addressed, and the effects of certain parameters can be visualized. In essence it allows the designer to rely less on intuition and more on quantitative data. The original framework proposed by Bessa [7] is first presented here. For an in-depth look into the data driven framework see Chapter 3.2.

1. A Design of Experiments is constructed with a set of discrete variables. These variables are given certain realistic bounds to minimize computational costs. X number of sampling points are taken from large number of combined variables within the design space. For example, in the original article the ultra-thin deployable carbon shell was parametrized with two variables, the angle θ and the height h , and then the design space was sampled by a Sobol sequence
2. Of the X selected combinations, see Figure 2.26, a computational analysis is performed using the commercial finite element (FE) software, in this case Abaqus. From these simulations the relevant data (in this case buckling moments [7]) is extracted and a database constructed. This data shows the relationship between certain variables and the resultant structural properties.
3. When the properties of interest (buckling moments) are uncertain, e.g. due to geometric imperfections, the input-output relationships needed for design of the structure should be determined with Bayesian machine learning since the data is noisy.
4. After the machine learning step, a multi-dimensional design space is constructed based on the number of variables, with various material behaviour zones. These design charts show the influence of the parameters of interest on structure re-

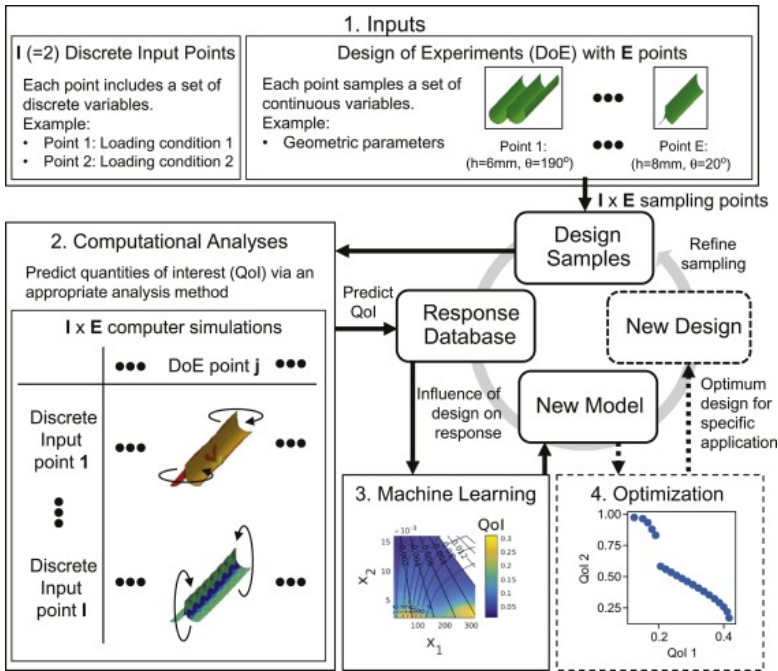


Figure 2.26: Data-driven framework applied to structural modeling and design of an ultra-thin deployable carbon shell [7]

sponse, and shows the bounds for parameters in which the structure is able to function.

The above summary is very brief and provides merely an overview of the data driven framework. An elaborate explanation of this framework as applied to the highly compressible metamaterial can be found in Chapter 3.

2.6. KNOWLEDGE GAP, AIMS AND OBJECTIVES

Creating a highly deformable stiff material is not trivial and natural materials only get us so far. To surpass the state of the art a creative structure needs to be designed. The literature presents several metamaterial structures which perform relatively well under uniaxial compressive load, most notably that of Cao et al. [44]. This is fundamental research and had not yet been adapted for practical applications. A gap in the literature is identified for a stiff, highly compressible material (>83% strain) which can be implemented into a three dimensional lattice. A data driven framework presented by Bessa et al. provides a novel approach to achieving an optimal design.

After reviewing the state of the art and determining where there are current gaps in the research the following research question is established.

The objective of this research is twofold: one, to lay the building block for the underlying structure of a metamaterial which is both highly deformable and has a high compressive strength, utilizing additive manufacturing to create the metamaterial structure, and two, further validate the data driven design framework approach for a highly complex structure.

The research will be focused around a data driven design framework, in which a design is fully simulated and optimised before manufacturing. The computational component of this design process is carried out by another master student (Piotr Glowacki). This thesis focuses on validating the design process, by manufacturing the structure and testing it under compressive load. The analytical model presented by Kitamura [45] will also be validated and used as a secondary analysis tool for the mast.

This project will have a strong practical component, focusing on the material design, coming to grips with the properties of materials used, and using machine learning as a tool to determine the optimal design space for a certain purpose.

For the main research part of the project in developing a new metamaterial structure the following research questions are introduced:

1. Can the design charts attained by the data-driven process be used to guide the experiments?
2. Can the data-driven process propagate the uncertainty of the base material including its properties and the manufacturing process?
3. Is a coilable mast a viable candidate for use in a unit-cell of a highly compressible material?

3

DATA DRIVEN FRAMEWORK APPLIED TO A BUCKLING MAST

THIS study strives to validate the data driven design approach. The conventional way in which structures are designed is to use intuition and experience to make a design, then to construct and test that design, fixing problems in subsequent iterations. Once completed, either a Finite Element Model or an analytical model is then used to support the obtained results. The data driven approach reverses this conventional method by first simulating the structure, varying several key parameters. The results of the data driven process are several design charts guiding the designer, decreasing the importance of intuition or experience. Mechanical testing is mainly used to validate the data driven output, hereby saving resources and time for highly complicated structures.

This chapter will first introduce the unit cell on which the metamaterial is based. The data driven framework and process will then be explained, concluding with an analytical model presented by Kitamura [45] which can be used to further validate the findings.

3.1. PROPOSED METAMATERIAL CONCEPT

A metamaterial consists of many repeated unit cells arranged in a lattice structure. The unit cell considered in this project is a mast design which is derived from the Astromast coilable boom, shown in Chapter 2.3. This coilable helical boom is made up of several bays which are interconnected via vertically oriented rods known as longerons. The Astromast is able to achieve a compressive strain in the order of 99%. However, the Astromast structure contains many linkages and moving parts, that would make it impractical for adaptation into a metamaterial. Here, the astromast is simplified by considering a single bay, decreasing the number of design variables and improving the suitability of the design for fabrication by additive manufacturing.

The metamaterial unit cell concept is shown in Figure 3.1 (left). This metamaterial is comprised of two identical mirrored structures, henceforth referred to as the half-mast (HM). This study focuses on the half-mast design. As the unit cell contains two identical mirrored half-masts, finding an optimal design for the half-mast results in a optimal design for the metamaterial.

As can be seen in Figure 3.1, the half-mast is based on several input variables: the bottom ring diameter D_1 , the top ring diameter D_2 , the longeron diameter d , and the pitch P (distance between floors). Inputs D_1 and D_2 refer to the pivoting point on the longeron, and not the outer diameter of the supporting ring. This is an important distinction as hinges are not modelled in the finite element analyses. Figure 3.4 shows one representation of a mast design in Abaqus.

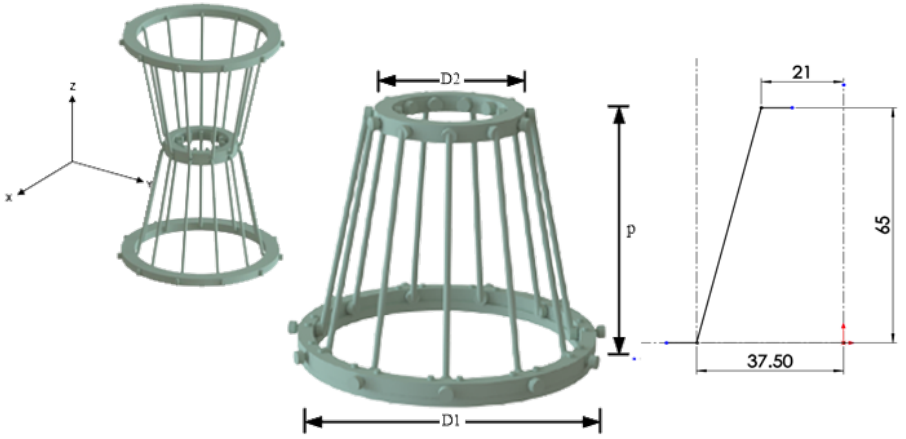


Figure 3.1: (Left) Unit cell of metamaterial with free rotating middle segment, (Middle) Simplified half-mast building block which will be used for both simulations and practical testing, (right) An example of core dimensions for the longeron

3.2. DATA DRIVEN APPROACH

This section presents an overview of the data driven approach briefly presented in Chapter 2.5 and applied to the half-mast structure. Figure 3.2 shows an overview of data driven framework, after-which each step of the framework will be covered in detail.

Remark 3 *The following information is a summary of the data-driven computational framework created by Bessa et al. [6, 7] and implemented for the metamaterial design by Glowacki [89]. Glowacki presents a 7 parameter model which includes additional variables (I_x , I_y , J_T , and G/E). To simplify the problem for practical testing these variables will not be considered. The reader is referred to the original articles for further details [6, 7, 89]. In this thesis we explore and validate the results of the data-driven investigation in order to prove its predictions and the feasibility of manufacturing the new metamaterial.*

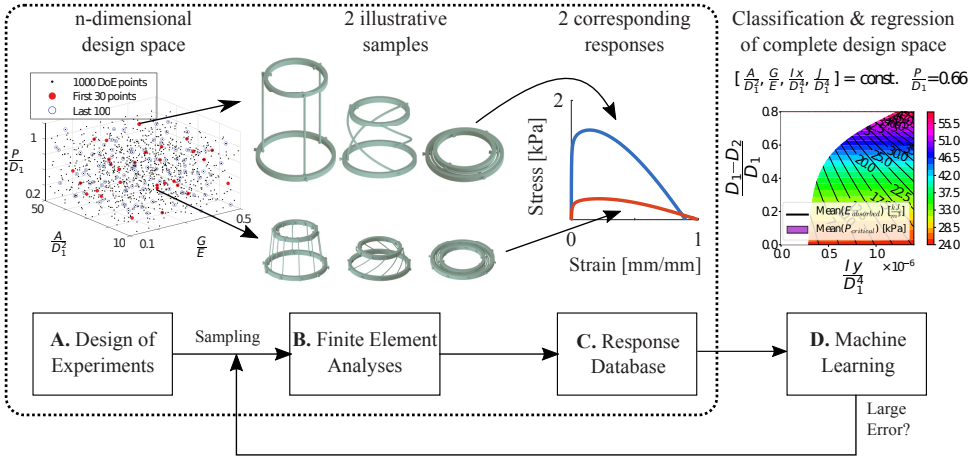


Figure 3.2: Data-driven design of a super-compressible metamaterial building block using 7 design variables.

3.2.1. DESIGN OF EXPERIMENTS

Step one of the data driven framework is to create a design of experiments in which many half-mast parameter combinations can be made. The half-mast is specified by the following set of parameters which are bounded. These parameters are all normalized with respect to D_1 i.e. properties are scale independent. The following inputs are necessary to define the design:

1. D_1 , Bottom ring diameter [mm]
2. D_2 , Top ring diameter [mm]
3. d , Diameter round cross-section of longeron [mm]
4. p , Pitch (height between bays) [mm]

Material properties Young's modulus (E) and Shear modulus (G) of the longerons are chosen as constants. The longerons are the main load carrying component, so the force changes proportionally with the number of longerons. This is assuming that there is no interaction between longerons (longerons do not make contact when the half-mast is fully compressed). If the number of longerons is large with respect to D_1 then non interaction can no longer be assumed.

Table 3.1: Bounds for continuous variable inputs

Variable	A [mm ²]	P [mm]	$D_r = \frac{D_1 - D_2}{D_1}$
Upper Bound	40.96	150	0.8
Lower Bound	0.1171	25	0

By implementing the above mentioned parameters and bounding them, a design space

is created. Sampling this design space is done using a Sobol sequence (Figure 3.3). The Sobol sequence samples the design space creating many half-masts each consisting of different parameters, offering a good balance of randomness and regularity. For more details on sampling with regard to this problem the reader is directed towards Glowacki [89].

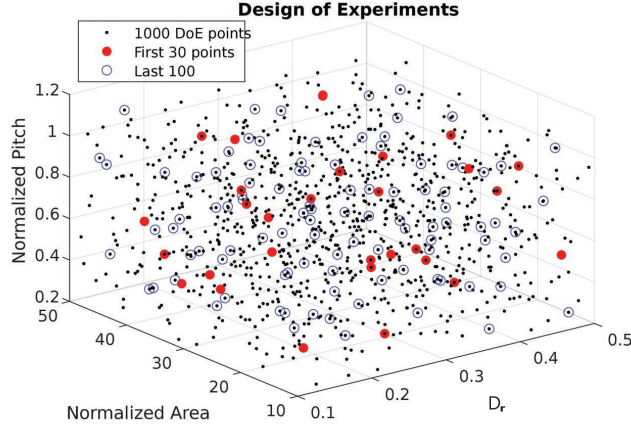


Figure 3.3: Visualisation of the Sobol sequence across 3 parameters for sampling the design of experiments

3.2.2. FINITE ELEMENT ANALYSIS

Each metamaterial design (each DOE point) is simulated with the finite element method. A combination of the above mentioned variables (D_1 , D_2 , P , d) are selected within the bounds using the Sobol sequence. This mast is then constructed and simulated using FEM in Abaqus. The simulation consists of two parts. First, a linear buckling analysis of the half-mast in the un-deformed state, gives estimates of buckling loads and modes. Second, an implicit static simulation using the arc-length method is performed providing the response data during compression.

In the Abaqus model, each longeron is represented as two nodes connected by a line. This line is then assigned a cross section profile (in this case round) and material properties. The nodes are freely rotating without friction see Figure 3.4. The bottom ring is fixed whilst the top ring is unconstrained. All nodes of the top and bottom rings are kept in the same respective planes.

A vertical force is applied to the mast upon which it buckles. The manner in which it buckles can differ, and if any buckling mode other than twisting dominates, the mast is labelled as non-coilable. An overview of the buckling modes can be seen in Figure 3.5, naturally Mode-1 is the desired mode of buckling. After the initial buckle the implicit static simulation is initiated where a force response of the mast is generated through a full compression.

Lastly, the data which is of interest is then extracted (in this case its the buckling load and energy absorption). This data can be used to construct classification and regression analyses giving the designer insight into the effects of various parameters (see Section 3.3).

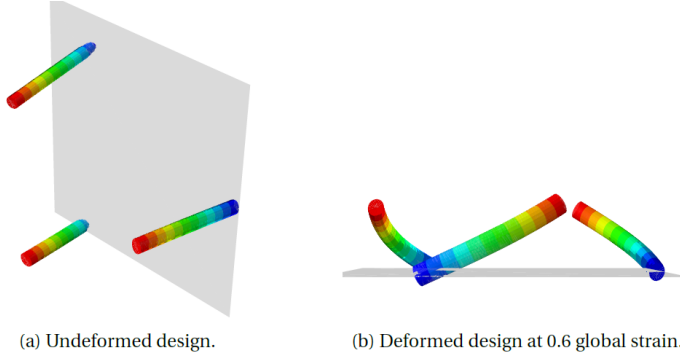


Figure 3.4: Visualisation of mast model in Abaqus which consists of centerline and cross-section. Support rings or hinges are not included

3.2.3. GEOMETRIC IMPERFECTIONS

The half-mast response behaviour in its basic form is imperfection free. In reality this is not the case. Several examples of global buckling modes can be seen in Figure 3.5. These modes can be used to seed geometric imperfections into the idealized (and undeformed) geometry of the metamaterial. The impact of such imperfections is unknown a priori, so quantifying the uncertainty caused by them is important when predicting the half-mast response because the mechanical metamaterials explore buckling – an imperfection sensitive phenomena. Furthermore, each design from the DOE usually has different sensitivity to these imperfections.

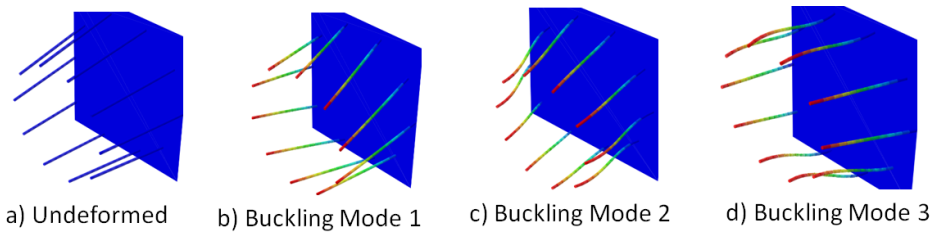


Figure 3.5: Imperfection Modes that affect the response of the mast under loading.

Preliminary half-masts show that the most significant geometric imperfections coincides with the buckling Mode 1. Thus Mode 1 buckling is chosen to seed all of the imperfections. Different half-masts manufactured from the same design will not be identical due to slight variations of the manufacturing process and environmental conditions. A lognormal distribution is chosen to seed the imperfection with a mean of 4 degrees

with a standard deviation of 1.2 degrees. A lognormal distribution ensures randomness between each simulated half-mast, as is the case in practice, whilst giving preference to smaller deviations. The mean and standard deviation are also based on preliminary half-masts. Mode one error increases as longeron diameter decreases or pitch increases.

3.2.4. RESPONSE DATA

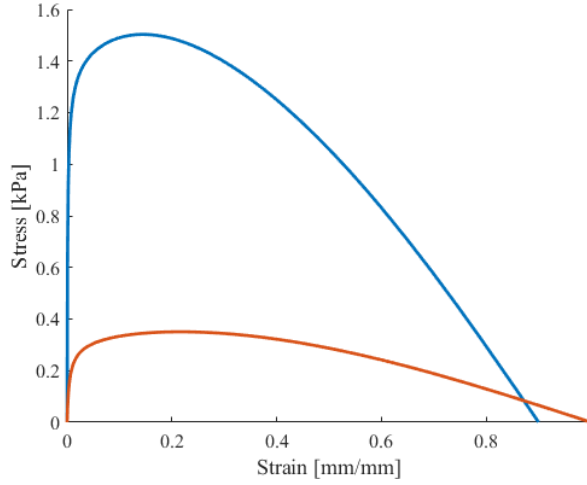


Figure 3.6: Mast response for one parameter combination with no imperfections

Figure 3.6 shows the response curve extracted from Abaqus output data for two combinations of half-mast parameters. Furthering this, we can introduce imperfections into the simulations. Figure 3.7 shows the variance of the response data, based on various mode-1 imperfection angles simulated on a single half-mast design showing the significance of imperfections on the response.

3.2.5. MACHINE LEARNING

The way in which machine learning is implemented with respect to the buckling half-mast is presented. First a database spanning the design space was used in order to classify the half-mast into two categories: coilable and non-coilable. All half-mast designs which are classified as non-coilable are not taken into account in the next steps.

A RIKS analysis (arc-length method) is used to obtain the stress strain data from Abaqus [89]. The remaining points are used with performing a regression analysis on both critical buckling load, and energy absorbed. A sensitivity analysis is also performed on the regression model to gain insight on the relationships between certain parameters on the half-mast response.

The design of a metamaterial with a large number of parameters poses significant challenges especially when including uncertainty quantification. For large multidimensional

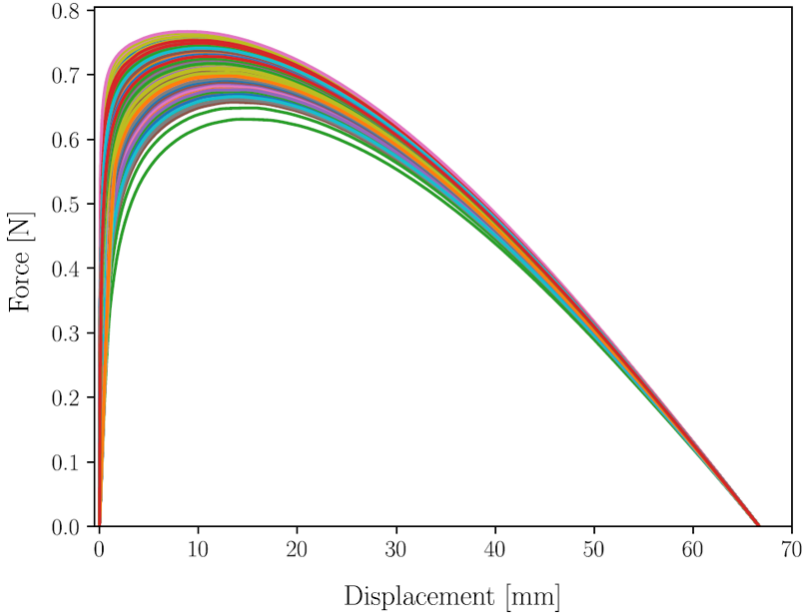


Figure 3.7: All possible inflections seeded on single half-mast design

datasets classifiers such as Sparse Variational Gaussian Process (SVGP) are used as well as Sparse Gaussian Process Regression (SGPR) for regression analysis [89]. In this case, using a 4 parameter model (D_1 , D_2 , P , d) the classification can be done using a support vector machine (SVM) algorithm and neural networks for regression. For further information please consult referenced articles from Bessa and Glowacki [6, 7, 89].

3.3. DESIGN CHARTS

In Figure 3.8 the design classification of the 4 parameter model is shown. The boundaries separate 3 classifications: Not Coilable, Coilable, and Coilable but Yields. A half-mast is classified as Not Coilable if the first buckling mode is not the desired twisting mode. This is influenced both by pitch (P) and D_r . The second boundary shows whether or not the material will yield. For the chart this threshold is 3.3% strain. This strain limit is taken from the Ultimaker quoted yield limit of their PLA [90]. Their limit is obtained using ISO 527 specimen tests with 90% infill printed specimens. Whether the Ultimaker quoted properties provide a reasonable representation of all 3D-printed structures is unlikely. In order to validate these assumptions we will investigate the properties of our own manufactured FDM parts in Chapter 4.

Figure 3.9 shows the impact of the four parameters on the critical buckling load, and energy absorption. The zone over which the regression is plotted is shown Figure 3.8 with dotted region. For just four parameters the information conveyed by the regression

plot may seem somewhat trivial with thicker longerons resulting in higher stress. Where these plots become particularly useful is when increasing the number of parameters in the model. Glowacki [89] further represents I_x , I_y , E/G , and J_T as free variables resulting in a 7 dimensional design space. His findings show that variables such as I_x and I_y have a great influence on the compressive strength of the metamaterial. These results can be seen in Appendix F.

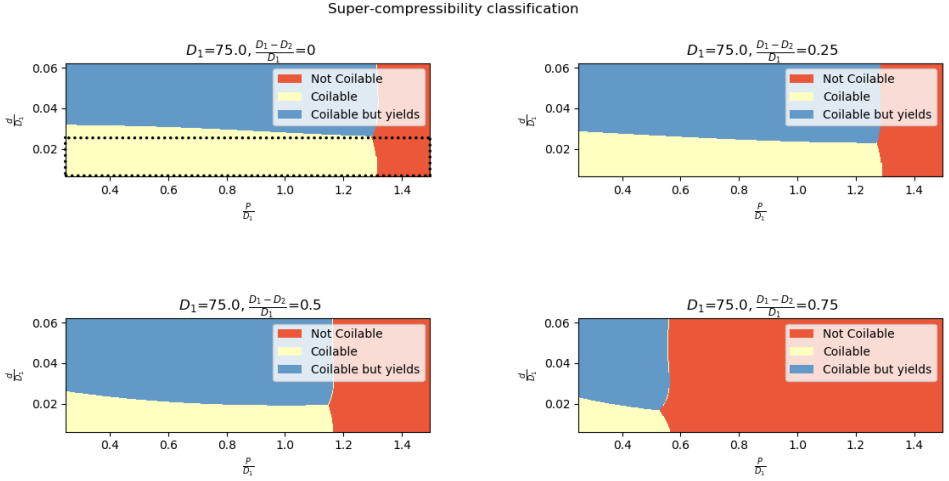


Figure 3.8: Coilability classification using strain limit to classify plasticity, black dotted section range over which regression plots are made

The design space considered herein only has three features: P/D_1 , d/D_1 , and $(D_1 - D_2)/D_1$. Therefore, Figure 3.8 provides sufficient information to interpret the behaviour of the half-mast. An increase of $(D_1 - D_2)/D_1$, i.e. a decrease in the diameter D_2 of the top support ring, causes a decrease of the region where coilability without plasticity can occur (note the shrinking size of the yellow region in the figure). Two effects can be observed with increasing $(D_1 - D_2)/D_1$: (1) the top bound of the yellow region moves down and its slope decreases; and (2) the right bound of the yellow region moves left. This implies that decreasing the size of the top ring and increasing the height of the metamaterial contributes to an increase of the maximum local deformation, leading to premature plasticity.

3.4. ANALYTICAL MODEL

Kitamura et al. [45] derived a simplified analytical model of the Astromast response, i.e. assuming the longerons to be perfectly vertical ($D_r = 0$). The analytical model was presented in Section 2.3, but here it is further simplified because the designs considered in this dissertation only have one bay, leading to the following result:

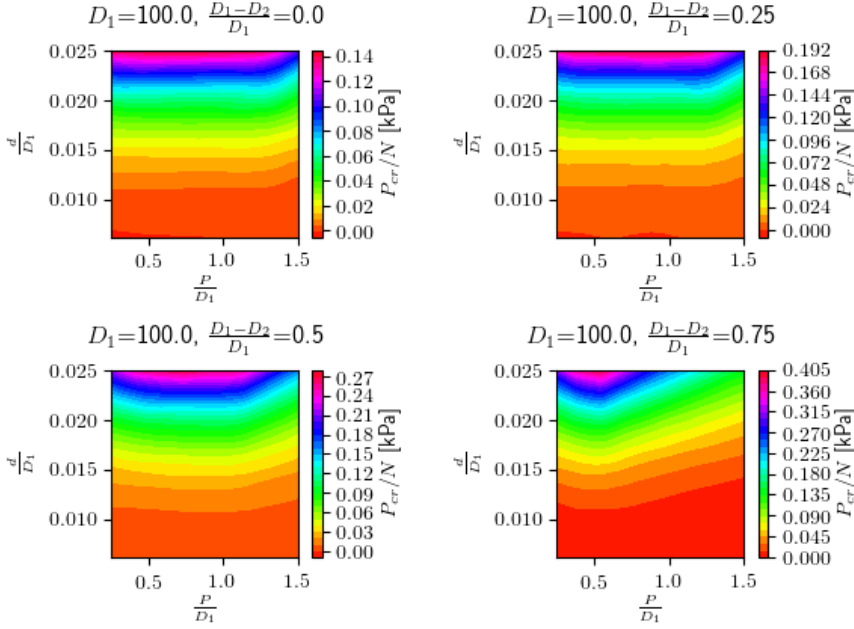


Figure 3.9: Regression plot showing impact of D_r , p and d on compressive strength shown per longeron. Range of regression is shown with black dotted lines in Figure 3.8

$$F = \frac{4nx}{D_1^2 L} \left[2E_1 I_1 \left\{ 1 - \left(\frac{x}{L} \right)^2 \right\} + G_1 J_1 \left\{ 2 \left(\frac{x}{L} \right)^2 - 1 \right\} \right] \quad (3.1)$$

where:

F : force [N]

n : number of longerons

D_1 : bottom ring diameter [mm]

x/L : deploying ratio to mast length

EI : bending stiffness [N mm²]

GJ : torsional stiffness [N mm²]

Figure 3.10 shows the influence of the input parameters in the analytical prediction of the post-buckling response of different mast designs obtained from Equation (3.1). Having an analytical model is useful as a means of comparison with the computational pre-

dictions and the experimental investigation later in this work. Note that the analytical model does not include the pitch influence.

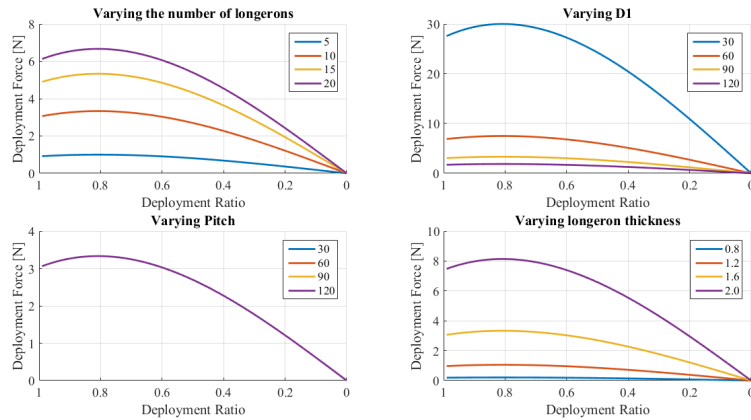


Figure 3.10: Kitamura Analytical equation with trends (top-left) Varying the number of longerons corresponding to a higher compressive force. (top-right) Varying the diameter of the mast with vertical longerons, (bottom-left) Pitch of the mast is only included into the bottom section of the Kitamura equation, as our metamaterial has no battens pitch does not affect the compressive force, (bottom-right) Increasing the longeron thickness results in a higher compressive force.

4

CHARACTERIZING THE MATERIAL

ADDITIVE manufacturing provides significant freedom for fabricating parts with complex shapes. As the main goal is to additively manufacture the new metamaterial concept, the first step is to select an appropriate 3D printer. Four printers are available for this project, the Ultimaker 2 [90], EnvisionTEC Per factory 4mini XL [91], EnvisionTEC Micro Plus Hi-Res [91], and the Nanoscribe [39, 59, 92, 93]. Given the availability of the Ultimaker 2 at the Mechanical, Maritime and Materials Engineering faculty, as well as its low operating cost, it was decided to focus on this printer for the first exploratory work. Polylactic acid (PLA) is the base material of choice, also due to its availability.

Table 4.1: Material properties of bulk PLA [94]

Material property	Units	Value
Density (ρ)	g/cm ³	1.24
Elastic modulus (E)	MPa	3500
Shear modulus (G)	MPa	1287
Poisson's ratio (ν)	-	0.36
Yield strength (σ_y)	MPa	70
Ultimate tensile strength	MPa	73
Elongation	%	7

The Ultimaker 2 is a fused deposition modelling (FDM) printer, so it introduces anisotropy into the material, despite bulk PLA being isotropic – Table 4.1 shows the properties of bulk PLA. The layers of the FDM printed part therefore behave as unidirectional fibre reinforced composite plies [95]. The presence of manufacturing defects such as voids implies that the PLA will have a mesostructure that leads to different material properties when compared to bulk PLA. These material properties are not deterministic; instead, they are statistical. Therefore, this chapter focuses on characterizing the PLA base material in order to provide the necessary information to make predictions about the

behaviour of the metamaterial, since elasticity and yielding information is required to design a recoverable and highly compressible structure.

The Ultimaker quoted material properties were used to obtain the initial classification charts (Figure 3.8). It cannot be assumed that these values are fully representative as 3D-printed PLA is highly anisotropic and sensitive to printing settings. This chapter aims to understand fully the material properties of the longerons to improve the accuracy of the simulations. Section 4.1 introduces the mesostructure of the longeron created by the printer. Section 4.1.2 presents the results of tensile testing different shaped specimens. This is followed by sections 4.3 & 4.4, analysing the compression and shear properties respectively. Lastly, a yield surface for the material is presented in section 4.5.

4.1. MESOSTRUCTURE CHARACTERIZATION

The longerons of the metamaterial printed in PLA are not completely solid. Instead, their mesostructures are porous, which explains the anisotropic behaviour of the printed material. The FDM printer melts the bulk PLA and extrudes it in thin filaments known as roads. Each road is extruded on top of previously printed material. This material can be best visualized as a composite, with the fibres all running in a single uniform direction see Figure 4.1. Understanding the microstructure of the longerons and measuring the variability of their geometry caused by the manufacturing process is key to understanding the propagation of uncertainty to the properties of interest. For details on the print properties and variables which affect print quality, see Appendix B.1.

A small diameter of the longeron cross-section is necessary to avoid plastic deformation. This scale is determined by the initial design charts using Ultimaker PLA properties. 3D-printing a longeron at this scale (1 – 3 mm diameter) is at the limit of what the Ultimaker 2 is capable of producing. This makes the design more susceptible to printer defects, increasing the variance of the properties.

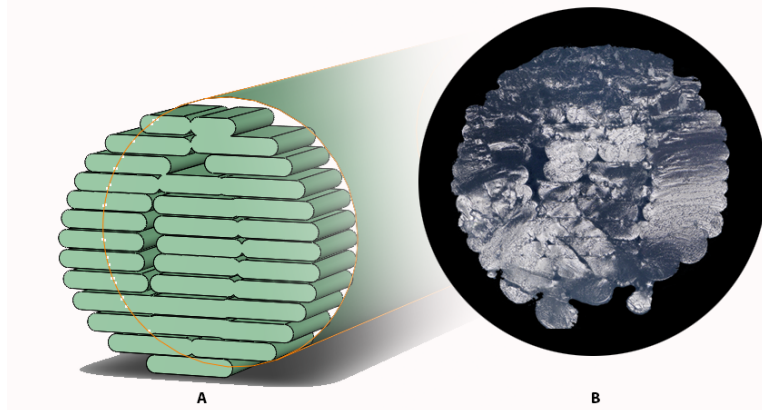


Figure 4.1: Structure of longeron after 3D-Printing with Ultimaker 2 using layer height of 0.1 mm

4.1.1. IDEAL PACKING

A complete study into the effects of print properties on the material properties falls outside the scope of this thesis, although some insight may be gained about this topic. The weakest component of a FDM structure is the bonding between adjacent roads. For this reason, if one would like to optimize material properties, the roads should be as large as possible with the fewest number of voids between them [95]. Figure 4.2 crudely demonstrates the ideal manner in which to print a longeron. However, this then results in a rough surface and non-circular shape.

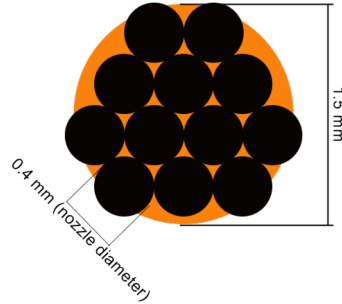


Figure 4.2: Idealized roads for maximizing longeron properties on Ultimaker 2 with 0.4 mm nozzle, where orange represents a 1.5 mm diameter longeron cross section

4.1.2. LONGERON MESOSTRUCTURE ANALYSIS

Several articles have investigated the effects of print settings on the material characteristics. Floor et al. [96] investigates several fill patterns and fill percentages for the Ultimaker 2. They conclude that 100 percent infill with unidirectional fibres results in the largest Young's modulus. Ahn et al. [97] show the effect of different printing orientations of the specimens on the print bed, resulting in the strongest part being oriented in the x or y direction. They also explore how stress concentrations arise from the fill pattern and visualize the different porosities caused by different print setting.

In this thesis, several microscopic images were made of a longeron along its length in order to understand their underlying structure and porosity. Figure 4.1 shows one such image, of the 8 cross sections which were analysed. An analysis of the dark holes is done to determine porosity using a pixel based image analysis tool (SketchandCalc area calculator). The temperature of half the longerons is lowered with liquid nitrogen to make the material more brittle before snapping. This was in order to minimize plasticity caused by the snapping action. The other half of the longerons is not cooled before snapping to verify whether the contraction and expansion of the cooling process affects the porosity. Appendix C.3 shows several microscopic images of longeron cross-sections.

The porosity of a 1.5 mm longeron is an average of 4% of the total area. A bigger contribution to the difference between an idealized cross-section and the printed one is at the perimeter of the print structure (see Figure 4.3). This is due to the additive nature of FDM

Table 4.2: Average cross sectional diameter (\bar{d}) measured with Mitutoyo micrometer and Keyence VHX-5000 digital microscope with porosity obtained via pixel based image analysis

	\bar{d} measured with micrometer [mm]	\bar{d} measured with microscope [mm]	Porosity [%]
Average	1.608	1.482	4.064
Standard deviation	0.024	0.057	0.667

which produced a rough surface when printing on small scale. When measuring using a micrometer (Mitutoyo Absolute Digital Micrometer QuickMike 0-30mm) with a circular cross section tip of 2 mm diameter and an accuracy of $\pm 2\mu\text{m}$, the average of 6 measurements is taken for each cross section. This method measures the largest diameter at any one point. A comparison with the diameter found using the Keyence VHX-5000 series digital microscope (see Figure 4.3) shows a systematic measurement error of 1.26 mm. These errors will be taken into account during material testing.

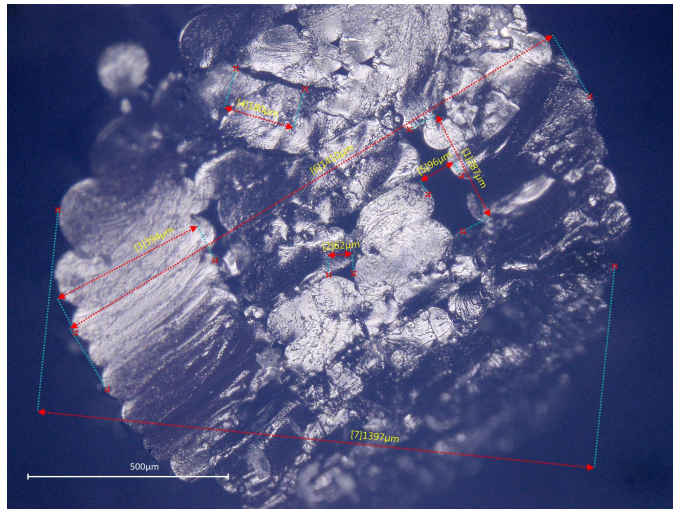


Figure 4.3: Porosity of longeron layer height of 0.1 mm

4.2. CHARACTERIZATION OF 3D PRINTED MATERIAL PROPERTIES

The increased popularity of 3D-printing has led to several papers analysing the properties of 3D-printed parts. The most commonly quoted property is the tensile Young's modulus which is used to compare different printers and printing materials. FDM parts are not generally used in load bearing conditions, and there is insufficient literature on simulating the mesostructure of a FDM generated structure. For this reason, before optimizing the design it is essential to have a thorough understanding of the material

which is being used. Several papers [96–101] have studied the effects of print settings on both PLA and Acrylonitrile butadiene styrene (ABS) and the effects of printing orientation.

Torres et al. [94] presents the properties of PLA before printing, as seen in Table 4.1. These properties are of bulk PLA before being extruded by the printer nozzle. This is a baseline for which to compare the measured values for both Young's and shear moduli of the longerons.

4.2.1. UNIAXIAL TENSILE TESTS

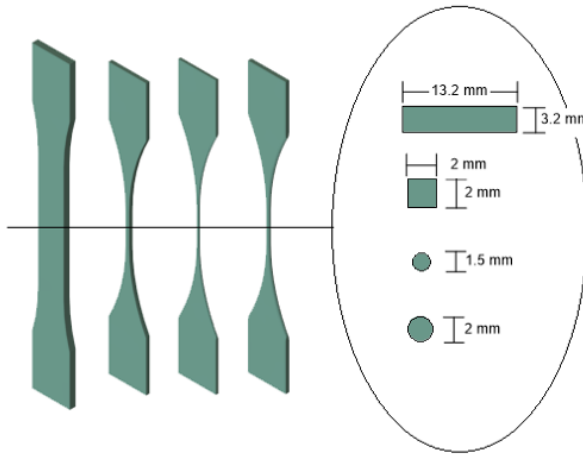


Figure 4.4: Tensile testing specimens with cross section dimensions

Ultimaker reports that their printed PLA has a Young's modulus of 2,346 MPa [90, 96] but only for the following settings: 90% infill, 0.1 mm layer height, with a fill pattern of ± 45 deg. As expected, this property is lower than the one obtained for bulk PLA – see Table 4.1 – approximately 3500 MPa. The difference between these values can be partially attributed to porosity in the printed material, layer height and fill, and potential additives to the PLA used to aid printability or provide colour.

The standard testing specimen used by articles testing tensile properties of plastics is the ASTM D638-14 or the equivalent ISO 527-12. Here the same norms are followed to create the specimens according to Figure 4.4. This standard test was conducted with 100 percent infill and a layer height of 0.1 mm with custom print settings (see Appendix B.2).

Since FDM mechanical properties are scale and shape dependent according to the orientation and cross section of the roads with respect to the specimen, tension testing was conducted on dog-bone specimens with smaller cross sections (Figure 4.4). Samples with 1.5 mm and 2 mm round cross sections, as well as 2 mm square cross sections

were produced as shown in Figure 4.4. While a 1.5 mm square cross section was also produced, it failed due to a stress concentration caused by a small void in the fillet region.

Figure 4.5 shows the stress-strain response obtained for the specimen following the ASTM D638-14 norm and considering unidirectional fibres with 100% infill. An important note about these results is that they include the raw measurements for the tests conducted, where in order to avoid damaging the strain-gauge, it was removed before the specimens failed, creating an artificial elbow due to the miscalibrated load cell of the mechanical testing device. The corrected average curve is plotted above the raw data, including the 95% confidence interval (two standard deviations). See Appendix E.2 for insight into the correction factor.

For ASTM D638-14 (tension) and ASTM D695-15 (compression) samples, a Zwick Z10 with a 10 KN load cell was used with mechanical wedge grips. A 20 mm Zwick-Roell Clip-on extensometer was used for tensile testing.

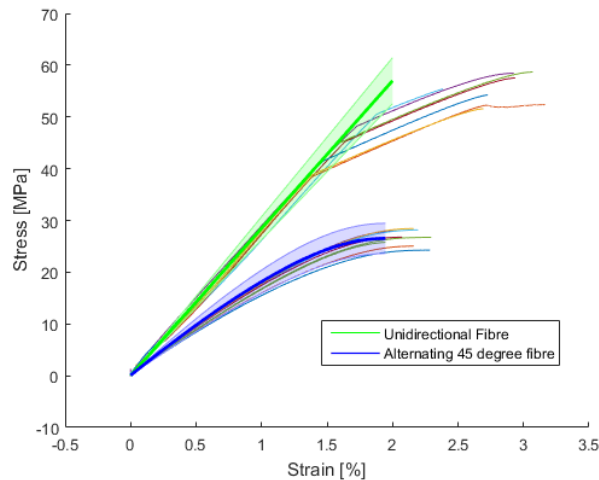


Figure 4.5: Comparison of unidirectional fibre tensile specimen with ± 45 degree infill specimen. Strain gauge removed during test for unidirectional fibre specimen resulting in dramatic slope change.

An identical test was conducted but now considering standard Cura (Ultimaker CAD slicing software) infill settings. This results in an alternating ± 45 degree fibre direction for the fill as well as 1 mm of unidirectional fibres along the sides of the specimen. A comparison between the ± 45 degree infill and unidirectional is seen in Figure 4.5. The ± 45 degree infill did not require removal of the strain gauge as the breaking force was below a given threshold.

The Young's modulus $E = 2700$ MPa is found for the specimen with unidirectional fibres, whereas for ± 45 degree infill $E = 1830$ MPa.

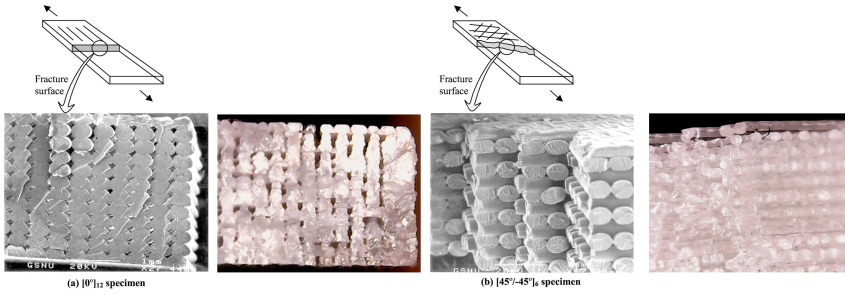


Figure 4.6: (A) Microstructure unidirectional fibres specimen [97] compared with ASTM D638-14 unidirectional fibre specimen. (B) ± 45 degree specimen from Ahn [62] compared with our ASTM D638-14 specimen with ± 45 degree fibres

For FDM PLA, both yield and fracture strain happen at approximately 2% strain. The distinction between the two is important as the manner in which the material fails is highly size dependant. This size effect is analysed and discussed in the following section.

SIZE EFFECT INVESTIGATION

For this anisotropic and porous 3D printed material there may be a size-dependency of the Young's modulus. For this reason tensile samples were manufactured with similar dimensions to the longerons used in the mast. These are 1.5 mm round, 2 mm round, and 2 mm square as seen in Figure 4.4. A 1.5 mm square sample was also attempted but due to a stress concentration located in an air gap in the tapered region of the sample, this data was not reliable.

For dog-bone specimens with 1.5 to 2.5 mm cross sections an Instron 5500R was used with a 1000 N load cell. Here too mechanical grips were used however these clamps were hand tightened. This is combined with an Instron Dynamic Extensometer 12.5 mm GL (12.5 mm)

Figure 4.7a shows the stress strain relationship for the 1.5 mm diameter specimens. These samples exhibit necking and are less brittle than the ASTM 638-14 samples, as expected. This is explained by the decrease in cross-section, as in smaller samples the probability of an imperfection being present decreases. As there are less locations where stress concentrations can occur, the material logically becomes less brittle. For more information see Appendix E.

Analysing the results in Figure 4.7 clarifies that the Young's moduli of all the small-section specimens is similar to the ASTM D638-14 specimens of Figure 4.5, although the latter has approximately 10% lower value than the dog-bone specimens. This can be attributed to extra porosity present in the specimen when compared with the smaller cross sections (see Figure 4.6). However, the small cross-section specimens do not show differences with statistical relevance for the Young's modulus, from which one can conclude that this property can be averaged for all the specimens leading to a mean Young's modulus

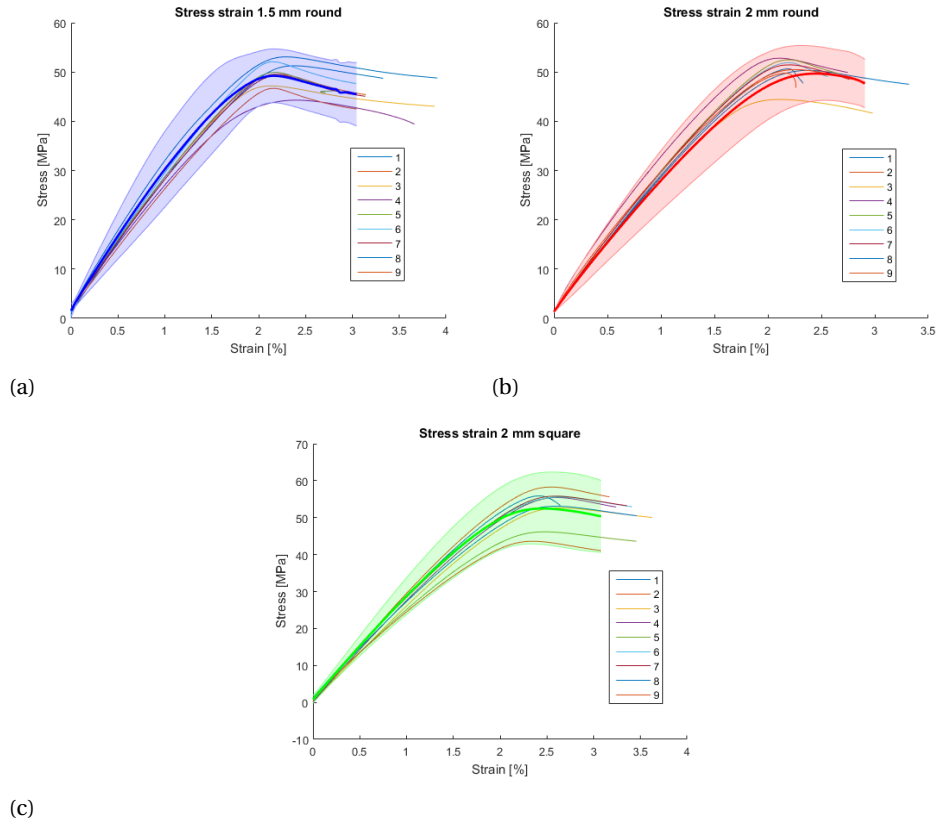


Figure 4.7: Uniaxial tension response of dog-bone specimens with diameters close to that of the longerons. Each legend represents the specimen number. The average curve with 95% confidence bounds is plotted over the raw data.

of 2886 MPa and a standard deviation of 186 MPa (see Table 4.6).

The systematic diameter error and the porosity measured in Section 4.1.2 resulted in an average area difference of 12% with respect to the idealised cross section of bulk PLA. Taking into account the Young's modulus of bulk PLA presented by Torres et al. [94] of 3500 MPa and considering 12% porosity, the rule of mixtures predicts $3500 \times 88\% \approx 3080$ MPa, which is in reasonable agreement with the mean value that was experimentally determined above.

As expected, the Young's modulus varies little with changing the specimen size. What does change is the manner in which it fails i.e. brittle to ductile transition. The data shows that with larger specimens, the failure is far more brittle than for smaller diameter specimens. This is a result of the dimensionality effect. Large specimens are sensitive to imperfections, localising the force around the imperfection. Logically, a smaller sample will have smaller chance of imperfections being present. The smaller specimens therefore exhibit some necking and ductility whereas the large specimens result in brittle fracture.

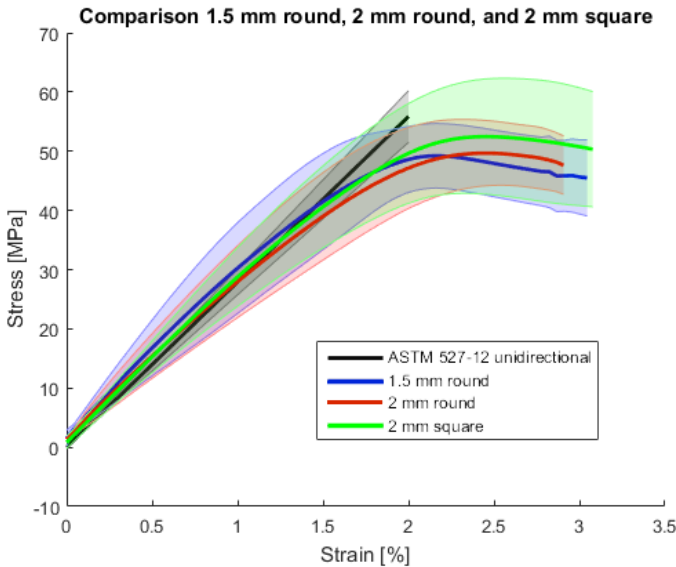


Figure 4.8: Comparison of ASTM D638, 1.5 mm round crosssection, 2 mm round crosssection, and 2 mm square crosssection showing mean and standard deviation on the test data.

Remark 4 *There are many factors which affect the properties of 3D-Printed PLA, such as the printer settings, the temperature, the print speed, the age of the PLA, the print bed alignment. The printer used is also a significant factor as there are minute differences between printers caused by wear and other factors. It is clear from Figure 4.6 that the print quality is not always ideal creating room for error. To counter this, multiple tests are needed to help eliminate variables. For a detailed look into all the factors affecting print*

quality see Appendix B.1. For this reason, keeping test specimens as close to the longeron dimensions as possible helps minimize these differences.

Table 4.3: Average obtained values for tension properties from testing data

Specimen	Young's modulus [MPa]	Yield stress [MPa]	Yield strain [%]
ASTM D638-14 Unidirectional E	2700 ± 112	60	2
1.5 mm round E	2970 ± 200	49	2.1
2 mm round E	2880 ± 150	50	2.2
2 mm square E	2810 ± 210	52	2.3

4.3. UNIAXIAL COMPRESSION TESTS

A known phenomena reported in the literature [102] is that FDM polymers may exhibit different properties in compression and tension, due to the manner in which PLA contains both amorphous and crystalline regions of the polymer chain, as well as the FDM structure. For this reason compressive tests are also investigated herein.

According to the ASTM D695-15 [103] standard, compression test specimens were manufactured with a diameter of 12.7 mm and height of 25.4 mm. An appropriate compressive strain gauge was not available for the Zwick machines, and it was known that the displacement data on these machines is unreliable by comparing the measurements obtained from the strain-gauge (recall Figure 4.5). Therefore, the results obtained for that machine are less accurate and should be considered with caution. As such, another test machine was also used to perform the compression tests on thin specimens (mimicking the longeron cross-section) on a more sensitive testing machine at the department of Precision and Microsystems Engineering.

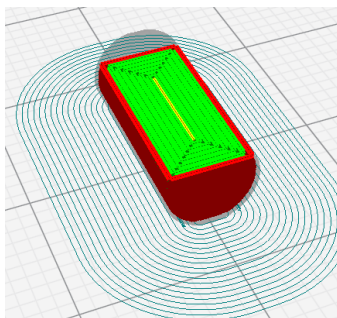


Figure 4.9: Ulimaker Cura, cross section 3D-printed ASTM D638-14 specimen, showing roads generated by printhead movement.

The results of compression testing can be seen in Figure 4.10. A correction factor of 0.68 is applied to these results, based on the measurements for the ASTM D638-14 tensile tests to account for the inaccurate strain measurement of the machine when a strain-gauge is not available. The results are compared to the second experiment conducted

on a 2.5 mm diameter round specimen as seen in Figure 4.10. The elbow seen at 0.8% strain for the 2.5 mm is caused by the settling of the clamping bolts in the material, as well as a misalignment caused by the torsion element of the machine. The test setup can be seen in Figure 4.13. This Zwick machine is optimised for torsion and tension experiments. The torsion cell undergoes self alignment, which allows it to move the clamp with the goal of correcting potential misalignments when the specimen is in tension. However, for the purposes of this test, the self-aligning mechanisms cause a negative effect because the specimen is in compression.

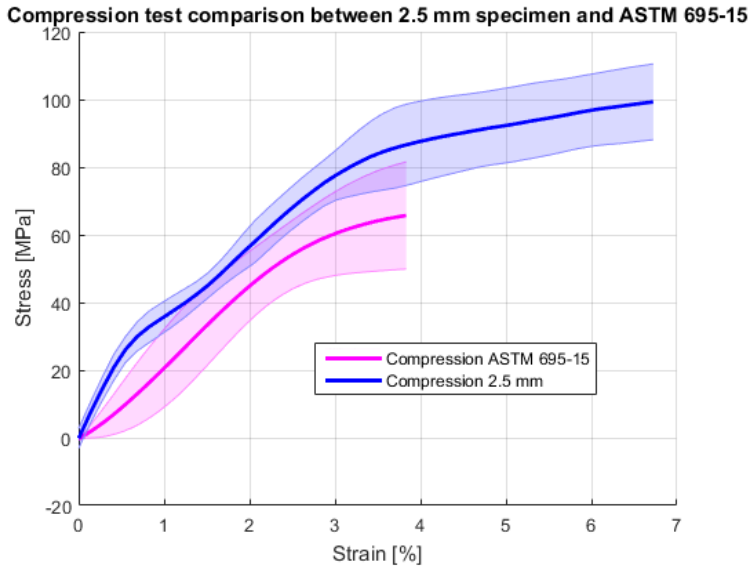


Figure 4.10: Comparison ASTM D695 and 2.5 mm longeron style specimen.

Therefore, both test results have limited interpretability, as verified by the large and unexpected differences observed in Figure 4.10. Measurements reported in the literature for PLA used in FDM mention values for the compression Young's modulus of approximately 1657 MPa for samples with 50% infill fabricated by Jiang et. al. [104], while Song et al. [105] found a value close to 4000 MPa for a sample with a porosity of just 1.5%. Our measurements are inconclusive, as the Young's modulus (below 0.5% strain) correspond to 4367 MPa but the value decreases after 0.8% strain due to the previously referred misalignment of the test apparatus. The corresponding Young's modulus of the ASTM D695-15 is 2300 MPa (measured between 1-2% strain). This measurement zone is chosen to minimize the effect caused by the manner of 3D-printing (see Figure 4.9.)

The compressive strength predictions are also significantly different, although this was to be expected. Table 4.4 shows the measured values. The literature also reports measurements for the compressive strength to be higher than the tensile strength [97, 98]. Ahn et al. [97] find a compressive strength of approximately 40 MPa, whilst Bagsic et al. [98] find a compressive strength of 70 MPa.

In conclusion, the compressive tests are less reliable than the tensile ones due to equipment constraints. However, these results together with other investigations available in the literature indicate that the elastic modulus, and especially the yield stress in compression, are higher than the ones in tension. Yet, given the limited accuracy of these tests, the Young's modulus of the 3D printed PLA used as input for the computational predictions is considered to be given by the tensile measurements, unless the agreement of the simulations indicates otherwise.

Table 4.4: Average obtained values for compression properties from testing data.

Specimen	Young's modulus [MPa]	Yield stress [MPa]	Yield strain [%]
Compression E	$(2000 < E < 4000)$	59	3

4.4. SHEAR TESTING

The shear modulus is used to calculate the Poisson's ratio, which is a parameter used for the simulations. To calculate the shear modulus, a torsion test is performed on a round cross section specimen with a diameter of 2.5 mm.

A custom built Zwick shown in Figure 4.13 having both tensile and rotational capabilities was used to conduct multi-loading tests, as well as the pure shear tests. A 1000 N tensile load cell was fitted as well as a 0.5 Nm torque cell. No extension or torsion meters were available for use with this machine.

The average shear modulus is found to be 954 MPa with a standard deviation of 84 MPa. The shear modulus is based on the average of 41 torsion tests performed on 8 specimens. Performing multiple tests on a single specimen helps minimise the effect of slipping caused by the mounting apparatus. This is marginally lower than 1287 MPa of bulk PLA that is quoted by Torres. The findings from Torres and Balderrama-Armendariz [94, 106] show that the FDM process should not significantly affect the material properties including shear modulus, and yielding points. Although the average shear modulus is marginally lower, the average yield stress is significantly lower. The shear yield stress is found to be on average 24.43 MPa (See Figure 4.11). Compare this to the results found by Torres et. al [94], who find the shear yield stress within the bounds of $32 < \tau_s < 52$ MPa for specimens with 100% infill.

The lower shear modulus can be accounted for by the presence of porosity and poor packing factor obtained at this scale. However Torres et al. [94] also demonstrate that shear properties of FDM are far more sensitive to cross section shape than tensile properties. We also find this sensitivity as evidenced by the large range found for the shear modulus. We conduct a deeper investigation into the cross section of the specimens used, see Appendix E.5. The results are staggering, showing a large variation in both porosity and shape for prints conducted on the same printer at the same moment with the higher shear values corresponding to rounder specimens.

These findings lead to the conclusion that all longerons have an imperfect cross section shape at some point along their length. Torsion specimens are far more sensitive to this

than tension specimens as the polar moment of inertia (mm^4) is a vital parameter. The likelihood of there being an imperfection present in the specimen increases with specimen length. These differences with respect to the ideal specimen cause undesired stress concentrations in torsion, thus yielding at a lower stress. Initial torsion tests were conducted using a 60 mm length between grips, and some yielded plastically at around 1 % strain (see Appendix E.5). To help reduce this, the specimen length is reduced from 50 mm to 20 mm between grips. Figure 4.11 shows the result of the 20 mm test. For near-perfect geometries (specimen 1 & 3) the shear limit is closer to the expected value.

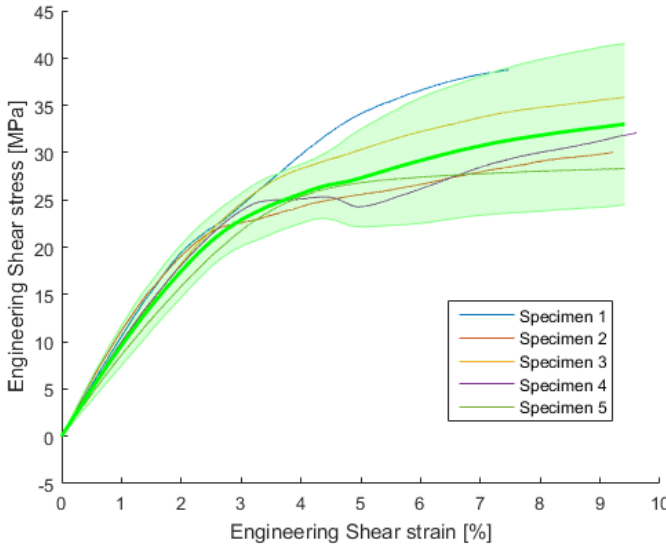


Figure 4.11: Stress strain curves of shear test only initial loading paths shown.

Table 4.5: Average obtained values for torsion properties from testing data.

Specimen	Young's modulus [MPa]	Yield stress [MPa]	Yield strain [%]
Torsion G	(954 ± 84)	24	2.8

4.5. YIELD SURFACE LONGERON

Determining the complete yield surface of a material requires multiple tests under multiple combinations of stress states. Establishing the yield surface has been attempted in other contexts by multiple authors [107–111] that proposed different methodologies.

In this research, torsion-compression and torsion-tension tests were performed to track the yield behavior under these loading conditions. As the Zwick from PME department is a prototype, loading in both tension/compression and torsion simultaneously was not possible. This meant a two stage process had to be conducted. A second issue with the Zwick was that load control in both tension and either torsion or compression would

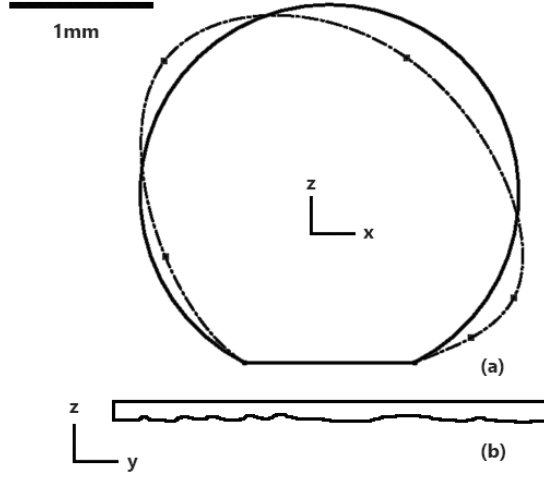


Figure 4.12: (a) Indication of possible differences in cross section shape of torsion specimen. (b) The attachment to support material on the print bed produced a rough surface with indentations causing localised stress concentrations.

cause the software to crash. This meant the only viable option was to perform the tests in displacement control for tension/compression, and then applying a torsional load until plasticity occurred. This would enable tracing the yield surface.

An attempt was made with this test methodology. A 2.5 mm diameter round longeron specimen was placed in clamps containing a 3 mm hole and held in place by an M3 bolt at both ends, see Figure 4.13. The plan was to conduct an initial tension/compression displacement control at various percentages of the known elastic limit, after which applying torsion until yielding. Secondly, by switching the order and holding a known torsion angle, and conducting a tension/compression load until yielding avoids bias. Unfortunately, these tests did not produce reliable data as too much scatter was observed to draw relevant conclusions. The results of these tests with all data points are reported in the Appendix (Figure E.12).

An alternative is provided by the literature using analytical representations of the yield surface of similar polymer types. Bessa et al. [7] proposes an analytical model based on the Raghava parameter [114] using the yield point of compression and tension to construct the yield surface based on the work by Melro et al. [112]. Equation 4.2 is created by sampling the yield stress of an epoxy (EPON865/33DDS) at different stress states in the principal stress space ($\sigma_1 - \sigma_2$). The samples points are approximated by the paraboloidal yield criterion [7]. Here σ_{Y_c} and σ_{Y_t} are the values of compressive and tensile yield stress. $I_1 = TR(\sigma_{ij})$ is the first stress invariant and $J_2 = \frac{1}{2}s_{ij}s_{ij}$ is the second invariant of deviatoric stress tensor s_{ij} . For further information the reader is directed to the following literature [7, 112, 113].

As a combination test of torsion with tension/compression was not possible, limited conclusions can be made about the yield surface of FDM PLA. Using the values for tension, compression and torsion (of round specimens), a good fit for this analytical model was obtained. As we cannot conclude with any certainty this model is correct, it will not be incorporated in the simulations, however it may offer explanations to the accuracy of the plasticity threshold in the design classification (see Figure 5.3).

$$\sigma_{Y_s} = \sqrt{\frac{\sigma_{Y_c} * \sigma_{Y_t}}{3}} \quad (4.1)$$

$$f(\sigma, \sigma_{Y_c}, \sigma_{Y_t}) = 6J_2 + 2(\sigma_{Y_c} - \sigma_{Y_t})I_1 - 2\sigma_{Y_c}\sigma_{Y_t} \quad (4.2)$$

$$J_2 = \frac{1}{3}I_1^2 - I_2 \quad (4.3)$$

where: I_1 and I_2 are the stress invariants and σ_{Y_t} and σ_{Y_c} the yield stresses of tension and compression respectively.



Figure 4.13: Test setup tension/torsion bench at department of Presesion and Microsystems TUDelft.

4.6. SUMMARY

The material which is being used for the longerons in the 3D printed mast has a porous composite like mesostructure. The elastic properties of the longerons can be found in table 4.6. The average cross section diameter and its standard deviation can be found in Appendix C.3 with the resultant diameter for a 1.5 mm designed mast being 1.48 mm with a standard deviation of 0.06 mm. This is due to the inaccuracies of the Ultimaker 2 and the support material, resulting in a rough surface quality.

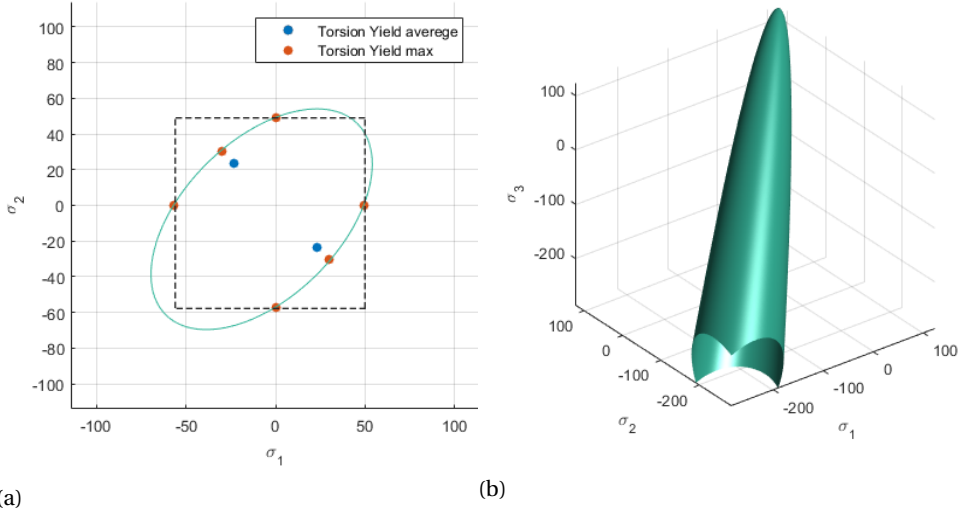


Figure 4.14: Yield surface model proposed by Raghava [114]. When using the shear yield stress obtained from torsion tests of specimens whose cross-section was close to the idealized cross-section, the model fits the data well. Note that "torsion yield max" refers to the average of specimen 1 and 3 in Figure 4.11, i.e. the specimens with close to ideal cross-sections. Dotted lines represent the yield criteria used in the simulations corresponding to 2% yield strain in tension and 3% yield strain in compression.

Figure 4.15 shows the different moduli, as well as the yield points for each. Using these yield points one can try to construct a yield surface for the material. There was an attempt to construct the yield surface of the 3D printed PLA, but due to experimental equipment limitations no conclusive data was obtained. However, the yield stress and the strength of the material under compressive loading are higher than those in tension. Importantly, the tensile, compressive, and shear tests allowed for a clear conclusion to be established: the maximum strain yield criterion of $\max(\epsilon_{ij} \approx 2\%)$ provides a conservative estimation for the onset of plasticity, as none of the tests led to yielding beyond this value. This conservative value is determined from the behaviour in tension, as it is shown to be the most critical one.

Figure 4.15 shows the three primary material property test results for the longeron. As discussed before, the compressive modulus result is less accurate, but when combined with studies found in the literature can be used to conclude the compressive strength is higher than the tensile one. Table 4.6 shows an overview of the measured Young's and shear moduli with corresponding standard deviations of the data. It is clear that the Ultimaker quoted properties (3.3% stain) are not applicable to our longerons. Now with a good understanding of the longeron material properties we can find a more accurate material classification as seen in Figure 5.1

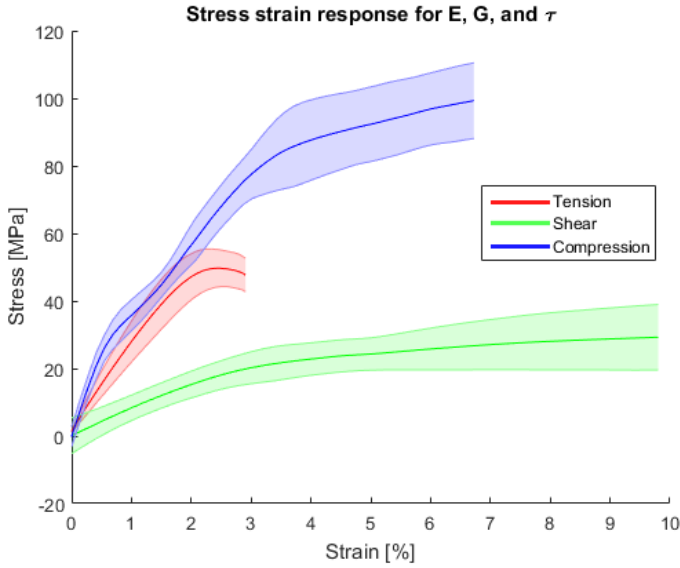


Figure 4.15: Overview of Tension, compression, and Shear test on 2.5 mm diameter round specimen.

Table 4.6: Results obtained through material testing on sampled of 3d-Printed PLA which will be used in the simulations

Input	Symbol	Mean	Standard deviation
Diameter	d	1.48 [mm]	0.06 [mm]
Young's modulus	E	2886 [MPa]	186 [MPa]
Shear modulus	G	954 [MPa]	84 MPa
Mode-1 error	-	4 [deg]	1.2 [deg]

The cross section measurement was conducted on longerons of 1.5 mm. The material properties and porosity values are assumed applicable to all longerons printed between 1 and 3 mm diameter. The Young's modulus is obtained as the average of the 3 dog-bone tests, (1.5 mm round, 2 mm round, and 2 mm square). Shear modulus is obtained from the average of all tensile tests (50 tests in total) using 2.5 mm specimens. Mode-1 error is determined by measurement of 5 masts with parameters $D_1 = 90$, $D_2 = 72$, $p = 60$, $d = 1.5$, $n = 10$ using PLA support rings

Furthermore a conclusion can be made about use of FDM printed PLA in functional components. Interest from literature is slowly identifying the limitations of FDM technology, mostly investigating the affects of varying print settings and curing temperatures. From found results, the repeatability and consistency of print quality is the biggest shortcoming of hobbyist FDM printers. It appears that tensile loading is not greatly af-

affected by small variation in cross section shape. Torsion properties, are however greatly affected by the shape and so extreme caution should be used when loading FDM parts in torsion.

5

EXPERIMENTAL VALIDATION OF DATA-DRIVEN DESIGN

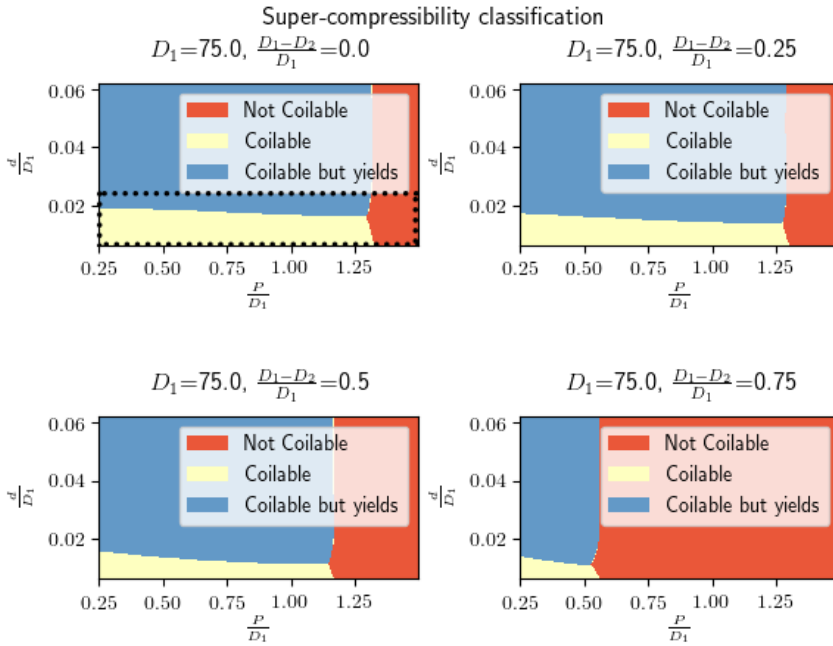


Figure 5.1: Classification chart using maximum yield strain criterion of 2%.

THE results of characterizing the 3D-printed PLA are implemented into the material plots which improve the predictions. Figures 5.1 and 5.2 are generated using these

improved values for the longerons and show the limits of geometry of the half-mast and the influence of given parameters on the compressive strength. This chapter will investigate how accurate these predictions are for a PLA half-mast. First the accuracy of stress strain response will be determined for a given half-mast. After-which several half-masts containing different geometries will be analysed in order to test the validity of assumptions made (constant Mode-1 error and negligible hinge friction) for the simulations.

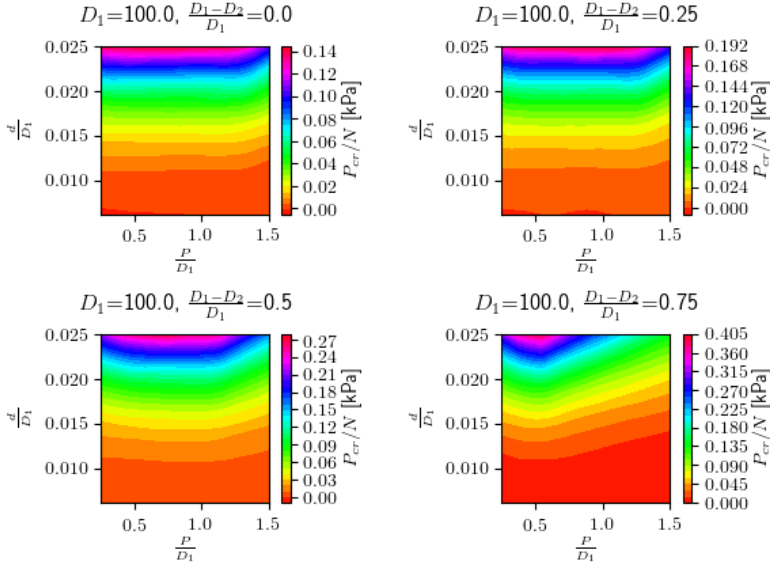


Figure 5.2: Mean quantities of interest d/D_1 , P/D_1 , D_r . Showing continuous plots over the dotted zone Figure 5.1, stress is shown per longeron.

5.1. FIRST 3D PRINTED PROTOTYPES

When selecting a viable 3D printer, we first needed to validate whether the Ultimaker 2 was capable of printing this structure. Arbitrary mast dimensions were chosen, $D_1 = 75$, $D_2 = 42$, $P = 65$, using 2 mm longerons. This mast appears as Point 1 in Figure 5.3.

Remark 5 *This first half-mast (point 1) was printed before the machine learning predictions were available to guide the design. This print was conducted to determine whether or not the components could be 3D printed using FDM and PLA.*

This first prototype (Point 1 in Figure 5.3), although functional, required an excessive amount of manual labour because it consisted of 15 separately printed components. Therefore, a new print scheme was devised to circumvent this issue. Instead of printing everything separately, an attempt was made to have only two separate prints for the

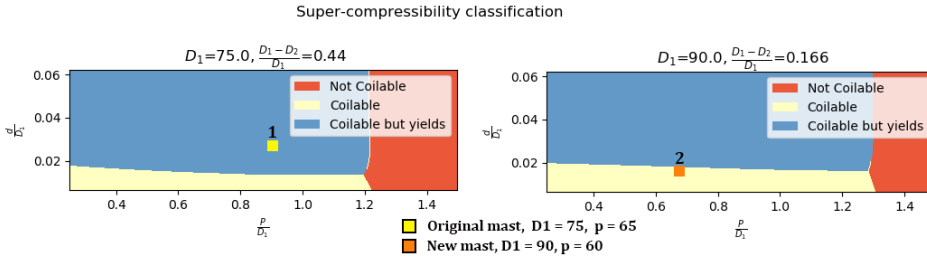


Figure 5.3: Design classification shown for original prototype half-mast and first manufactured half-mast which falls inside the design window.

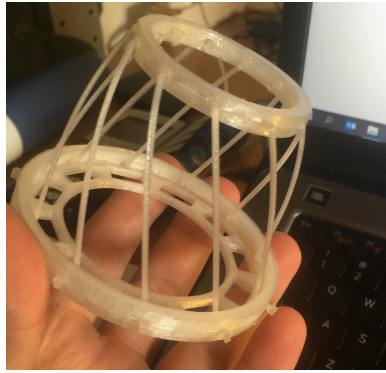


Figure 5.4: Prototype mast.

complete assembly of the half-mast: one part resembles a "spiderweb" and consists of the upper ring with the longerons, and a second print with a support ring. This new design was functional but had other significant limitations when applied to this problem and was discarded. For a full overview of the design see Appendix D.

5.2. FIRST HALF-MAST DESIGN

Regarding the classification and regression results, one clearly observes that there is negligible influence from the pitch of the half-mast on its critical buckling load (see Figure 5.2). Note that the quantities of interest are also determined per number of longerons and that if the size of the top ring decreases, then the number of longerons that can be attached to it also decreases. Therefore, the only incentive for the longerons not to be vertical, i.e. $(D_1 - D_2)/D_1 = 0$, is to create space in order to avoid self-contact between them when the half-mast is fully compressed as illustrated in Figure 5.5.

A low value of $(D_1 - D_2)/D_1 = 0.166$ was considered for validating the data-driven framework, and through finite element simulations it was determined that 11 longerons could

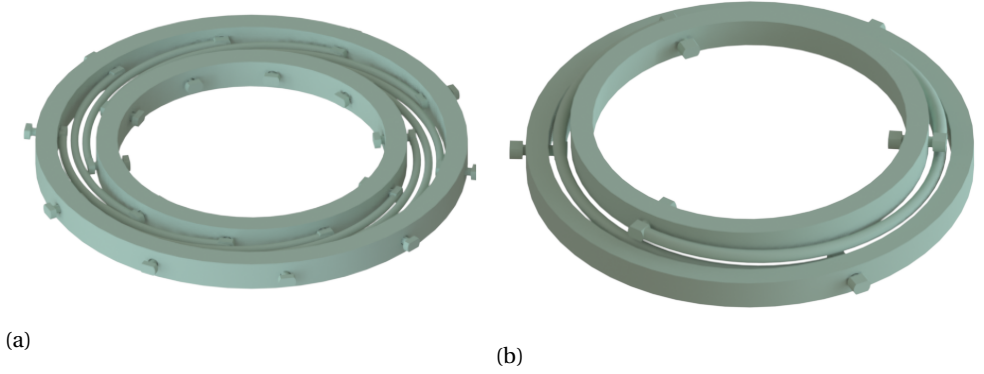


Figure 5.5: Difference in maximum compressive strain illustrated between sloped longerons (a) and vertical longerons(b).

be accommodated without self-contact. The half-mast parameters are: $D_1 = 90$, $D_2 = 72$, $P = 60$, $d = 1.5$ and using 11 longerons (Point 2 in Figure 5.3). $D_1 = 90$ is chosen as it is the maximum diameter with which 4 rings can fit on one printbed of the Ultimaker 2, limiting the number of prints which are necessary. A longeron diameter of 1.5 mm is selected as the maximum achievable longeron diameter which does not result in plastic deformation.

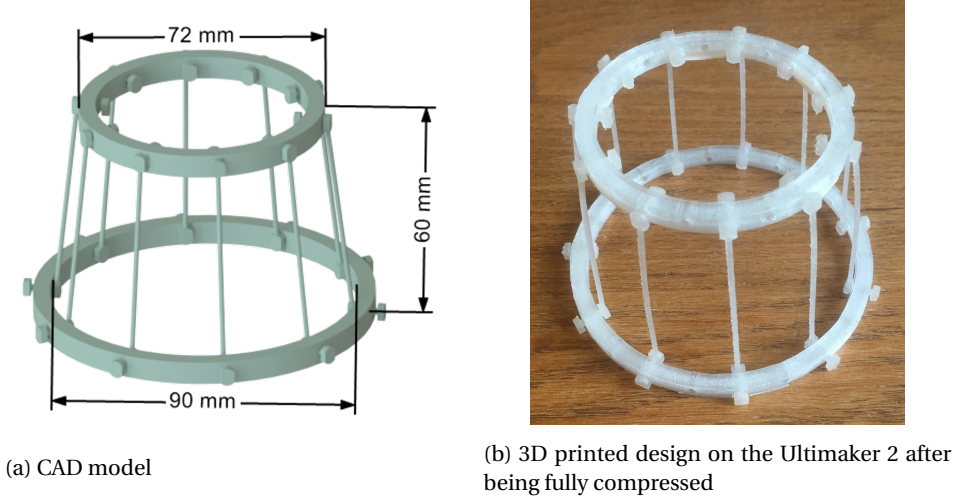


Figure 5.6: Half-mast design corresponding to Point 2 in Figure 5.3.

Figure 5.6b shows the proposed mast post-buckling. The results seen in Figure 5.7b show that the predictions do not correspond to the experimental test data. Consulting Kitamura's analytical formula [45] shown in pink, we see that it corresponds with the ML

predictions and not the test data. The ML prediction bounds are obtained by running 30 FE simulations using parameters randomly selected from the input bounds (Table 4.6). Each parameter is selected from a Gaussian distribution. The resultant plots show the mean of all simulated masts, with bounds showing an uncertainty of 2 standard deviations.

It is hypothesized that the difference between the test data and ML predictions lies in the friction at the hinges. This is further validated when looking at microscopic images (see Appendix C.2) of the aforementioned hinges. A large spread of the test data is observed (in the order of 12.5%) showing that the friction caused by the hinges is not constant for all masts.

The cause of this variable friction is due in part to the manual assembly of the half-masts. Each support ring is constructed out of two half rings glued together. While most of the pin hole connections are considered near-perfect, a percentage of the holes are slightly misaligned causing increased friction. This misalignment is shown in Appendix C.2.

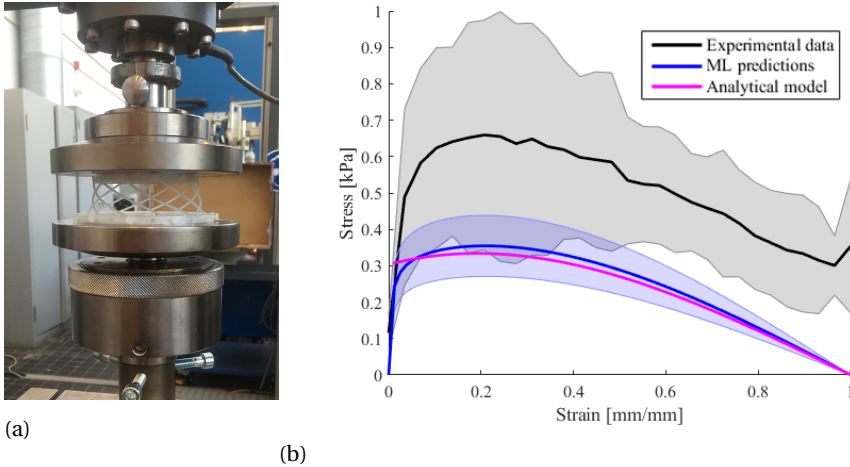


Figure 5.7: (a) Test setup for compression testing of the mast on Zwick z10, (b) Stress strain response compression test showing 2 standard deviations compared with Kitamura [45] analytical model and ML predictions with 2 standard deviations.

5.3. SECOND MAST ITERATION

For the second iteration of the mast, many of the problems encountered in the first mast design are addressed:

- The Polymer rings causing high friction are replaced with milled aluminium rings, which have a negligibly low friction coefficient with PLA. (Shaw et al. [115] find a friction coefficient between Aluminium and PTFE a similar thermoplastic polymer to be in the order of 0.05 to 0.23). The reason for changing the support rings

rather than adding friction into the simulations is due to the variability of the friction in identical masts. Both lowering the friction coefficient in the hinges and more importantly making it constant for all longerons increases the repeatability of tests.

- According to the simulations 11 longerons fit in the fully compressed state with no self-contact. However, tests revealed that the support material around the hinges causes contact between longerons after 95% compression (see Figure 5.7b). Removing support around the hinges would cause a stress concentration which is undesirable. Instead the number of longerons will be reduced to 10.

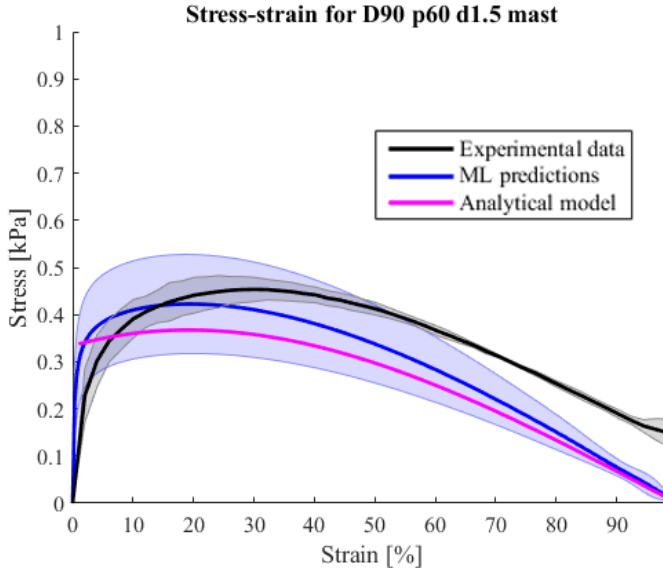


Figure 5.8: Response of low-friction mast design corresponding to Point 2 in Figure 5.3. Low friction is achieved by using aluminium rings. The 95% confidence bounds for experimental results and FEM simulations are also included (mean response is the solid line).

Figure 5.8 shows the test results of the half-mast using aluminum rings. These experiments are significantly closer to the finite element predictions than the ones obtained using the polymer rings, showing that friction in the hinges was indeed the cause of the discrepancy. However, note that the initial linear zone is less steep, and the peak stress is located around 26% strain rather than 18% for the ML predictions. Furthermore we see that even in a fully compressed state, residual stress remains. This phenomenon can be explained by the longerons plastically deforming during compression, as supported when looking at repeatedly loaded half-masts shown in Figure 5.9, and possibly due to some aluminum-PLA friction.

If we assume the yield surface model presented in Figure 4.14a is representative of the FDM material. This may help to explain why there is an onset of plasticity below the

given bounds of the metamaterial classification. Currently the simulations use tensile strain limit as the threshold for plasticity (Square dotted region in Figure 4.14a). It can be observed, using combined loading and assuming the paraboloid criteria, that the material may yield at a lower stress and therefore also a lower strain. This helps to explain why the $p=60$ (Mast 2 in Figures 5.3) longerons yield while not classified as such.

The fact that plastic deformation is present in this mast leads us to conclude that the classification bounds of 2% strain may not be conservative enough. In future, the yield surface will need to be included in the simulations to further improve the classification.

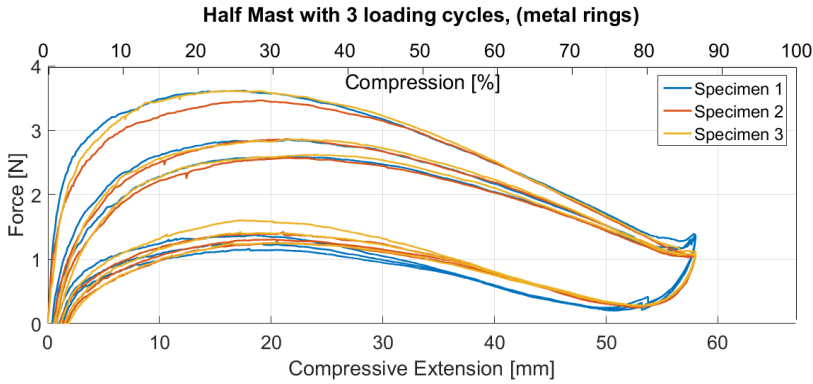


Figure 5.9: Three consecutive repeated loads for $P = 60$ mm and $D_1 = 90$ mm mast with aluminum support rings.

5.4. THIRD MAST ITERATION

Using the same aluminum rings, a third iteration of the design is created:

- The pitch (P) is increased to 90 mm with the goal of maximising compressive strain (approximately 94.7%) while still being sufficiently far from non-coilable region.
- The longeron diameter (d) is lowered to 1 mm to reduce the chance of plastic deformation occurring at the cost of peak stress.

This new mast is shown as point 3 on figure 5.10.

The new dimensions of the half-mast are as follows, $D_1 = 90\text{mm}$, $D_2 = 72\text{mm}$, $d = 1\text{mm}$, $P = 90\text{mm}$ with 10 longerons see Figure 5.10.

What can be seen from Figure 5.12b is that the ML predictions now accurately predict the half-mast response. The ML simulations used a measured average angle of 7 degrees for the Mode-1 error and a Young's modulus of 2886 MPa. The longeron diameter has a measured mean diameter of 1.007 mm with a standard deviation of 0.05 mm. The Poisson ratio, due to inaccuracies in both the E and G, has a mean of 0.43 and a S_d of 0.06. For this analysis, 30 unit cells are simulated across the range of imperfections mentioned

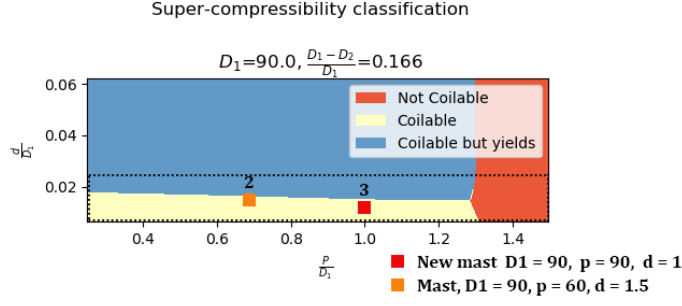


Figure 5.10: Design classification metamaterial unit cell.

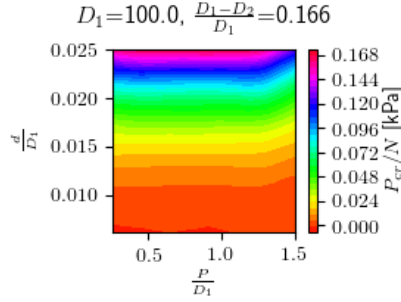


Figure 5.11: Influence of parameters on critical buckling force for zone shown with dotted line in Figure 5.10.

above. The mean and 2 standard deviations of the simulated half-mast responses are shown in blue as seen in Figure 5.12b.

Analysing the plot we see that in practice, there is an increase in stress at 95% strain. This is caused again by the interaction of the longerons which are now 30 mm longer than the previous half-mast ($P = 90$ instead of $P = 60$). This interaction can be beneficial, causing the half-mast to spring back on its own accord. Without this, the half-mast would achieve a new equilibrium state, also known as bistable (see Section 2.1.4). This is a further design choice which can be taken into consideration when designing for a specific problem.

Furthermore, it is observed that the ML prediction achieved a marginally lower peak stress, and a steeper curve. Friction in the hinges, which is not included in the simulations, can account for this difference. We can conclude that the ML predictions are able to predict the mast response with sufficient accuracy, despite the large amount of uncertainty of the parameters. A visualisation of a single compression can be seen in Figure 5.13.

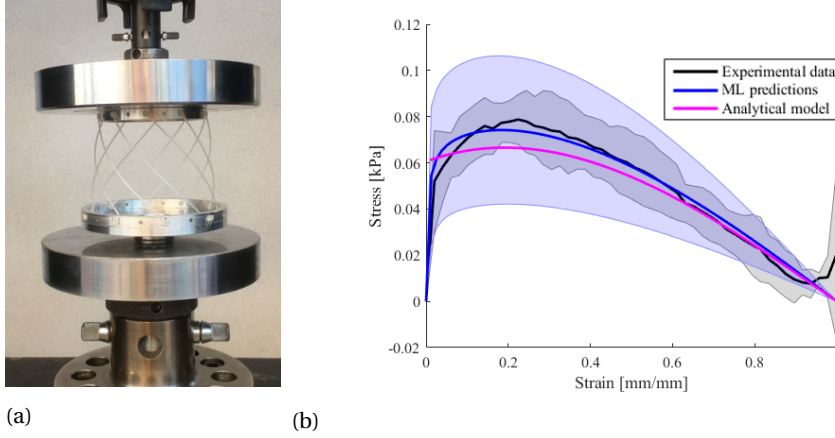


Figure 5.12: (a) test setup for compression testing of the half-mast on Instron fitted with 100 N load cell with ball bearing, (b) Stress strain response comparison between: experimental data, machine learning predictive model, and Analytical model [45] for a $D_1 = 90$, $P = 60$, $D = 1.5$ mm diameter unit cell with 10 longerons.

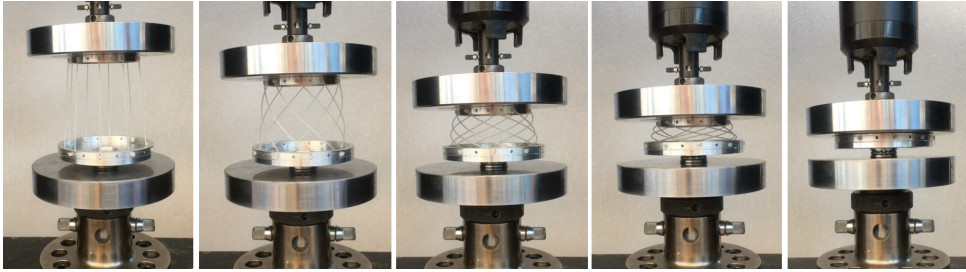


Figure 5.13: Compression cycle for $P = 90$ mm half-mast (Point 3 on classification in Figure 5.10).

5.5. ML CLASSIFICATION VALIDATION

In the previous section it was shown that the data driven framework can accurately predict response behaviour of a single half-mast design. The ML classification now needs to be tested for unit cell geometries across the design space. In order to validate both the classification and the accuracy of ML predictions over the design space, six designs are considered as shown in green in Figure 5.14. All unit cell geometries use the same polymer for longerons, same D_1 and D_2 , and same testing setup consisting of the aluminum rings. The longeron thickness and pitch, however, is varied. The ball bearing is replaced with a 3D printed PLA cone allowing one support ring to rotate freely across all 3 axis, which closer resembles the restrictions in Abaqus simulations. The simulations also allow freedom of movement of one ring in the x-y plane. This freedom of movement is too complicated to incorporate into the practical experiments. Not incorporating this

freedom may affect the results of the non-coilable region.

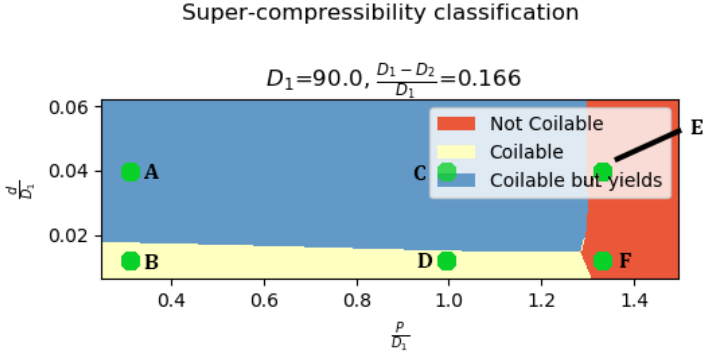


Figure 5.14: Unit cell geometry combinations tested in order to validate the machine learning classification.

Figures 5.15 and 5.16 shows the results of testing half-masts A-F of the design space. Figure 5.15 shows images taken during compression whilst Figure 5.16 shows the stress strain response of a tested half-mast as compared with the ML response data. The following data corresponds to each half-mast response:

- A Due to the bending stiffness of the short longerons, this half-mast did not function as intended. The longeron diameter was 0.5 mm wider than that of the hinges resulting in deformations of the hinges rather than the longeron. Furthermore the test was aborted pre-failure due to reaching the threshold of the load cell. On a subsequent test, it is observed that several longerons broke at the hinges as seen in Figure 5.15. This test was not representative of the half-mast which was being simulated and thus can be disregarded.
- B This half-mast is located in the coilable region of the classification. This unit cell does not plastically deform (see Figure 5.17a) and has a significantly lower $\frac{p}{D_1}$ with respect to the Metamaterial D. An underestimation of the stress by the ML predictions is observed, and friction is again the most plausible explanation because as the angle of the longerons increases ($\frac{D_1-D_2}{D_1}$ increases) then there is higher friction since the longerons are forced against the support rings.
- C This half-mast clearly shows the impact of longeron interaction which needs to be considered. The simulations do not account for this and so after 65% compression the model is no longer representative. It is also observed that a significant amount of plastic deformation occurs causing one longeron to snap in its fully compressed state. Figure 5.15 shows that it no longer recovers to its original length.
- D Metamaterial D in Figure 5.14 is identical to Point 3 in Figure 5.10 used in the previous section which has already been fully investigated.

- E This tall half-mast is classified as non-coilable, however, the half-mast does appear to coil. Looking into the buckling mode (Figures 5.18) we see that the mast is indeed simulated as coilable. The material classification uses a very simple classifier Support Vector Machine. This classifier draws a line of best fit between data points attempting to achieve the smallest possible error. This means that the nearer the bounds the half-mast parameters are, the more uncertainty there is regarding the classification. We see from Figures 5.18 that the difference in Eigen values is small. Selecting half-mast parameter P/D_1 as 1.4, results in buckling mode-2 being dominant as validated in Figure 5.19. This is a difference in pitch of just 6 mm showing just how close to the threshold it is. Furthermore, after 30% strain it can be noticed that the longerons are bent out of plane. This leads to a smaller bending radius and thus an increasing stress on the longeron. This causes the longerons to break at this small bending radius, starting at 46 % strain.
- F This half-mast behaves in a similar manner to half-mast E. Indeed the buckling Mode-1 also just dominates meaning that although not predicted as such, the mast coils. Similar to half-mast E, F also coils out of plane however the longeron diameter is small and so no fracture occurs. Frictional differences between hinges cause the base plate to both rotate and coil. The extra rotation of one end of the half-mast may contribute higher stresses towards the end of the compression.

It is clear from the above analysis that friction located in the hinges plays a significant role in the half-mast response. The influence of friction is directly related to the load which the mast is experiencing, resulting in the ML predictions underestimating the compressive strength of half-masts with higher loads. It can also be concluded that the Mode-1 error implemented into the simulations is not constant for all half-mast parameters. The Mode-1 error (mean = 4 degrees) is based on a half-mast with longeron diameter of 1.5 and a pitch of 60. The Mode-1 angle of the $P = 90$ mast with 1 mm diameter longerons has a mean of 7 degrees. This shows us that the Mode-1 error needs to be implemented into the simulations as a function of pitch and diameter.

Remark 6 *Two half-masts were tested for each point of the material classification, however for half of the tests, no appropriate load cell was available. For this reason there is only one response curve shown for each half-mast. As mentioned before, in practice there is a degree of variance between the properties of identical FDM printed longerons. This variance is included in the bounds of the ML prediction. As several half-masts fall outside the bounds, most notably half-mast B, it can be concluded that the assumption of friction in the hinges being negligibly small is incorrect.*

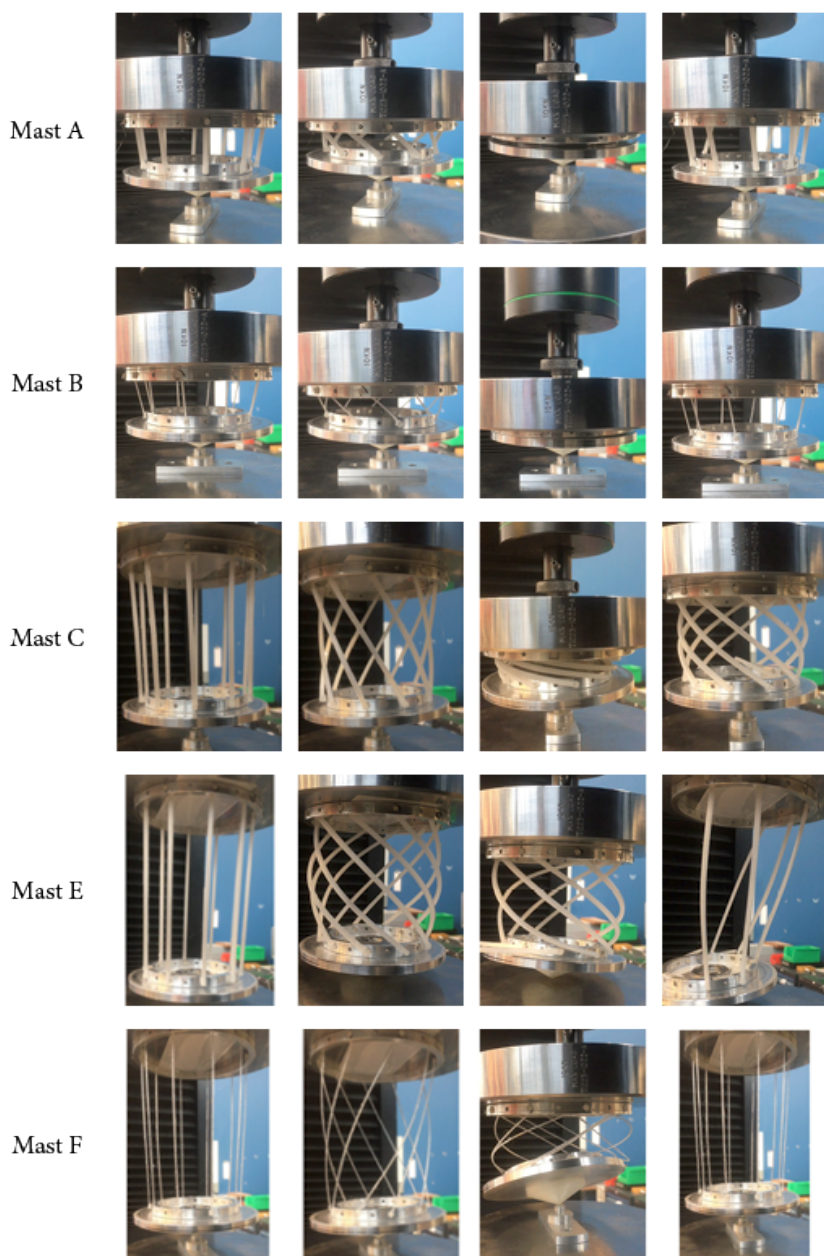


Figure 5.15: Images taken during various stages of compression starting and ending in the fully extended state.

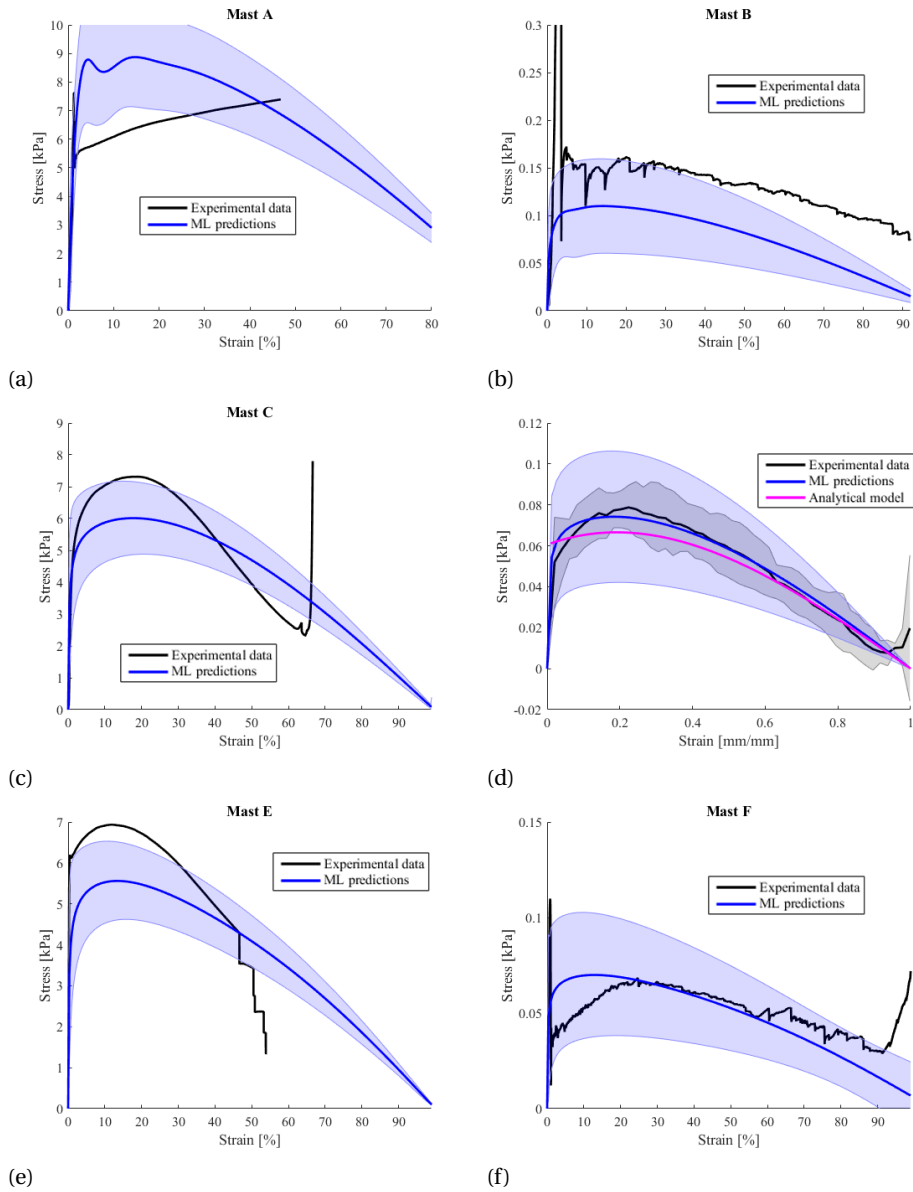


Figure 5.16: Stress strain response data for mast designs defined in classification. Finding robustness of ML prediction by comparing it to test data.

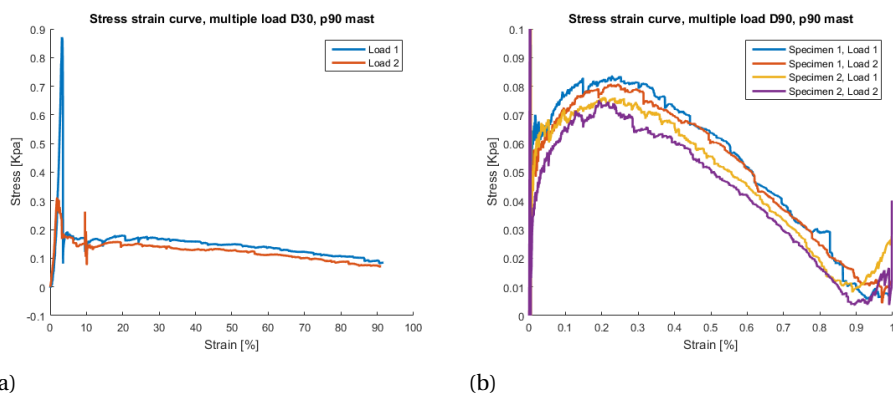


Figure 5.17: (a) Stress strain response for a half-mast with $D_1 = 90$ and $P = 30$ using 10 longerons of 1 mm diameter, (b) A stress strain response for a half-mast with $D_1 = 90$ and $P = 90$ using 10 longerons of 1 mm diameter

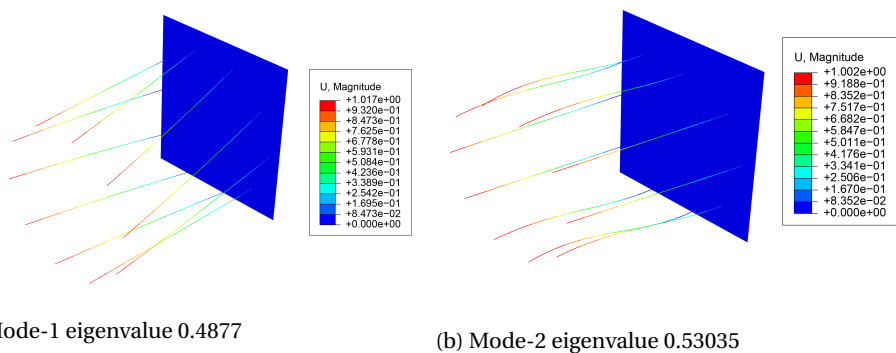


Figure 5.18: Buckling Modes for half-mast $D_1 = 90, D_2 = 72, P = 120, d = 3$

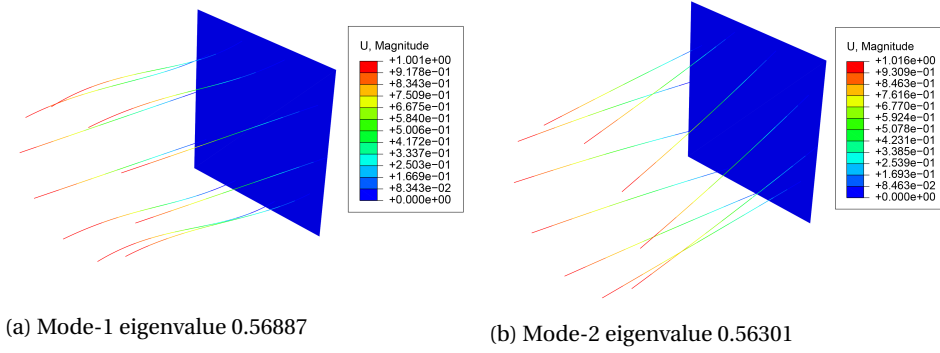


Figure 5.19: Buckling Modes for half-mast $D_1 = 90, D_2 = 72, P = 120, d = 3$, with only a marginal difference

It can be concluded that the ML predictions are able to predict half-mast behaviour with varying degrees of accuracy. Furthermore, it is clear that the assumption of negligibly low friction in the hinges does not hold up for all half-mast unit cell parameters. Lastly the assumption that all error modes can be incorporated into a single Mode-1 error and that the same lognormal distribution holds for all half-masts is proven false. It is clear that both pitch and longeron diameter greatly influence the amount of Mode-1 error present and so the measured mean of 4 degrees of the $P = 60$ half-mast does not apply to all half-masts.

By using the machine learning to fully understand the relationships of the parameters and half-mast responses, makes conclusions about certain observed effects easier to obtain. It is clear that the longeron thickness makes a significant impact on the compressive strength of the mast. It is also clear that parameter d is severely limited by the strain limit of PLA. We can thus conclude that the best way to increase the compressive strength based on the test data is to change the material to a material which has a higher strain limit with comparable Young's modulus.

5.6. COMPARISON WITH STATE OF THE ART

Looking at Figure 5.20, we see a comparison of three versions of the half-mast with the metamaterials found in the literature. The densification strain axis shows the comparison of the maximum achievable strains. It is important to note that densification strain can allow for plastic yielding of the material (see Figure E.1). The metamaterials plotted, all achieve the aforementioned strains in the elastic region. Furthermore, we find that when compared with the state of the art, the current metamaterial design made from PLA with 1 mm diameter longerons falls far short in compressive strength. A high compressive strain of 94% is achieved, far surpassing that of the carbon nanotube film presented by Cao et al. [44].

A theoretical limit for this structure is found in terms of compressive strength. This limit

is calculated assuming an I-beam profile for the longerons and that the base materials are carbon nano-tubes [89]. We highlight that this is not a realistic design, but this illustrates that high compressive strengths can be obtained with stiff base materials and different longeron cross-sections.

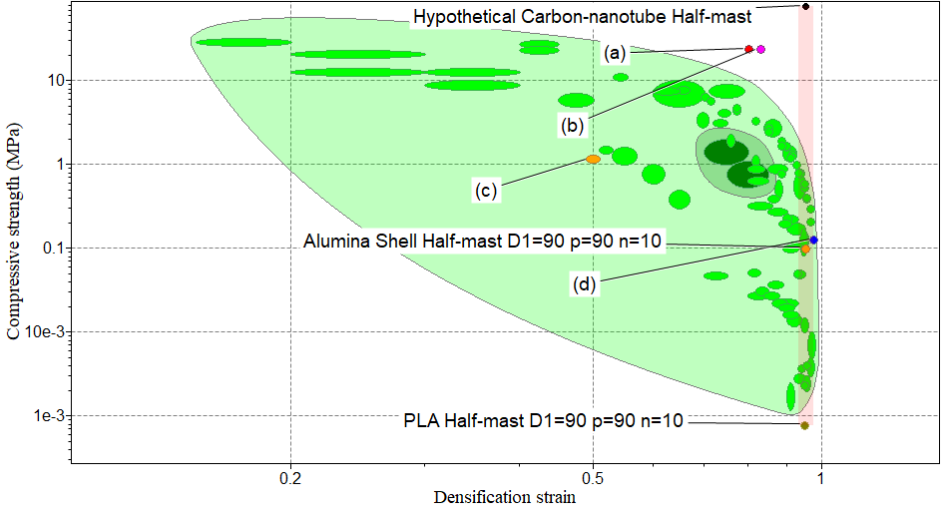


Figure 5.20: Asby plot comparing compressive strength to densification strain comparing the researched half-mast to the state of the art. The range (shown in red) of achievable strains is shown for $P=90$ PLA unit cell to hypothetical carbon nanotube unit cell encompassing a half-mast made using alumina pipes for the longerons. The half-mast is made using the same ratios for pipe diameter to wall thickness (≈ 0.017 which is in the thin wall range $t/a \ll 0.02$) Meza et al. metamaterials [116]. With (a) PAPMS [42], (b) Cao et al. [44], (c) 3D-printed graphene aerogel microlattice [17], and (d) Grapehe aerogel [43]

Meza et al. [116] presents a comparison of metamaterial structures fabricated by two-photon nanolithography (Nanoscribe) and coated with alumina. Printing with the Nanoscribe allows more complex geometries, so a direct comparison can be established with the designs by Meza et al. [116]. We assumed the cross-section of the longerons of a mast with $D_1 = 90$ mm, $P = 90$ mm and $d = 1$ mm is now a pipe profile (due to the coating with alumina), using an identical thickness to radius ratio as that presented by Meza. Furthermore, the pipe diameter (3 mm) was chosen such that it would experience no more than 4% strain during compression, where this value is determined in the original work as the maximum achievable strain for the alumina shell. Without any optimization we see that our half-mast falls into the compressive strength of ductile metamaterials (see Figure 5.21). The nano-lattices presented by Meza have a compressive strain limit of 70%, while the proposed metamaterial far surpasses this value (94.7%) and is fully recoverable.

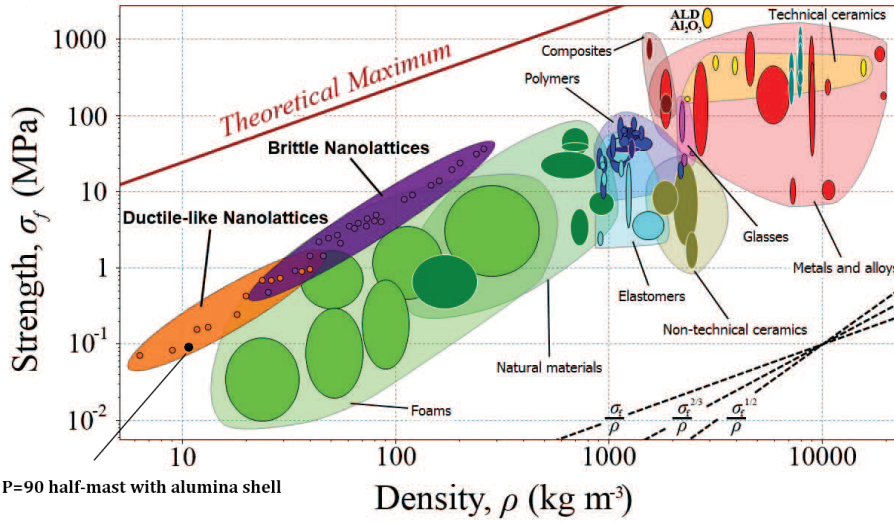


Figure 5.21: Ashby plot of Alumina nanolattices presented by Meza et al. [116]

5.7. ADDITIONAL PRELIMINARY INVESTIGATIONS

5.7.1. MIRRORED STACKED UNIT CELLS

This project has focused on the half-mast design of a metamaterial unit cell that consists of two mirrored half-masts combined. This combination allows the middle segment to freely rotate during compression while the two ends remain rotation-free. In order to gain a deeper understanding of this configuration several unit-cells (stacked half-masts) are tested. The results of this test data reveal several properties which need to be taken into consideration when researching this material further.

When a stacked unit cell is compressed, we observe an instability which results in one half mast compressing fully before the other. This is caused by the fact that the half-masts have negative stiffness after achieving a peak load (Figure 5.22), which means that if one of the masts reaches the peak stress slightly before the other then it will coil fully first. Since in reality the masts are never exactly the same (different imperfections), this double peak response tends to occur. This is clear when looking at the stress strain response plot for a half mast (Figure 5.12b for example), where after 20% strain the stress begins to decrease. This leads to an unstable bi-modal response. This issue can be solved using elements such as battens which change the shape of the half-mast response curve, but this has not been attempted here. Before proceeding to making a repeated lattice, this property should be properly investigated.

5.7.2. SCALING THE PROBLEM

As mentioned in the introduction, this dissertation aims at establishing the groundwork for a new building block of a super-compressible metamaterial. Despite the tests being

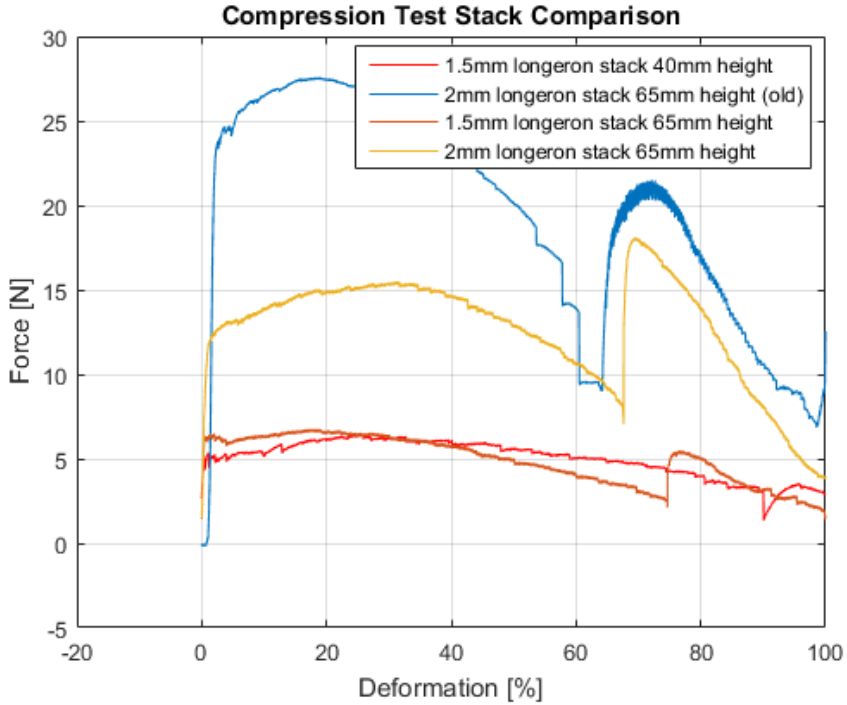
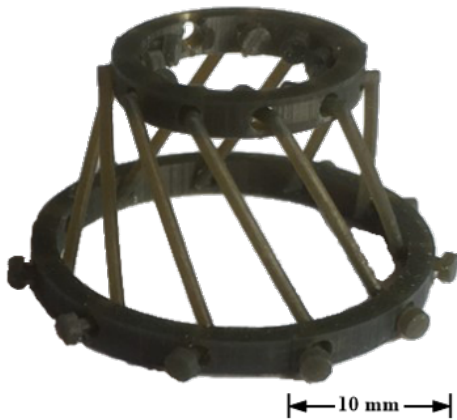


Figure 5.22: Force vs percent compression plot for various double stack masts. All masts exhibit one mast fully buckling before the other.

conducted at the macro-scale thus far, the half-mast is eventually intended for manufacture on the microscopic level in a repeated lattice containing this unit cell. A full analysis of the micro-scale prints fall outside the scope of this paper, however, the resources were available to validate that the mast indeed is printable and functional at the micro-scale. Prints were made on both the EnvisionTEC and Nanoscribe.

Figure 5.23a shows the result of manufacturing on the EnvisionTEC Micro Plus Hi-Res. This mast was able to be manufactured with HTM 140. This printing technology required a lot of support material which needs to be removed manually after printing (see Figure 5.24).

Whilst printing on the EnvisionTEC is interesting, the goal is to print on the micro level. This is done with the Nanoscribe. Several masts have been manufactured on the Nanoscribe as can be seen in Figure 5.23b. These masts can be printed both hinged and hingeless and can potentially be coated with alumina as demonstrated by Meza et al. [116]. A full analysis of the microscopic prints falls outside the scope of this thesis.



(a) Mast printed on EnvisionTEC Micro Plus Hi-Res.



(b) Double stack mast printed on Nano-scribe.

Figure 5.23



Figure 5.24: EnvisionTEC mast with support material.

6

DISCUSSION

THUS far we have showed that the data driven model works and is able to predict material response with varying degrees of accuracy. Furthermore we have shown the accuracy of material classification decreases near the borders. This section will aim to address certain aspects of the process which need more attention, as well as introduce several potential applications within the automotive sector.

The data driven approach produces design charts which guide the designer in making an optimal design for a given application. For this study, despite large uncertainty of material parameters, the finite element response data was able to very accurately predict a mast with 1 mm longerons and a pitch of 90 mm. However when probing the design space, several shortcomings at this stage were noticed and should be addressed in the future.

6.1. IMPORTANCE OF FRICTION EFFECT

Test data has shown that friction is a significant effect in the hinges of the half-mast structure. At first instance it seems that using aluminium rings with PLA longerons provided a low enough friction coefficient to not need to include friction in the simulations. This assumption is beneficial not only because it simplified the simulations, but because manufacturing this metamaterial at the micro-scale would likely a hingeless design. For this reason, quantifying and simulation friction at the macro-scale would not correspond to the micro scale masts.

Friction in the hinges has shown that it not only increases the amount of force needed to buckle the half-mast, but also changes the shape of the stress strain curve, by achieving a peak stress at a lower strain. This is seen of masts using PLA support rings rather than aluminium ones. The hinges of the PLA support rings exhibit stick slip behaviour, initially resisting the movement of the pin, resulting in a high initial peak stress at a low strain. When comparing this to the aluminium rings, which allow the hinge to rotate

more freely, the peak stress is witnessed later in the compression (20% strain). For half-masts, with thin longerons ($\ll 1.5$ mm), it appears that accurate predictions of the half-mast response can be made assuming no friction.

Probing the design space however shows that the frictionless assumption only holds for certain cases, with near vertical longerons, and low forces. Predictions for half-masts with thick longerons (3 mm diameter) shows that the FE predictions significantly and consistently under-predict stress. As friction is force dependent, this clearly shows that for half-masts buckling with higher force, friction in the hinges indeed plays a significant role and friction will therefore need to be included in the simulations.

6.2. END ROTATION IMPERFECTION (FIRST BUCKLING MODE)

Geometric imperfections of the metamaterial unit-cell were shown to cause significant differences in the mechanical response. The influence of the end rotation caused by imperfect 3D printing and the need for a large tolerance at the hinges (between longerons and support rings) was investigated by seeding the first buckling mode as an imperfection of the idealized structure. This is an obvious approximation, as there are clearly more geometric imperfections present that are not known a priori and so are challenging to accurately include into the simulations. A study conducted on $P = 60$ mm masts revealed a mean of 4 degrees with a standard deviation of 1.9 degrees for the amplitude of this first buckling mode (angle at the end), which was assumed to follow a log-normal distribution.

Now that several masts across the design space have been tested it is clear that the Mode-1 assumption only holds true for masts with parameters very similar to those on which the data was obtained i.e. point 1 in Figure 5.10. A further study finding the relationship between Mode-1 error and the parameters is needed in order to improve the ML model and FEA. Furthermore simplifying all geometric imperfections into the first buckling mode is probably insufficient, although the results were satisfactory.

6.3. REPEATED LOADING

Achieving full recoverability requires that the material should withstand repeated complete loading and unloading cycles without plasticity or damage. Looking at the $D_1 = 90$ $P = 60$ $d = 1.5$ mast (Figure 5.6a), we observe that subsequent loading cycles are at a lower force than the initial cycle (see Figure 5.9). This drop on consecutive loads was caused by small amounts of plastic deformation despite this design being classified as at the limit of fully elastic behavior by the ML classification chart, a relaxation effect which occurs in polymers, and due to friction (even when considering low friction solutions, i.e. using aluminum support rings, friction still occurs). Plastic deformation became negligible for a mast with a smaller longeron cross-section diameter ($d = 1$ mm). Evidently, plasticity can be avoided by using different base materials or selecting metamaterial geometries further from the classification boundary threshold (coilable but yields).

6.4. LONGERON CROSS SECTION

The study by Glowacki [89] concluded that the cross section shape is a critical parameter for compression response. This paper has only validated one of the simplest cases (round) and so has left a large design area still to be investigated. Figure 6.1 shows a visualisation of arbitrary cross sections. If a cross section is manufacturable, then it can greatly increase the buckling force of the mast. This is shown by Glowacki who finds the maximum achievable stress from the known material universe (carbon nano tubes) is in the order of 100 MPa using an I-beam profile.

We have seen that using alumina can also increase the compressive strength but this mast uses parameters optimised for PLA. As alumina has a much larger yield strain ($\approx 4\%$) more mast designs are possible. Furthermore the longeron cross section for such a material can be optimized to increase I_x (see Figure 6.2) by changing the cross sectional shape. Improving these parameters can elevate the compressive strength of the metamaterial to unprecedented values, while still being fully recoverable.

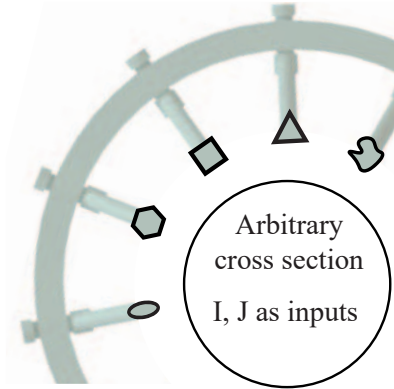


Figure 6.1: Visualization of multiple possible crossections for the longeron. For the data driven design model, J and I were included as variables, and so any possible crossection gets realised.

Note that the data driven process provides significant design flexibility, now that it has been experimentally validated, because the metamaterial structure can be optimised for many different applications without conducting additional finite element simulations. Instead, optimization can be performed directly on the machine learning model, i.e. it acts as a surrogate model.

6.5. APPLICATIONS

This project has been a feasibility study to attempt to create a new type of metamaterial unit-cell. Beyond its academic interest, considering its practical application in the

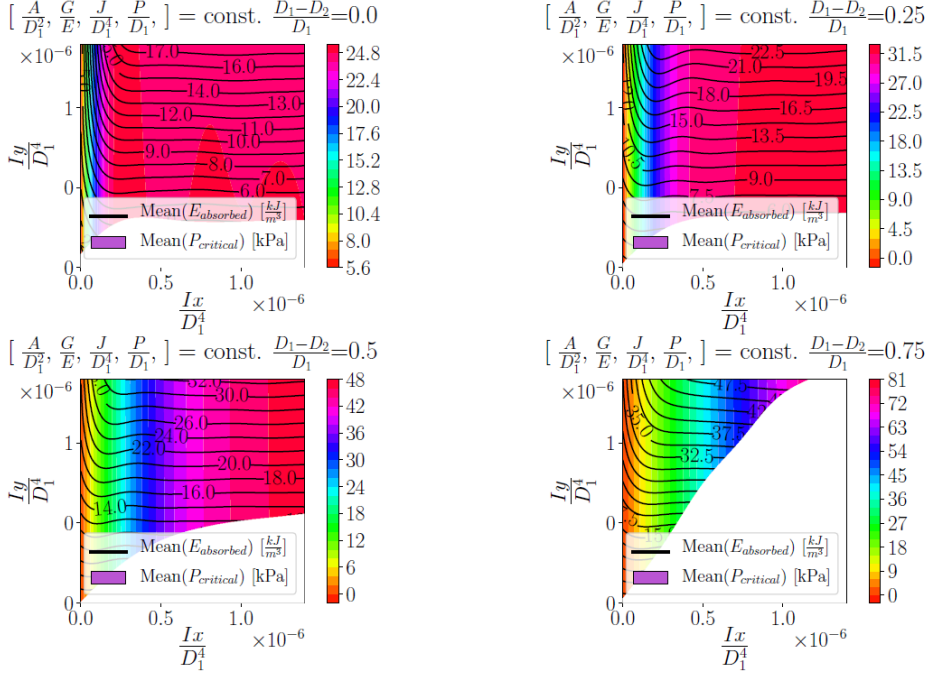


Figure 6.2: Regression plot showing influence of I_x on the peak stress and energy absorbed. I_x is greatly influenced by the cross section shape. [89]

future can be of relevance. Assuming that the unit-cell can be repeated in 3D to form a periodic lattice whose struts are the double-mast design, then the metamaterial would allow super-compressibility in all directions. This allows reconfigurability of a material into a very small volume once a peak load is achieved, while the metamaterial would retain its shape and relatively high stiffness before reaching the peak load (unlike linear springs).

Specifically for the automotive industry, this metamaterial could have important applications. Its energy absorption capabilities (large strain while having reasonable strength) can be useful for shock-absorption applications: suspension, car bumpers, automotive bodywork, etc. In addition, since this material can be impacted from any direction, crash structures could be optimized beyond the typical head on collision case studies. In these applications, considering plasticity and damage tolerance for the metamaterial would be useful, as it would increase the compressive strength and energy dissipation significantly.

7

CONCLUSION AND RECOMMENDATIONS

7.1. CONCLUSION

This thesis has contributed to the design of a novel unit-cell of a metamaterial. We have demonstrated that a data driven design framework can be a useful tool in metamaterial design. Despite the simplicity of both the simulations and classification, we have demonstrated that we can predict response behaviour. Trends are easily determined and designs which do not perform are quickly eliminated using the data driven process. The research of properties of functional complex FDM parts is also furthered.

- The mechanical response of a new metamaterial unit-cell was reasonably predicted by finite element analyses, including propagation of uncertainty of input material properties and geometric imperfections originated from additive manufacturing (fused deposition modeling).
- However, the simulations should include a friction model at the hinges between the longerons and support rings in order to be generalizable to more materials and loading conditions.
- Geometric imperfections were simulated considering the first buckling mode, i.e a small rotation at one end of the half-mast metamaterial unit-cell that originates from the physical tolerance at the hinges. However, we found experimentally that the rotation angle is unequally distributed over different designs. In addition, more realistic imperfections should be taken into consideration for improved accuracy of the simulations.
- Machine learning was shown to be useful by providing design charts that guide the experimental program to discover new materials. The design charts were remarkably accurate in predicting the regions of interest, although some designs that are

close to the boundaries were misclassified. Regardless, the data-driven approach was proven very useful in this exploratory investigation.

- A metamaterial unit-cell with large densification strain (strain at which the material behaves as the bulk material) were found. Similarly to other materials with large densification strain, the compressive strength is low. Yet, most materials achieve these densification strains when they are well beyond their elastic limit, i.e. with significant plasticity and damage. Our metamaterial can achieve reasonable compressive strengths while achieving recoverable super-compressibility (well beyond 90%).
- FDM printing was shown suitable, albeit not ideal, for 3D printing a structural part undergoing extreme behavior. However, the material properties of the base-material have large uncertainty that should be taken into consideration in the finite element analyses, as demonstrated in this dissertation. Elastic properties, yielding and (to a limited extent) damage have been characterized for different print settings, although this was not the main purpose of this investigation. Porosity, as discussed in other studies, has a strong influence on the mechanical properties of the 3D printed parts.

Metamaterial design results from explorations of extreme geometries and mechanical properties by considering vast design spaces (many design parameters). The design freedom provided by additive manufacturing has been extensively explored in the literature, but the value of data-driven design has not been shown to date.

In this dissertation we have investigated the potential of data driven design to provide accurate information to manufacture a new metamaterial. Its application to the buckling mast structure, has provided information about both the limitations and the possibilities to progress the design further. This strategy has clear benefits for structures with are complex and non intuitive. If adopted in place of an iterative design process, both existing and new metamaterial structures can be further understood and optimised.

7.2. RECOMMENDATIONS

The next step to further research the buckling mast metamaterial is to validate the concept at the micro-scale, after which a double stack can be made followed by a repeated lattice comprised of this building block. Base materials with high stiffness and with reasonable yield strains (4%) such as alumina are promising candidates to achieve unprecedented mechanical properties, as shown by the data-driven framework. A further investigation into the addition of structural elements such as battens, can also expand the design space to more applications. It is predicted that the presence of battens will permit to tune the stress-strain response such that the complete metamaterial unit-cell (double-stack mast) becomes more stable. Lastly an analysis of the friction of pivoting points of the unit cell (whether hinged or hingeless) need to be included into the simulation, as we showed this significantly impacts mast response to loading.

- FDM parts are more sensitive to shape imperfections when loaded in torsion than tension. Caution should be used when designing functional FDM components

which will be loaded extensively in shear. Part diameters which are a multiple of the print nozzle diameter will help reduce porosity.

- It is shown that the half-mast structure made of 3D-printed PLA cannot match the state of the art with respect to compressive strength without plastic deformation occurring. Alternative materials will need to be investigated to further push the metamaterial properties.
- The influence of different geometric imperfections needs to be better understood and implemented for improved accuracy of the computational predictions.
- To further explore the metamaterial design, the design space needs to be broadened by considering more parameters such as the cross section shape.
- There should be substantial benefits in exploring a hingeless structure by using torsional beams at to top and bottom.
- In addition, considering metallic and ceramic coatings (e.g. alumina) should improve the mechanical performance significantly.
- Lastly, the full unit cell needs to be validated for the hingeless design, followed by implementation in a lattice.

REFERENCES

- [1] Y. Bienvenu, *Application and future of solid foams*, [Comptes Rendus Physique](#) **15**, 719 (2014).
- [2] G. D. L. Chart created using CES EduPack 2018, [Material property charts](#), (2018).
- [3] T. Mullin, S. Deschanel, K. Bertoldi, and M. C. Boyce, *Pattern transformation triggered by deformation*, [Physical Review Letters](#) **99**, 1 (2007).
- [4] T. A. Schaedler, A. J. Jacobsen, A. Torrents, A. E. Sorensen, J. Lian, J. R. Greer, L. Valdevit, and W. B. Carter, *Ultralight metallic microlattices*, [Science](#) **334**, 962 (2011).
- [5] X. Zheng, H. Lee, and T. H. Weisgraber, *Ultralight, Ultrastiff Mechanical Metamaterials*, **344**, 1373 (2014).
- [6] M. A. Bessa, R. Bostanabad, Z. Liu, A. Hu, D. W. Apley, C. Brinson, W. Chen, and W. K. Liu, *A framework for data-driven analysis of materials under uncertainty: Countering the curse of dimensionality*, [Computer Methods in Applied Mechanics and Engineering](#) **320**, 633 (2017).
- [7] M. A. Bessa and S. Pellegrino, *Design of ultra-thin shell structures in the stochastic post-buckling range using Bayesian machine learning and optimization*, [International Journal of Solids and Structures](#) **0**, 1 (2018).
- [8] J. Pendry, *Beyond metamaterials*, [Nature Materials](#) **5**, 763 (2006).
- [9] N. Fang, D. Xi, J. Xu, M. Ambati, W. Srituravanich, C. Sun, and X. Zhang, *Ultrasonic metamaterials with negative modulus*, [Nature Materials](#) **5**, 452 (2006), [arXiv:arXiv:1507.02142v2](#).
- [10] A. Rafsanjani, A. Akbarzadeh, and D. Pasini, *Snapping Mechanical Metamaterials under Tension*, [Advanced Materials](#) **27**, 5931 (2015), [arXiv:1612.05987](#).
- [11] K. Bertoldi, V. Vitelli, J. Christensen, and M. V. Hecke, *Flexible mechanical metamaterials*, [Nature](#) **2** (2017), [10.1038/natrevmats.2017.66](#).
- [12] X. Yu, J. Zhou, H. Liang, Z. Jiang, and L. Wu, *Mechanical metamaterials associated with stiffness, rigidity and compressibility: A brief review*, [Progress in Materials Science](#) **94**, 114 (2018).
- [13] R. Hedayati, M. J. Mirzaali, L. Vergani, and A. A. Zadpoor, *Action-at-a-distance metamaterials: Distributed local actuation through far-field global forces*, [APL Materials](#) **6** (2018), [10.1063/1.5019782](#).

- [14] J. N. Grima and R. Caruana-Gauci, *Mechanical metamaterials: Materials that push back*, [Nature Materials](#) **11**, 565 (2012).
- [15] M. J. Mirzaali, S. Janbaz, M. Strano, L. Vergani, and A. A. Zadpoor, *Shape-matching soft mechanical metamaterials*, [Scientific Reports](#) **8**, 1 (2018).
- [16] J. L. Silverberg, A. A. Evans, L. McLeod, R. C. Hayward, T. Hull, C. D. Santangelo, and I. Cohen, *Using origami design principles to fold reprogrammable mechanical metamaterials*, [Science](#) **345**, 647 (2014).
- [17] C. Zhu, T. Y. J. Han, E. B. Duoss, A. M. Golobic, J. D. Kuntz, C. M. Spadaccini, and M. A. Worsley, *Highly compressible 3D periodic graphene aerogel microlattices*, [Nature Communications](#) **6**, 1 (2015).
- [18] L. R. Choi, J, *choi1994.pdf* (University of Iowa, Iowa City, 1994) pp. 113–128.
- [19] L. J. Gibson, *Cellular Solids*, [MRS Bulletin](#) (2003), 10.1557/mrs2003.79, [arXiv:arXiv:1011.1669v3](#).
- [20] R. Lakes, *Materials with structure hierarchy*, [Nature](#) **361**, 511 (1993).
- [21] L. Zhang, S. Feih, S. Daynes, Y. Wang, M. Y. Wang, J. Wei, and W. F. Lu, *Buckling optimization of Kagome lattice cores with free-form trusses*, [Materials and Design](#) **145**, 144 (2018).
- [22] E. Barchiesi, M. Spagnuolo, and L. Placidi, *Mechanical metamaterials: a state of the art*, [Mathematics and Mechanics of Solids](#) (2018), 10.1177/1081286517735695.
- [23] T. Tancogne-Dejean and D. Mohr, *Stiffness and specific energy absorption of additively-manufactured metallic BCC metamaterials composed of tapered beams*, [International Journal of Mechanical Sciences](#) **141**, 101 (2018).
- [24] H. M. Kolken and A. A. Zadpoor, *Auxetic mechanical metamaterials*, [RSC Advances](#) **7**, 5111 (2017).
- [25] J. N. Grima, R. Gatt, and P. S. Farrugia, *On the properties of auxetic meta-tetrachiral structures*, in [Physica Status Solidi \(B\) Basic Research](#) (2008).
- [26] K. W. Wojciechowski, *Two-dimensional isotropic system with a negative poisson ratio*, [Physics Letters A](#) **137**, 60 (1989).
- [27] D. Prall and R. S. Lakes, *chiral honeycombe. Poisson's ratio. 1. INTRODUCTION Cellular solids are used widely in a variety of engineering applications. In particular,* **39** (1997).
- [28] T. Frenzel, M. Kadic, and M. Wegener, *Three-dimensional mechanical metamaterials with a twist*, [Science](#) **358**, 1072 (2017).
- [29] E. T. Filipov, T. Tachi, and G. H. Paulino, *Origami tubes assembled into stiff, yet re-configurable structures and metamaterials*, [Proceedings of the National Academy of Sciences](#) **112**, 12321 (2015), [arXiv:arXiv:1408.1149](#).

- [30] S. J. Callens and A. A. Zadpoor, *From flat sheets to curved geometries: Origami and kirigami approaches*, [Materials Today](#) **21**, 241 (2018).
- [31] S. Felton, M. Tolley, E. Demaine, D. Rus, and R. Wood, *A method for building self-folding machines*, [Science](#) **345**, 644 (2014).
- [32] M. Schenk and S. D. Guest, *Geometry of Miura-folded metamaterials*, [Proceedings of the National Academy of Sciences](#) **110**, 3276 (2013).
- [33] X. M. Xiang, G. Lu, D. Ruan, Z. You, and M. Zolghadr, *Large deformation of an arc-Miura structure under quasi-static load*, [Composite Structures](#) **182**, 209 (2017).
- [34] N. Hu and R. Burgueño, *Buckling-induced smart applications: Recent advances and trends*, [Smart Materials and Structures](#) **24** (2015), 10.1088/0964-1726/24/6/063001.
- [35] B. Haghpanah, L. Salari-Sharif, P. Pourrajab, J. Hopkins, and L. Valdevit, *Architected Materials: Multistable Shape-Reconfigurable Architected Materials* (*Adv. Mater.* 36/2016), [Advanced Materials](#) **28**, 8065 (2016).
- [36] Z. G. Nicolaou and A. E. Motter, *Mechanical metamaterials with negative compressibility transitions*, [Nature Materials](#) **11**, 608 (2012), [arXiv:1207.2185](#).
- [37] G. N. Greaves, A. L. Greer, R. S. Lakes, and T. Rouxel, *Poisson's ratio and modern materials*, [Nature Materials](#) **10**, 823 (2011).
- [38] S. Babaei, J. Shim, J. C. Weaver, E. R. Chen, N. Patel, and K. Bertoldi, *3D soft metamaterials with negative poisson's ratio*, [Advanced Materials](#) **25**, 5044 (2013).
- [39] T. Bückmann, N. Stenger, M. Kadic, J. Kaschke, A. Frölich, T. Kennerknecht, C. Eberl, M. Thiel, and M. Wegener, *Tailored 3D mechanical metamaterials made by dip-in direct-laser-writing optical lithography*, [Advanced Materials](#) **24**, 2710 (2012).
- [40] W. Wang, H. Rodrigue, and S. H. Ahn, *Deployable Soft Composite Structures*, [Scientific Reports](#) **6**, 1 (2016).
- [41] L. Sun, W. M. Huang, Z. Ding, Y. Zhao, C. C. Wang, H. Purnawali, and C. Tang, *Stimulus-responsive shape memory materials: A review*, [Materials and Design](#) **33**, 577 (2012).
- [42] G. Zu, K. Kanamori, T. Shimizu, Y. Zhu, A. Maeno, H. Kaji, K. Nakanishi, and J. Shen, *Versatile Double-Cross-Linking Approach to Transparent, Machinable, Supercompressible, Highly Bendable Aerogel Thermal Superinsulators*, [Chemistry of Materials](#) **30**, 2759 (2018).
- [43] L. Qiu, B. Huang, Z. He, Y. Wang, Z. Tian, J. Z. Liu, K. Wang, J. Song, T. R. Gengenbach, and D. Li, *Extremely Low Density and Super-Compressible Graphene Cellular Materials*, [Advanced Materials](#) **29**, 1 (2017).

- [44] A. Cao, P. L. Dickrell, and W. G. Sawyer, *Super-Compressible Foamlike Carbon Nanotube Films*, **310**, 1307 (2005).
- [45] T. Kitamura, K. Okazaki, M. Natori, K. Miura, S. Sato, and A. Obata, *Development of a "HINGELESS MAST" and its Applications*, *Acta Astronautica* **17**, 341 (1988).
- [46] L. Puig, A. Barton, and N. Rando, *A review on large deployable structures for astrophysics missions*, *Acta Astronautica* **67**, 12 (2010).
- [47] *Structural Dynamics and Materials Conference* (Orlando, Florida, 1985).
- [48] X. Zhou, G. Yue, H. Huang, and X. Wang, *Deployment analysis and test of a coilable mast for BUAA student micro-satellite*, *ISSCAA2010 - 3rd International Symposium on Systems and Control in Aeronautics and Astronautics*, 1329 (2010).
- [49] R. CRAWFORD, *Strength and efficiency of deployable booms for space applications*, *12th Structures, Structural Dynamics and Materials Conference* (1971), doi:10.2514/6.1971-396.
- [50] H. Ma, H. Huang, J. Han, W. Zhang, and X. Wang, *Study on the criterion to determine the bottom deployment modes of a coilable mast*, *Acta Astronautica* **141**, 89 (2017).
- [51] D. M. Murphy, T. W. Murphey, and P. A. Gierow, *Scalable Solar Sail Subsystem Design Considerations*, *Space Technology* (2002).
- [52] S. Arita, I. Fukuta, Y. Yamagiwa, and Y. Miyazaki, *A Proposal of New Deployable Space Structure Applying Buckling*, **1** (2018).
- [53] N/A, *Casting Design and Performance* (ASM International, 2009).
- [54] T. A. E. Altan, Tayla, *Sheet Metal Forming - Fundamentals* (ASM International, 2012).
- [55] E. J. A. Armarego and R. H. Brown, *TA - TT* - (Prentice-Hall, Englewood Cliffs, N.J. SE - ix, 437 pages illustrations 25 cm, 1969).
- [56] J. D. Buckley and B. A. Stein, *TA - TT* - (Noyes Data Corp., Park Ridge, N.J., U.S.A. SE - xviii, 480 pages : illustrations ; 25 cm, 1986).
- [57] H. J.-S. Gebhardt, Andreas, *Additive Manufacturing - 3D Printing for Prototyping and Manufacturing* (Hanser Publishers, 2016).
- [58] E. Puik, L. Van Moergestel, and D. Telgen, *Cost modelling for micro manufacturing logistics when using a grid of equilets*, (2011) cited By 3.
- [59] M. Vaezi, H. Seitz, and S. Yang, *A review on 3D micro-additive manufacturing technologies*, *International Journal of Advanced Manufacturing Technology* **67**, 1721 (2013), arXiv:arXiv:1011.1669v3 .

- [60] T. D. Ngo, A. Kashani, G. Imbalzano, K. T. Nguyen, and D. Hui, *Additive manufacturing (3D printing): A review of materials, methods, applications and challenges*, *Composites Part B: Engineering* **143**, 172 (2018).
- [61] L. Li, A. Haghighi, and Y. Yang, *A novel 6-axis hybrid additive-subtractive manufacturing process: Design and case studies*, *Journal of Manufacturing Processes* **33**, 150 (2018).
- [62] S.-h. Ahn, M. Montero, and P. K. Wright, *Anisotropic material properties of fused deposition modeling ABS* (2012).
- [63] J. Z. Manapat, Q. Chen, P. Ye, and R. C. Advincula, *3D Printing of Polymer Nanocomposites via Stereolithography*, *Macromolecular Materials and Engineering* **302**, 1 (2017).
- [64] B. Gupta, N. Revagade, and J. Hilborn, *Poly(lactic acid) fiber: An overview*, *Progress in Polymer Science (Oxford)* **32**, 455 (2007).
- [65] J. R. Tumbleston, D. Shirvanyants, N. Ermoshkin, R. Januszewicz, A. R. Johnson, D. Kelly, K. Chen, R. Pinschmidt, J. P. Rolland, A. Ermoshkin, E. T. Samulski, and J. M. Desimone, *Continuous liquid interface of 3D objects*, *Science* **347**, 1349 (2015).
- [66] Z. Weng, J. Wang, T. Senthil, and L. Wu, *Mechanical and thermal properties of ABS/montmorillonite nanocomposites for fused deposition modeling 3D printing*, *Materials and Design* **102**, 276 (2016).
- [67] J. A. Lewis, *Direct ink writing of 3D functional materials*, *Advanced Functional Materials* **16**, 2193 (2006).
- [68] O. A. Mohamed, S. H. Masood, and J. L. Bhowmik, *Optimization of fused deposition modeling process parameters: a review of current research and future prospects*, *Advances in Manufacturing* **3**, 42 (2015), arXiv:arXiv:1011.1669v3 .
- [69] A. K. Sood, R. K. Ohdar, and S. S. Mahapatra, *Parametric appraisal of fused deposition modelling process using the grey Taguchi method*, *Proceedings of the Institution of Mechanical Engineers, Part B: Journal of Engineering Manufacture* **224**, 135 (2010).
- [70] J. S. Chohan, R. Singh, K. S. Boparai, R. Penna, and F. Fraternali, *Dimensional accuracy analysis of coupled fused deposition modeling and vapour smoothing operations for biomedical applications*, *Composites Part B: Engineering* **117**, 138 (2017).
- [71] U. BV, *Ultimaker 3*, (2011-2018).
- [72] P. Parandoush and D. Lin, *A review on additive manufacturing of polymer-fiber composites*, *Composite Structures* **182**, 36 (2017).
- [73] J. R. C. Dizon, A. H. Espera, Q. Chen, and R. C. Advincula, *Mechanical characterization of 3D-printed polymers*, *Additive Manufacturing* **20**, 44 (2018).

- [74] F. P. Melchels, J. Feijen, and D. W. Grijpma, *A review on stereolithography and its applications in biomedical engineering*, [Biomaterials](#) **31**, 6121 (2010).
- [75] X. Wang, M. Jiang, Z. Zhou, J. Gou, and D. Hui, *3D printing of polymer matrix composites: A review and prospective*, [Composites Part B: Engineering](#) **110**, 442 (2017).
- [76] K. Chen, C. A. Us, J. Poelma, C. A. Us, J. Goodrich, A. Z. Us, R. Pinschmidt, J. M. Desimone, C. A. Us, and L. M. Robeson, (12) *United States Patent*, Vol. 2 (2016).
- [77] B. Utela, D. Storti, R. Anderson, and M. Ganter, *A review of process development steps for new material systems in three dimensional printing (3DP)*, [Journal of Manufacturing Processes](#) **10**, 96 (2008).
- [78] R. Dou, T. Wang, Y. Guo, and B. Derby, *Ink-jet printing of zirconia: Coffee staining and line stability*, [Journal of the American Ceramic Society](#) **94**, 3787 (2011).
- [79] N. Travitzky, A. Bonet, B. Dermeik, T. Fey, I. Filbert-Demut, L. Schlier, T. Schlördt, and P. Greil, *Additive manufacturing of ceramic-based materials*, [Advanced Engineering Materials](#) **16**, 729 (2014).
- [80] I. Gibson, D. W. Rosen, and B. Stucker, *Additive Manufacturing Technologies: Rapid Prototyping to Direct Digital Manufacturing*, 1st ed. (Springer Publishing Company, Incorporated, 2009).
- [81] R. Hahnlen and M. J. Dapino, *NiTi-Al interface strength in ultrasonic additive manufacturing composites*, [Composites Part B: Engineering](#) **59**, 101 (2014).
- [82] A. Hehr and M. J. Dapino, *Interfacial shear strength estimates of NiTi-Al matrix composites fabricated via ultrasonic additive manufacturing*, [Composites Part B: Engineering](#) **77**, 199 (2015).
- [83] J. H. Martin, B. D. Yahata, J. M. Hundley, J. A. Mayer, T. A. Schaedler, and T. M. Pollock, *3D printing of high-strength aluminium alloys*, [Nature](#) **549**, 365 (2017).
- [84] H. Zhang, H. Zhu, T. Qi, Z. Hu, and X. Zeng, *Selective laser melting of high strength Al-Cu-Mg alloys: Processing, microstructure and mechanical properties*, [Materials Science and Engineering A](#) **656**, 47 (2016).
- [85] A. Takezawa and M. Kobashi, *Design methodology for porous composites with tunable thermal expansion produced by multi-material topology optimization and additive manufacturing*, [Composites Part B: Engineering](#) **131**, 21 (2017).
- [86] M. Ramasamy and V. K. Varadan, *3D printing of nano- and micro-structures*, , 98020H (2016).
- [87] N. GmbH, [Technology](#), (2011-2018).
- [88] N. GmbH, [Additive manufacturing](#), (2011-2018).

- [89] P. Glowacki, *Data - driven design of a metamaterial unit cell using sparse gaussian processes*, (2019).
- [90] U. BV, *Ultimaker 2*, (2011-2018).
- [91] P. Hackney and K. Pancholi, *Analysis of the envisiontec perfactory system for rapid production of components and validation utilizing finite element and photo-elastic analysis*, (2004) pp. 93–99, cited By 0.
- [92] L. R. Meza, A. J. Zelhofer, N. Clarke, A. J. Mateos, D. M. Kochmann, and J. R. Greer, *Resilient 3D hierarchical architected metamaterials*, (2015), [10.1073/pnas.1509120112](https://doi.org/10.1073/pnas.1509120112).
- [93] A. Schroer, J. M. Wheeler, and R. Schwaiger, *Deformation behavior and energy absorption capability of polymer and ceramic-polymer composite microlattices under cyclic loading*, *Journal of Materials Research* **33**, 274 (2018).
- [94] J. Torres, J. Cotel, J. Karl, and A. P. Gordon, *Mechanical property optimization of FDM PLA in shear with multiple objectives*, *Jom* **67**, 1183 (2015).
- [95] M. Somireddy and A. Czekanski, *Mechanical Characterization of Additively Manufactured Parts by FE Modeling of Mesostructure*, , **1** (2017).
- [96] J. Floor, *GETTING A GRIP ON THE ULTIMAKER 2 TENSILE STRENGTH OF 3D PRINTED PLA: A SYSTEMATIC INVESTIGATION*, TUDelft Master Thesis , 116 (2018).
- [97] S. H. Ahn, M. Montero, D. Odell, S. Roundy, and P. K. Wright, *Anisotropic material properties of fused deposition modeling ABS*, *Rapid Prototyping Journal* **8**, 248 (2002).
- [98] A. Bagsik and D. Manufacturing, *MECHANICAL PROPERTIES OF FUSED DEPOSITION MODELING PARTS MANUFACTURED WITH ULTEM * 9085* *Material l To analyze the influence of the toolpath parameters*, Direct , 1294 (2011).
- [99] A. K. Sood, R. K. Ohdar, and S. S. Mahapatra, *Parametric appraisal of mechanical property of fused deposition modelling processed parts*, *Materials and Design* **31**, 287 (2010).
- [100] J. Cantrell, S. Rohde, D. Damiani, R. Gurnani, L. Di Sandro, J. Anton, A. Young, A. Jerez, D. Steinbach, C. Kroese, and P. Ifju, *Experimental characterization of the mechanical properties of 3D printed ABS and polycarbonate parts*, *Conference Proceedings of the Society for Experimental Mechanics Series* **3**, 89 (2017).
- [101] S. Rohde, J. Cantrell, A. Jerez, C. Kroese, D. Damiani, R. Gurnani, L. DiSandro, J. Anton, A. Young, D. Steinbach, and P. Ifju, *Experimental Characterization of the Shear Properties of 3D-Printed ABS and Polycarbonate Parts*, *Experimental Mechanics* **58**, 871 (2018).

- [102] L. Singh Mehta and P. Pillai, *Compression Testing of PLA in 3D Printing*, Priam Pillai International Journal of Electronics **6**, 466 (2017).
- [103] ASTM International, *Standard Test Method for Compressive Properties of Rigid Plastics*, ASTM International **08**, 46 (2019).
- [104] Y. Jiang and Q. Wang, *Highly-stretchable 3D-architected Mechanical Metamaterials*, *Scientific Reports* **6**, 1 (2016).
- [105] Y. Song, Y. Li, W. Song, K. Yee, K. Y. Lee, and V. L. Tagarielli, *Measurements of the mechanical response of unidirectional 3D-printed PLA*, *Materials and Design* **123**, 154 (2017).
- [106] C. O. Balderrama-Armendariz, E. MacDonald, D. Espalin, D. Cortes-Saenz, R. Wicker, and A. Maldonado-Macias, *Torsion analysis of the anisotropic behavior of FDM technology*, *International Journal of Advanced Manufacturing Technology* **96**, 307 (2018).
- [107] A. H. V. D. Boogaard, *MEASUREMENTS AND CALCULATIONS ON YIELD SURFACES IN TENSION – SIMPLE SHEAR EXPERIMENTS*. **31**, 61 (2008).
- [108] A. Jung and S. Diebels, *Yield surfaces for solid foams: A review on experimental characterization and modeling*, *GAMM Mitteilungen* **41**, 1 (2018).
- [109] H.-c. Wu, *Effect of loading-path on the evolution of yield surface for anisotropic metals subjected to large pre-strain*, **19**, 1773 (2003).
- [110] F. Kabirian and A. S. Khan, *Anisotropic yield criteria in $r-s$ stress space for materials with yield asymmetry*, *International Journal of Solids and Structures* **67-68**, 116 (2015).
- [111] V. Pre-deformation, G.-l. Liu, S.-h. Huang, C.-s. Shi, B. Zeng, K.-s. Zhang, and X.-c. Zhong, *Experimental Investigations on Subsequent Yield Surface of Pure Copper by Single-Sample and*, [10.3390/ma11020277](https://doi.org/10.3390/ma11020277).
- [114] R. Raghava, R. M. Caddell, and G. S. Y. Yeh, *The macroscopic yield behaviour of polymers*, *Journal of Materials Science* **8**, 225 (1973).
- [112] A. R. Melro, P. P. Camanho, F. M. Andrade Pires, and S. T. Pinho, *Micromechanical analysis of polymer composites reinforced by unidirectional fibres: Part I- Constitutive modelling*, *International Journal of Solids and Structures* **50**, 1897 (2013).
- [113] X. Bai, M. A. Bessa, A. R. Melro, P. P. Camanho, L. Guo, and W. K. Liu, *High-fidelity micro-scale modeling of the thermo-visco-plastic behavior of carbon fiber polymer matrix composites*, *Composite Structures* **134**, 132 (2015).
- [115] M. Shaw, P. Tsang, and S. Rhee, *Study of the friction and wear behavior of aluminum composites sliding against polymer composites*, (1991) pp. 167–175, cited By 2.

- [116] L. R. Meza, S. Das, and J. R. Greer, *Supplementary-Strong , Lightweight and Recoverable Three - Dimensional Ceramic Nanolattices*, [Submitted 345, 1322 \(2014\)](#).
- [117] K. Madhavan Nampoothiri, N. R. Nair, and R. P. John, *An overview of the recent developments in polylactide (PLA) research*, (2010).
- [118] M. Konakovic, K. Crane, B. Deng, S. Bouaziz, D. Piker, and M. Pauly, *Beyond Developable: Computational Design and Fabrication with Auxetic Materials*, [ACM Transactions on Graphics 35, 1 \(2016\)](#).
- [119] B. Wittbrodt and J. M. Pearce, *The effects of PLA color on material properties of 3-D printed components*, [Additive Manufacturing 8, 110 \(2015\)](#), [arXiv:arXiv:1011.1669v3](#).
- [120] B. Ilic, S. Krylov, and H. G. Craighead, *Young's modulus and density measurements of thin atomic layer deposited films using resonant nanomechanics*, [Journal of Applied Physics 108 \(2010\)](#), [10.1063/1.3474987](#).



LIST OF TESTS

Table A.1: List of performed tests, for both material and mast properties

Date	Test type	Machine
09-07-18	ASTM D638-14 100 % diagonal infill 0.2mm layer height	Zwick z10
09-07-18	Double stack mast testing with Pitch 65 and 45 mm	Zwick z10
13-07-18	Double stack mast testing with New print method (2 component)	Zwick z10
28-07-18	Tensile test on 1.5 mm, 2 mm round and square dogbone specimens	Instron
03-09-18	Testing validity of cone for free rotating side	Zwick z10
03-09-18	Half-Mast compression using cone	Instron
06-09-18	ASTM D638-14 100 % diagonal infill 0.06mm layer height	Zwick z10
25-10-18	Half-Mast compression using cone	Zwick z10
04-11-18	Half-Mast compression with metal rings	Instron
15-11-18	ASTM D695-15 Compression Testing	Zwick z10
16-11-18	Tensile test 1.5 mm longeron	Instron
26-11-18	Attempt compression testing 1.5 mm longeron specimen	Instron
03-12-18	ASTM D638-14 Tension test with Unidirectional Fibres & Strain guage	Zwick z10
03-12-18	ASTM D695-15 Compression Testing Scaled	Zwick z10
05-12-18	Torsion test PME	Zwick
16-01-19	ASTM D638-14 Tension test with +_ 45 deg Fibres & Strain guage	Zwick z10
16-01-19	ASTM D695-15 Compression Testing scaled specimen & unidirectional fibres	Zwick z10
25-01-19	Combined Shear,tension/compression yield surface test PME	Zwick
29-01-19	Compression,Tension,Shear test	Zwick
11-02-19	Compression half-mast cone with metal rings	Instron
01-03-19	Compression p90 half-mast ball bearing & metal rings	Instron

Remark 7 *Zwick: refers to an experimental prototype Zwick machine used at PME department of 3ME, TUDelft. This machine is a hybrid of a torsion and tension tester and is operated solely by qualified technicians.*

B

ULTIMAKER 2 PRINTERS AND USED MATERIAL

B.1. ULTIMAKER 2 PRINT PROCESS

The Mechanical, Maritime and Materials Engineering faculty at the Delft University of Technology has four different printers that are considered in this thesis: the Ultimaker 2 [90], the EnvisionTEC Per factory 4mini XL [91], the EnvisionTEC Micro Plus Hi-Res [91], and the Nanoscribe [39, 59, 92, 93]. These printers use fundamental different printing technologies and are used at different stages of the development of the metamaterial design. Due to the costs and availability involved in using each of the printers (increasing from Ultimaker to Nanoscribe), the main focus of this paper is on macro-scale printing with the Ultimaker. Therefore, the PLA (polylactic acid) material used with this printer is studied in detail (see Appendix B.3).

There is a significant variation between identical prints on the same printer. This is in part caused by the manner in which the Ultimaker 2 operates. The printing process will be briefly explained as well as issues which are of note will be labeled with a letter and discussed in the following paragraph.

Start, the print bed heats up to a temperature of 60 degrees Celsius, and the print nozzle to a temperature of 220 degrees Celsius. The nozzle extrudes waste material in the corner of the printbed (A). After extruding material into the corner of the print bed, the nozzle approaches the starting position of the structure and begins (B). The first layer is then printed in its entirety (C), followed by a raising of the nozzle and each subsequent layer (D). After printing is complete the printer is cooled and the part is removed. The build plate adhesion and support material need to be removed by hand (E). PLA absorbed moisture which causes swelling. To minimize this effect all material tests were conducted within a week of printing.

- (a) This is where variation can begin, as it is random whether or not that waste mate-

rial remains in the corner out of place, that it gets dragged into the print itself and causes variation in a certain section of the print.

- (b) The approach to the starting position is a diagonal slope to the initial starting height. This results in one road of undesired material underneath the printed part.
- (c) The printbed alignment is key to the quality of the print. A poorly aligned printbed will result in the first layer being incorrect, and error subsequently getting worse with subsequent layers.
- (d) As the PLA cools from 220 to 60 degrees Celsius it shrinks. In some cases the poor first layer can lead to bad adhesion to the print bed, and the shrinking effect causes the part to bend off the print bed, resulting in an improper part.
- (e) The support material is attached to the part by the nozzle skipping one layer of the print. This in short means that the following layer is printed in midair and should only very poorly adhere to the support material. This may work adequately for large parts, however as can be seen in Figure 4.3, one edge of the longeron is greatly affected by the support material.
- (f) In extreme cases, source of error C & D can ruin the entire print, by the print head knocking into the part on the successive passes. The effect of the print head bumping into the raised material can lift the part off of the printbed, meaning the print can be discarded.
- (g) Some other variables which can affect the print in minor ways include
 - (a) cleanliness of print bed
 - (b) ambient temperature
 - (c) friction between print head and guide rails.

B.2. PRINTING SETTINGS

The TUDelft 3ME Ultimaker 2 printers were made available for this project. This is an expensive way in which a lot of parts can be manufactured and tested. These printers are available to all students at the university and are managed by the IWS department. This means that altering print settings in order to improve results was not an option and so the standard settings used by the IWS needed to be respected. Special permission was given however to lower the layer height, and force the fibers into a uniform direction via increasing wall thickness. The used print settings can be seen in Figure B.1. This printing setup, however convenient, does result in extra variation (in some cases extreme) between supposedly identical parts. There are 6 printers managed by IWS and the part gets printed on the next available unit. The wear and age of these printers is different and perhaps most importantly the printbed height alignment is different.

B.3. POLYLACTIC ACID

Several printable filaments are available for the Ultimaker 2, the faculty of 3me only offers polylactic acid (PLA). Since we are limited by this material and production choice, it is important to obtain a better understanding of PLA, its properties and how it will react. Properly understanding the material we are working with will allow us to predict what will happen when changing materials and production methods.

PLA or polylactide, which means the polymerization of cyclic lactic acid [117]. It is a semi-crystalline thermoplastic that is known to have relatively large amorphous phase. Having a low glass transition temperature of roughly 55 to 60 degrees Celsius [118] and a melting temperature of just 150-160 degrees [96] make it good for 3D-printing and injection moulding. PLA is a thermoset rather than a thermoplast, making it highly recyclable as it can be remelted several times without significant loss or degradation. On the other hand thermosets cannot be re-molten once set, they would simply burn.

Wittbrodt et al. [119] investigates how crystallinity affects the tensile properties of PLA. The results show a strong relationship between tensile strength and percentage crystallinity which is in part caused by the variance in extruder temperature [119].

B.3.1. SUPERIOR MATERIAL CHOICE

Although this study is using PLA to validate the structure, any printable material can be used. Graphene could be one possible material choice. Its properties include high specific surface area, superior elasticity, chemical stability, and high thermal and electrical conductivity [17]. Making a three-dimensional graphene based material can therefore be hugely beneficial to improving mechanical metamaterials. Several papers in literature propose graphene structures which are highly compressible. Zhu et al. [17] proposed a method for fabricating graphene aerogel micro lattices through 3D printing. The fabrication process discussed in (manufacturing) allows Zhu et al. to create a graphene micro lattice with a density of 53 mg/cm^3 , which can fully recover from a 50% strain after multiple loads.

Alumina coated polymers, and hollow alumina shells are being extensively researched at the micro scale. With a strain limit of roughly 4% and a Young's modulus of 350 GPa [120]. This allows for far higher compressive strains at the microscopic scale relative to that achieved at the macroscopic scale with PLA.

Even when limited to the Ultimaker 2, using a different print filament can improve the material properties. TPU (Thermoplastic Polyurethane) for example has a similar tensile modulus to PLA but a tensile strain limit of 6%, 3 times that for PLA, dramatically increasing the design window for the part [90].

Ultimaker 2

Instelling voor Printen

Aanbevolen

Aangepast

Profiel:

Normal - 0.15mm

Zoeken...

Kwaliteit

Laaghoogte

0.06

mm

Lijnbreedte

0.4

mm

Lijnbreedte Wand

0.4

mm

Shell

Wanddikte

2

mm

Aantal Wandlijnen

5

Dikte Boven-/Onderkant

0.8

mm

Dikte Bovenkant

0.8

mm

Bovenlagen

14

Bodemdikte

0.8

mm

Bodemlagen

14

Horizontale Uitbreiding

0

mm

Vulling

Dichtheid Vulling

20

%

Vulpatroon

Raster

Materiaal

Intrekken Inschakelen

☒

Snelheid

Printsnelheid

60

mm/s

Beweging

Z-sprong wanneer ingetrokken

☐

Koelen

Koelen van de Print Inschakelen

☒

Ventilatorsnelheid

100.0

%

Supportstructuur

Support genereren

☐

Hechting aan Platform

Type Hechting aan Platform

Brim

Breedte Brim

8.0

mm

Dubbele Doorvoer

Speciale Modi

Printvolgorde

Eén voor Eén

Figure B.1: Cura printing settings used for the Ultimaker 2

C

LONGERONS

The longerons are the defining part of the mast structure, and imperfections in the longerons can greatly affect mast response. This section will look closely at the variation in mast diameters, illustrate what a poorly printed longeron looks like, and provide a better understanding of the mesostructure.

The longeron properties depend on several print settings, which as mentioned above, we have little control over. For consistency and simplicity, round longerons were chosen for the masts, however any shape would be possible, as represented in Figure C.1. To get the longerons as round as possible, a lower layer height is required, this also helps deal with surface finish, but these are not the best printing parameters.

C.1. FAILED PRINTS

Figure C.2 shows a typical example of a failed longeron print. Little over half the cross-sectional area remains intact. This error is likely caused by a poor built plate alignment causing the first initial layer not to adhere properly. This results in fibres that are poorly joined together, in some cases not at all.

C.2. PIN-HOLE RELATIONSHIP

As mentioned in the design optimisation, the pins were a source of great friction and error in the mast. The extent was so high that PLA rings were abandoned for the testing and replaced with aluminium ones. The figures below illustrate some of the issues with regard to misalignment (Figure C.3a) and with regard to roughness (Figure C.3b)

C.3. LONGERON CROSS SECTION

As noted before, for material testing and obtaining the Young's modulus, area is of vital importance. During the experiments a Mitutoyo Absolute Digital Micrometer QuickMike 0-30mm is used, however this measures the maximum area, not the actual average area.

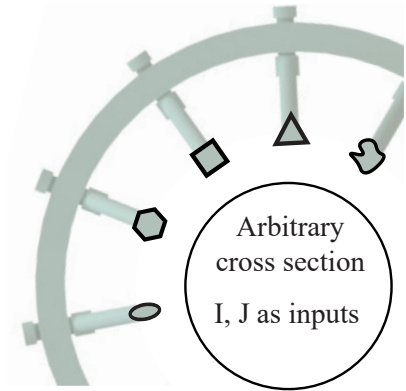


Figure C.1: Visualization of multiple possible cross sections for the longeron. For the data driven design model, J and I were included as variables, and so any possible crossection gets realised.

For this reason a systematic error of around 0.1 mm was found and corrected for.

Table C.1: Longeron diameters measured at 4 points for 1.5 mm diameter round cross section shape

Specimen	1	2	3	4	5	6	7	8	9	10	
	1.57	1.64	1.612	1.62	1.566	1.6	1.6	1.48	1.566	1.561	
	1.52	1.61	1.57	1.53	1.6	1.574	1.58	1.58	1.544	1.62	
	1.6	1.61	1.577	1.49	1.64	1.57	1.68	1.72	1.62	1.591	
	1.6	1.71	1.71	1.64	1.71	1.62	1.65	1.65	1.66	1.75	average
	1.5725	1.6425	1.61725	1.57	1.629	1.591	1.6275	1.6075	1.5975	1.6305	1.608525

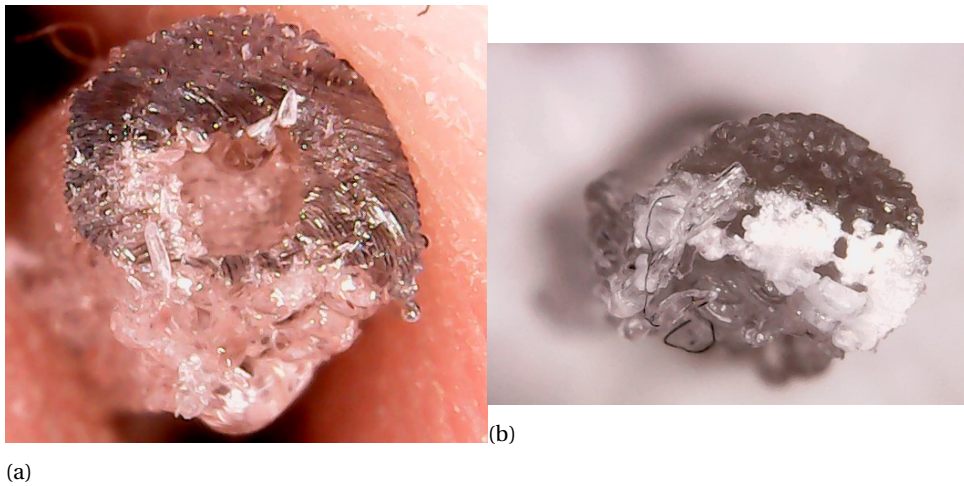


Figure C.2: Failed longerons: (a) Image of a longeron, printed without 100% infill setting, clearly illustrating weakness at build plate side, (b) Microscopic image 2mm diameter longeron which failed due to a poor print (bottom-left hand side attached to build plate), printed with 100% infill and 0.1 mm layer height.

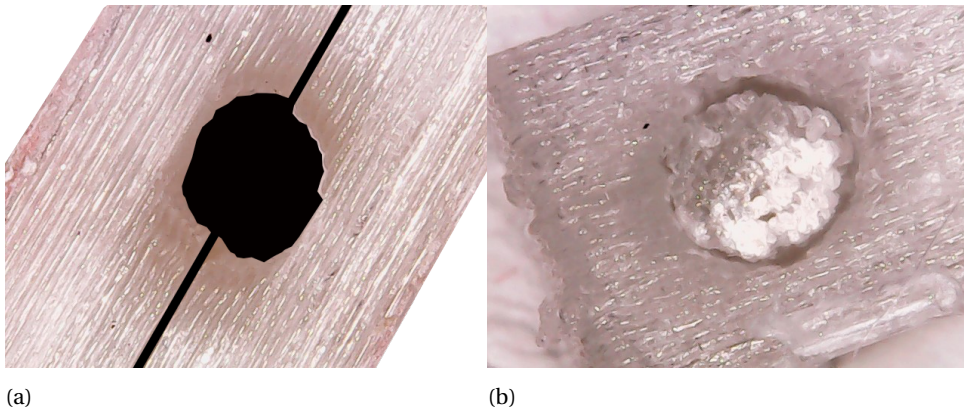


Figure C.3: (a) Microscopic image of hinge made of two rings. Background blacked out to show the misalignment problem. (b) Pin and ring printed simultaneously, clearly seen that longeron is not perfectly round.

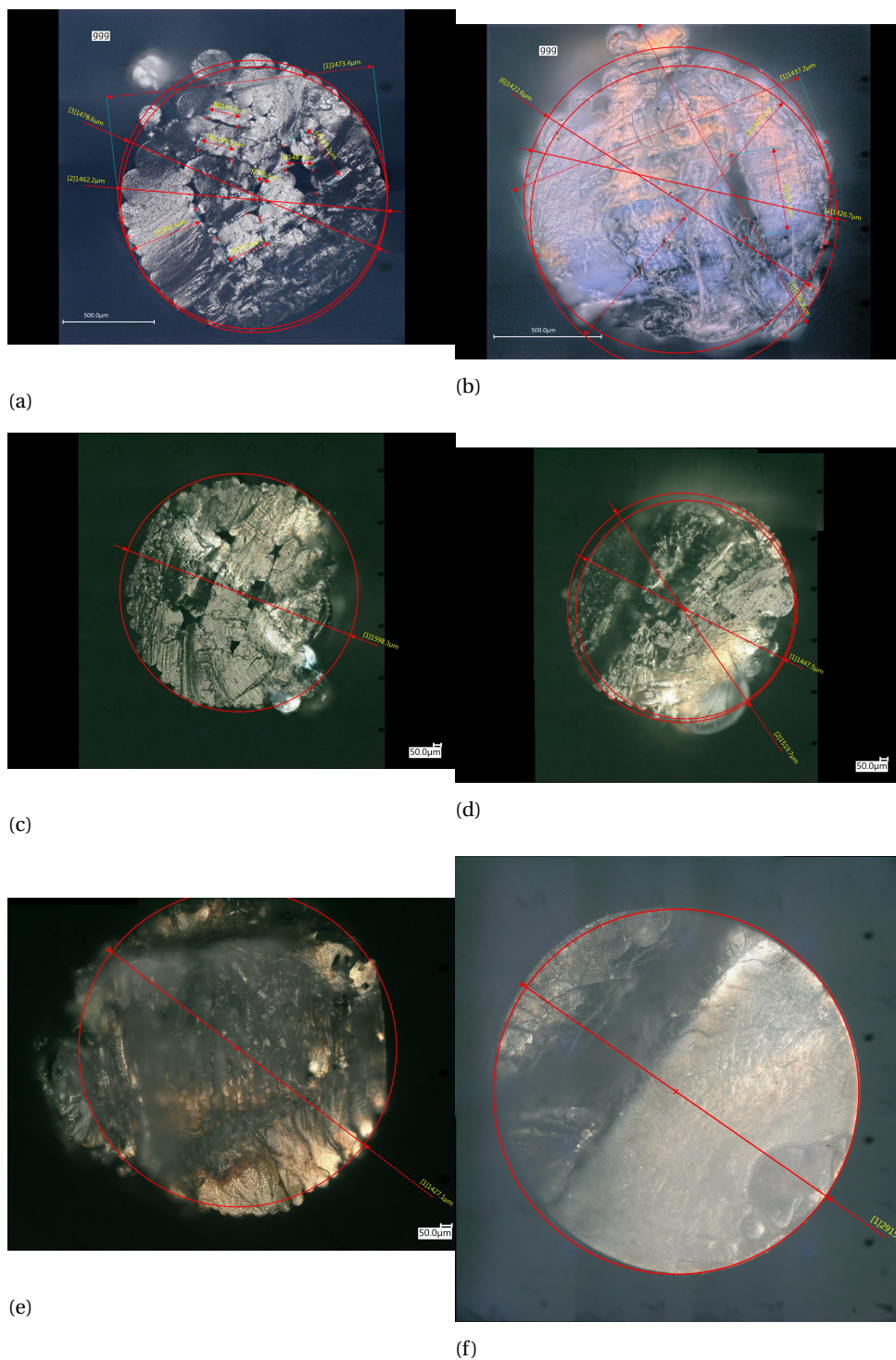
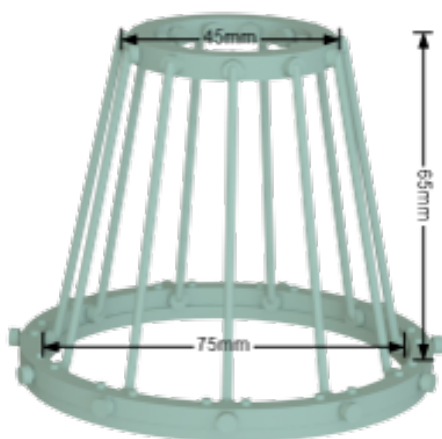


Figure C.4: (a-e) cross section 1.5 mm longerons (f) un-printed PLA filament 3 mm.

D

NOVEL DESIGN TO PRINT MAST ON ULTIMAKER 2

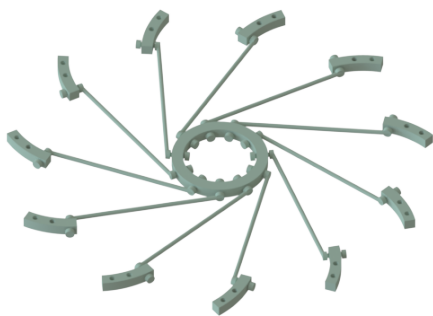
This first prototype (Point 1 in Figure 5.3), although functional, required an excessive amount of manual labour because it consisted of 15 separately printed components. Therefore, a new print scheme was devised to circumvent this issue. Instead of printing everything separately, an attempt was made to have only two separate prints for the complete assembly of the metamaterial: one part resembles a "spiderweb" and consists of the upper ring with the longerons, and a second print with a support ring. The idea is that the segments on the ends of the longerons snap into place on the support ring. Figure D.1 shows the outcome of this printing strategy.



(a) Computer-aided design model of metamaterial unit cell

(b) Image half-mast showing plastic deformation after buckling

Figure D.1: Metamaterial unit-cell printed using only two separate components.



(a)

(b)

Figure D.2: 3D printing optimised design for double-stack mast created with this middle section and two supporting rings.

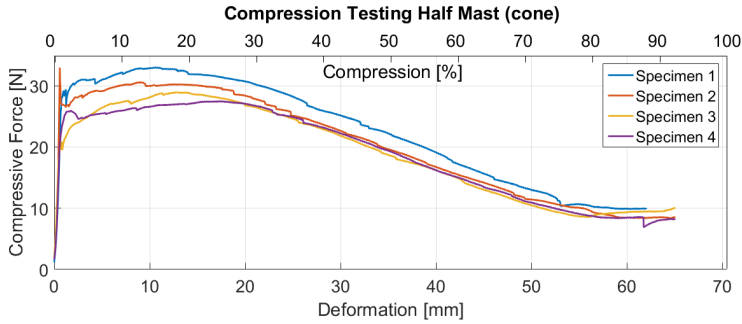


Figure D.3: Force displacement response compression testing prototype half-mast, using FDM printed PLA cone for free rotating end.

The "spider web" printing strategy worked as intended, but due to a policy of the faculty workshop of not allowing students to alter the printer settings, the print time was significantly longer than printing all components separately and, more importantly, multiple prints had significant defects (only approximately one third of the prints were without fault). Another possible solution to this problem was to use a newer 3D printer, Ultimaker 3, including a dual extrusion head in which one of them can build support material that is soluble in water. One attempt was made, printing PLA with PVA supports at the faculty of architecture and this too was unsuccessful due to a print defect (one longeron was not printed).

E

SUPPLEMENTARY INFORMATION MATERIAL TESTING

E.1. DENSIFICATION STRAIN

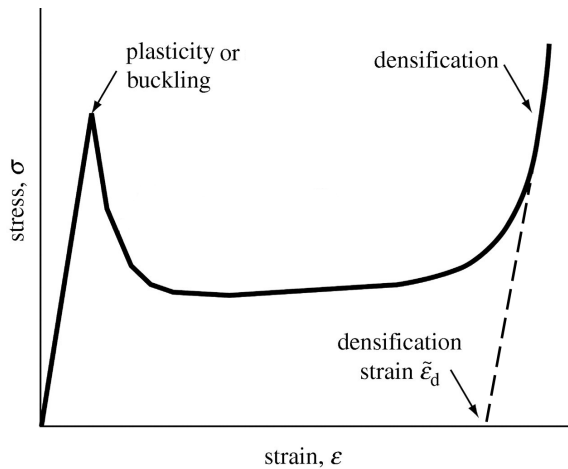


Figure E.1: Figure showing what densification strain of a material represents

E.2. ASTM D638-14

Equivalent specimen – ISO 527 - 12

A comparison between the ± 45 degree infill and unidirectional is seen in Figure 4.5. For the Young's modulus (E) the focus is only on the behaviour of the linear section at the start. One thing that should be noted is these two tests were conducted at differ-

ent times which can lead to marginally different properties due to the use of different printers.

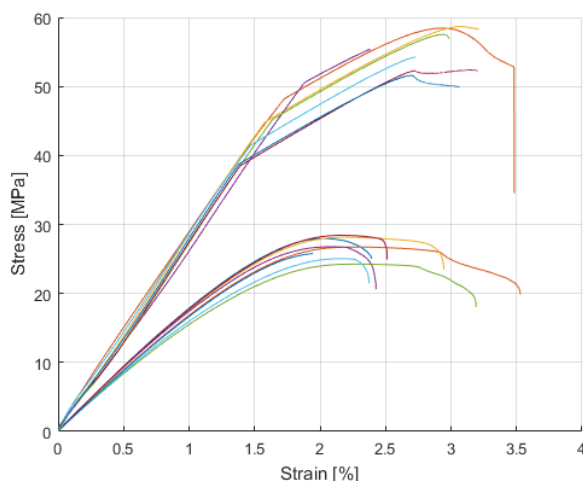


Figure E.2: Comparison Unidirectional vs. ± 45 degree infill on stress strain curve

During the test the extensometer needed to be removed before fracture. The strain value then switched to that of the crosshead sensor. As the cross head sensor of the testing machine is poorly calibrated resulting curve shows a distinctive elbow. This error is further validated by the force displacement curve where identical gradients can be seen after removal of the strain gauge as seen in Figure E.3b.

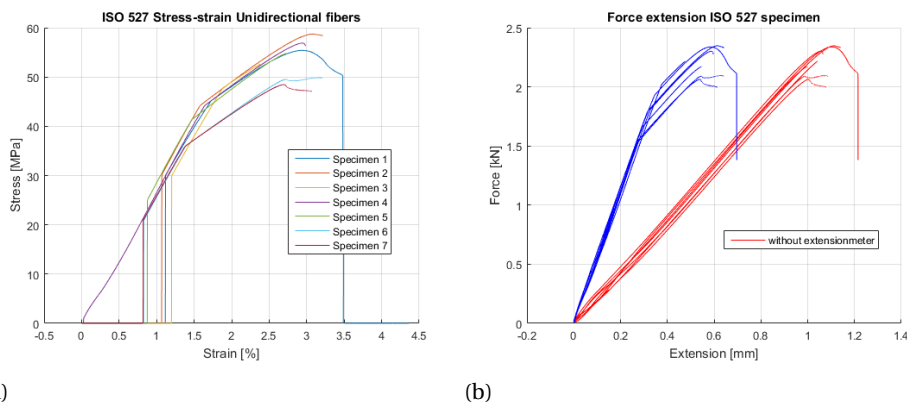


Figure E.3: (a) Theoretical Yield stress ASTM D638 specimen without removing strain gauge. (b) Comparison with and without strain gauge showing poor calibration displacement sensor

In most isotropic materials the Young's modulus is not size dependent and should be easily scalable over different sized samples. For this highly isotropic material however, it cannot be concluded that the changing porosity at various sizes doesn't affect the modulus. For this reason tensile samples were constructed with similar dimensions to the longerons used in the structure. A 1.5mm square sample was also attempted but do to a stress concentration caused by an air gap in the tapered region of the dog-bone sample, this data was not usable. As the samples were significantly smaller then the ISO 527 ones, the Zwick 10 tensile tester could not be used. Instead a Instron was used with 1000 N load cell.

E.3. DOG-BONE SPECIMENS

This section shows the raw test data for the dog-bone tensile specimens. Figure E.4 shows the stress-strain curve for 1.5 mm round cross section specimens, Figure E.5a shows the force displacement data for the 2 mm round specimen, and Figure E.5a shows the force displacement data for the 2 mm square tensile specimen.

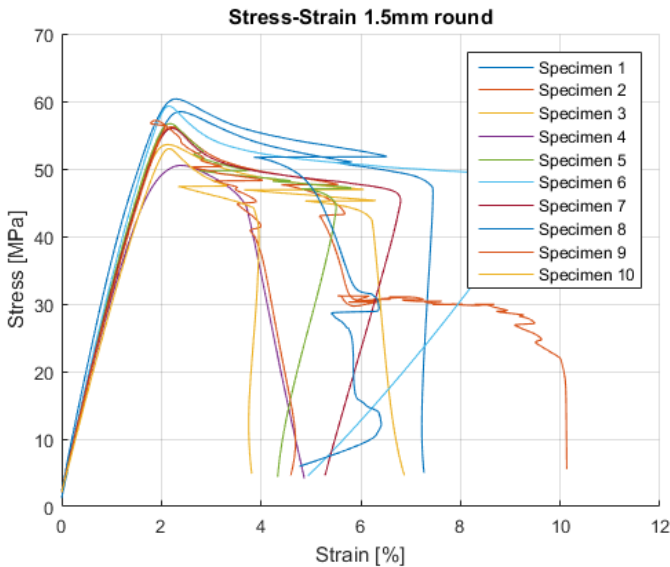


Figure E.4: Tensile test of a Dogbone shape with a circular crosssection of 1.5 mm diameter - Instron 1000 Newton load cell

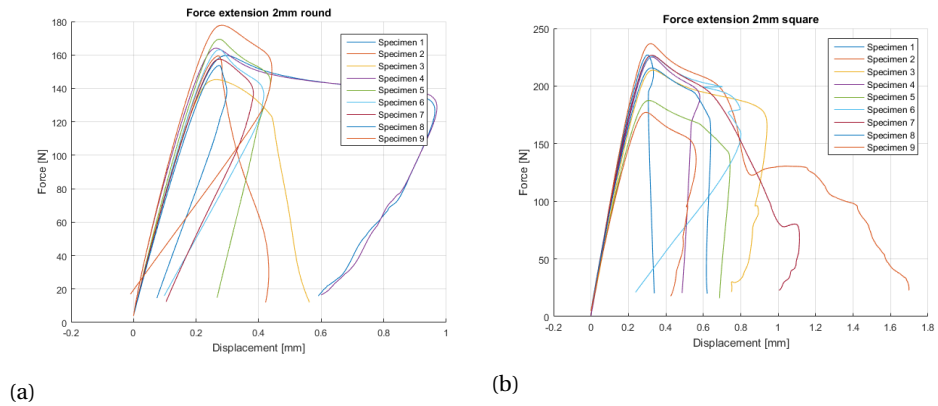


Figure E.5: (a) Tensile test of a dog-bone shape with a circular cross section of 2 mm diameter - Instron 1000 Newton load cell, (b) Tensile test of a dog-bone shape with a square cross section of 2 mm diameter - Instron 1000 Newton load cell

E.4. ASTM 695-15 COMPRESSION SPECIMEN

Figure E.6 provides the structure of the FDM printed specimen. The top and bottom roads contain small amounts of porosity, and under compression, this air is first compressed before the pure PLA is compressed. This results in the non-linear response at the start of the stress strain response seen in Figure E.7.

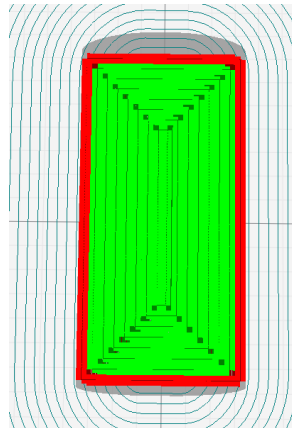


Figure E.6: Cura generated cross-section of the roads within a ASTM 695-15 compressive specimen.

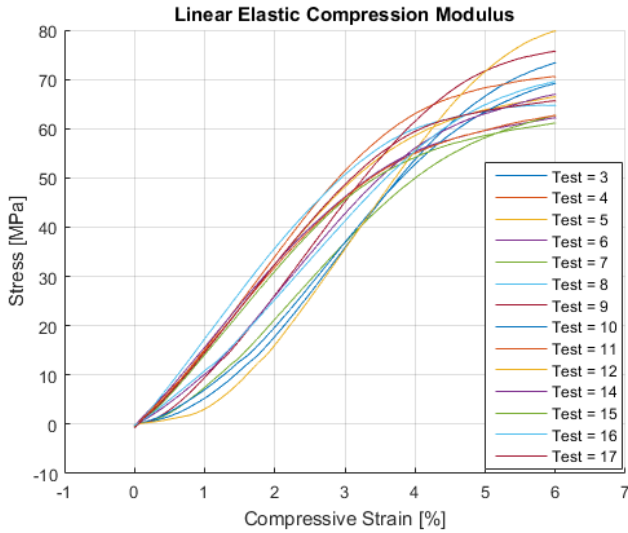


Figure E.7: ASTM 695-15 Compression sample testing on Zwick z10

E.5. TORSION TESTING

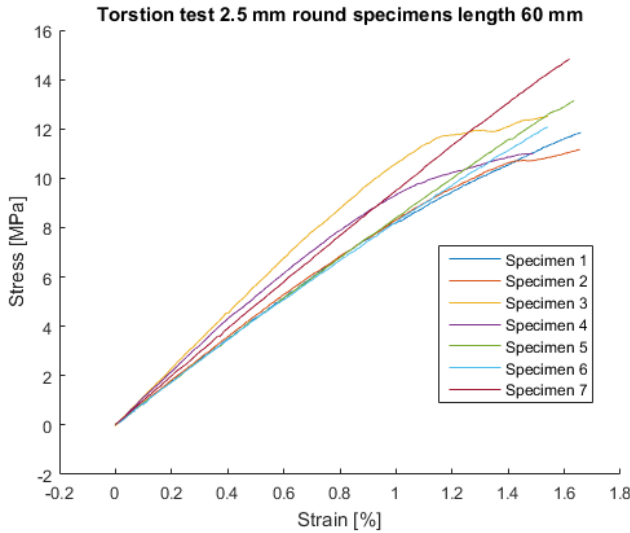


Figure E.8: A comparison of the initial loading cycles of each specimen which showed the highest amount of plasticity. This test setup used a 60 mm length between grips, resulting in the specimen being more sensitive to error. These specimens yield around 1 percent strain which is far earlier than expected.

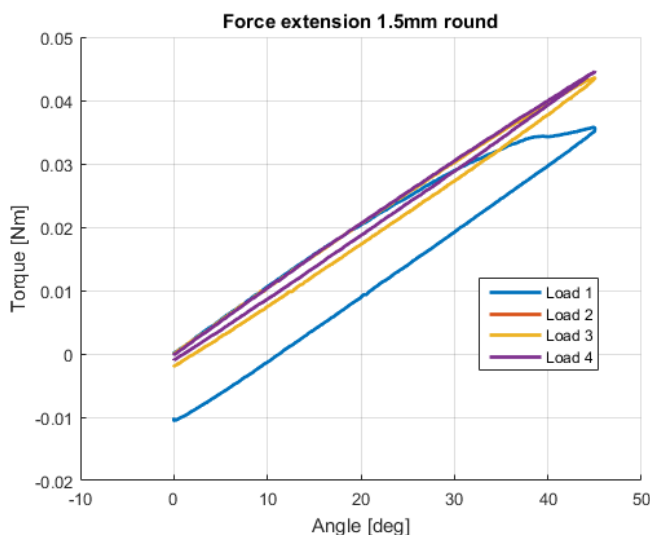


Figure E.9: Difference between initial load cycle with high plasticity and subsequent loading cycles. Initial cycle yields introducing strain hardening, subsequent cycles still representative for shear modulus.

E.5.1. TORSION SPECIMEN CROSS SECTION

Here a selection of microscopic images made of a the 2.5 mm round 3D-printed PLA specimen used in pure torsion testing are seen. These specimens originate from the same printer and were printed at the same time in the same conditions. There is a great degree of variance in both porosity and shape. This further supports that the largest concern with FDM is the consistency of print quality.

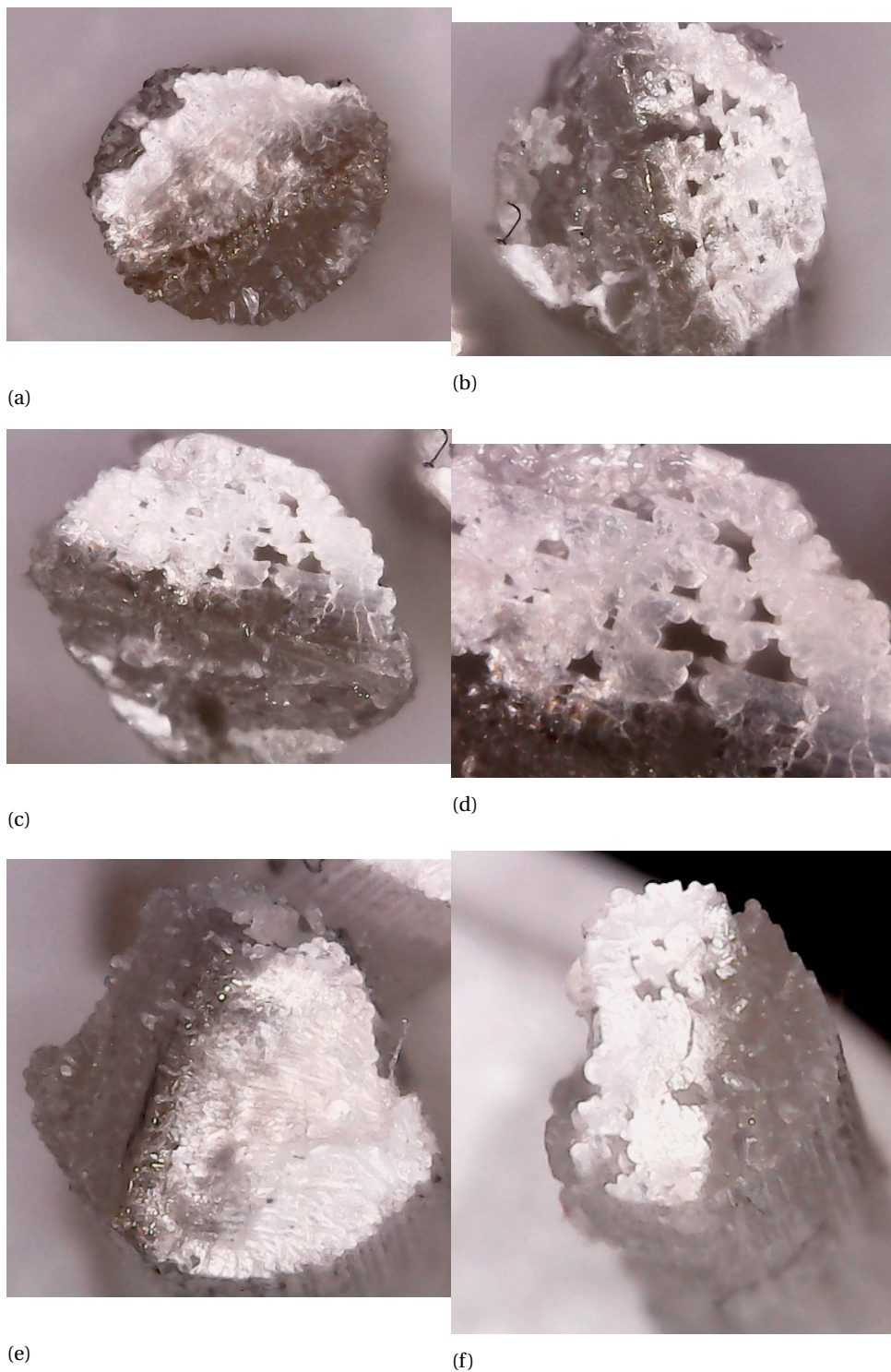


Figure E.10: (a-f) a selection of cross section microscopic images for 2.5 mm torsion specimens where (a) corresponds to Specimen 1 and (b) to specimen 3, remaining show clear shape and porosity defects

E.5.2. TORSION TESTING APPARATUS



Figure E.11: This figure shows specimen deformation and slip of attachment point of the mounting apparatus of the Zwick prototype machine, used for torsion, tension, and compression.

E.6. YIELD SURFACE PLOT

Figure E.12 shows an enormous amount of variation on the resultant data. This variation has several causes which will be addressed below

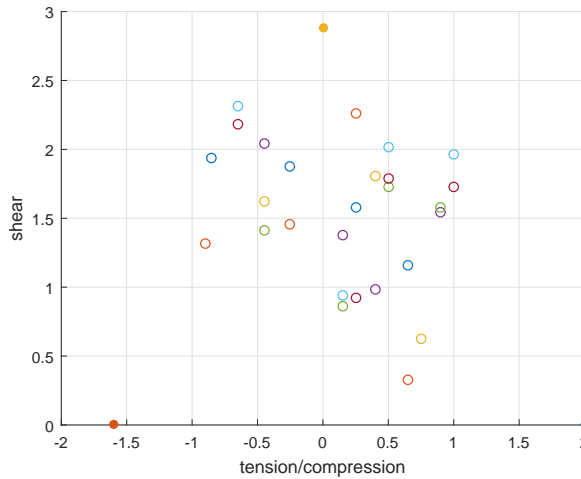
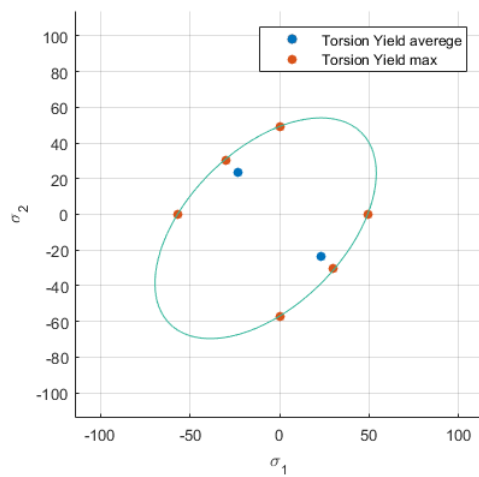


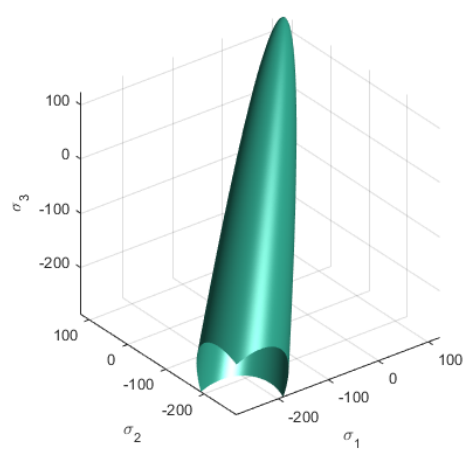
Figure E.12: Raw data multi-axial testing of 2.5 mm round specimen. Yield strain surface space.

1. The polymer is significantly softer than the steel clamps. Furthermore, there is no dog-bone shape of the specimens as the impact of the dog-bone on the results could not be calculated. This results in that the polymer experienced plastic deformation by the bolt before the test was begun, and as the bolts are hand tightened and the longerons not consistent in surface quality, this introduces significant variation.
2. For the compression tests, as there is also a rotational test which proceeds or follows the compressive load, there is a high probability of the clamps falling out of alignment. This is caused because the torsional clamp has a small freedom in the x-y plane, allowing for auto aligning in pure torsion testing. When adding a compressive element however, this caused the specimen to bend out of plane and affect the results.
3. The longeron specimens are printed with 2.5 mm diameter, with a layer height of 0.06 mm and with 100 % infill. The 3D printers are run by an external department within the university, and thus we were unable to control the printers ourselves. For the test specimens, the quality of the prints was worse than usual, and there was insufficient time to reprint the specimens before the test deadline.

This Zwick prototype is not designed to conduct a bi-axial tests, and this experiment would always be a challenge. For this reason I chose to try and approximate the yield surface through only uni-axially obtained data.



(a)



(b)

Figure E.13: Yield surface as calculated by analytical model presented by [7, 112, 113]

F

7 PARAMETER MODEL

This section briefly illustrates what the design space looks like when using the 7 parameter model constructed by Glowacki [89]. First Figure F1 shows a sensitivity analysis for all 7 parameters. The details of which are in [89]. Figures F2 and F3 show design charts as continuous plots for the influence of I_x on compressive strength. Interesting to note is that the mast diameter, which is of critical importance in the 4 parameter model, shows almost no influence over the compressive strength. This is because diameter is seeded in I_x which is of the order $[\text{mm}^4]$.

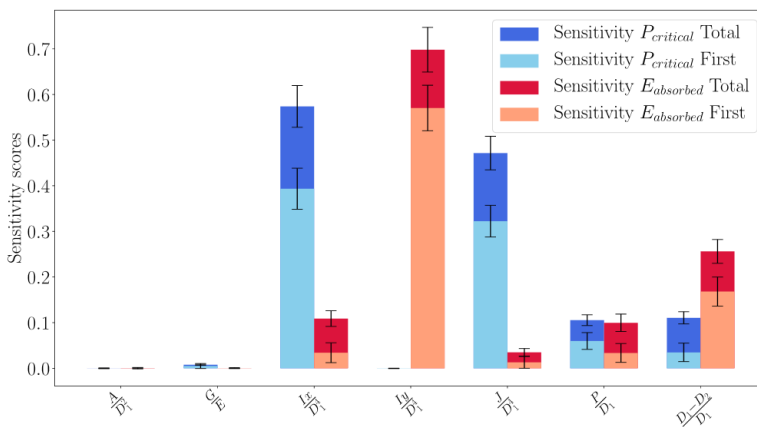


Figure F1: Sensitivity analysis of parameters

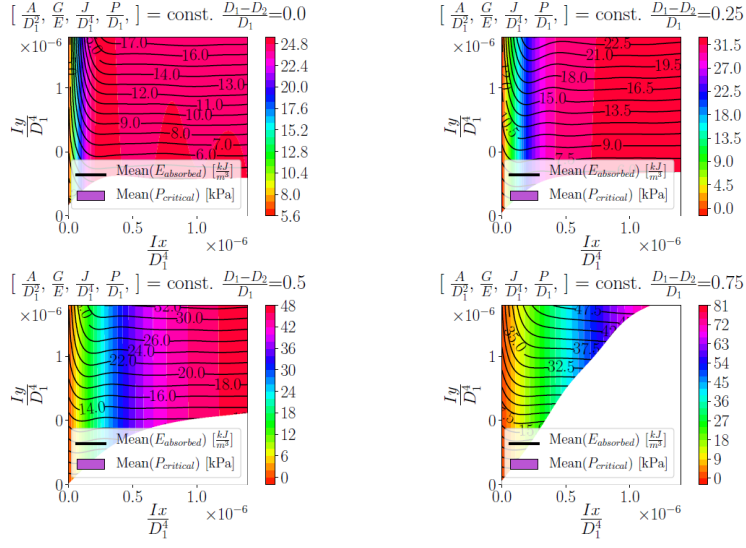


Figure E2: Mean quantities of interest as function of I_x , I_y , and D_R . The $A = 0.001$, $G/E = 0.36$, $J_\tau = 2.5 \times 10^{-6}$ and $P = 0.66$ remain constant

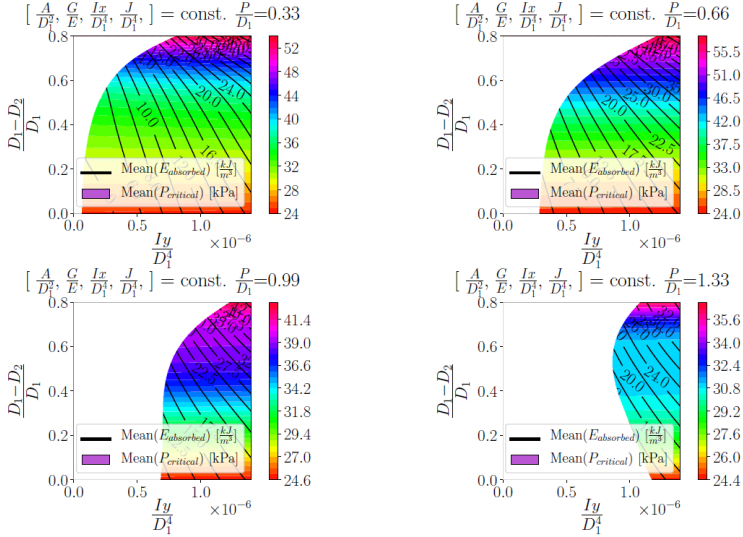


Figure E3: Mean quantities of interest as function of J_τ , I_y , and D_R . The $A = 0.001$, $G/E = 0.36$, $I_x = 7.5 \times 10^{-7}$ and $P = 0.66$ remain constant